The Magnetic Field, Temperature and Strain Dependence of Jc in Narrow Superconducting Tracks of (RE)BCO Coated Conductor

EMMA GRACE ELIZABETH GILLARD

The Magnetic Field, Temperature and Strain Dependence of J_c in Narrow Superconducting Tracks of (RE)BCO Coated Conductor

University of Durham

Emma Gillard

2025

Abstract

The dependence of the critical current density (J_c) on an applied magnetic field (B), temperature (T), angle of the field to the tape normal (θ) and strain (ε) for narrow tracks of Rare Earth Barium Copper Oxide (REBCO) coated conductor (CC) with a width down to 5 µm is presented. Our motivation is to investigate the properties of REBCO CC tracks and the viability of this superconductor for future Tokamak magnet systems.

We found the dependence of J_c on an applied strain for 100 µm chemically etched tracks to be inverse parabolic, similar to that of full-width 4 mm tapes. However the $J_c(\varepsilon)$ dependence for 5 µm focused ion beam milled (FIB) tracks was found to be much more sensitive to strain, with a shift in the peak of the $J_c(\varepsilon)$ curve to tensile strains from 0 % to above 0.3 %. After fitting the data to the bimodal chain model, and imaging the REBCO layer using electron backscatter diffraction (EBSD), we conclude that FIB milling changed the microstructure of the narrow REBCO tracks causing them to be richer in A-domains.

The J_c dependence on field, temperature and angle for the chemically etched and FIB tracks at 0 % strain was measured in detail and found to be the same as that for a full-width REBCO CC tape. Detailed measurements of $J_c(B, T, \theta)$ data were obtained down to 10 K and up to 0.7 T by developing a Cold Head cryocooler system for measuring the 5 µm FIB tracks.

A preliminary investigation into the $J_c(\varepsilon)$ dependencies for different orientations of current and applied strain in the REBCO tapes was also completed. We found that the J_c response to strain was weaker when the current and strain were orthogonal, and strongest when the current and strain were parallel. We also found that J_c was more sensitive to strain when the current and strain were parallel and along the tape length rather than across it.

Publications

Gillard E.G., Raine M.J. and Hampshire D.P. "The strain dependence of J_c of narrow-width tracks of REBCO coated conductor as a function of field and temperature," to be published.

Louzguiti A., et al. "On the evaluation of current sharing temperature within conductors of ITER toroidal field coils in operation," *IEEE Transactions on Applied Superconductivity*, 2025.

Gillard E.G., Raine M.J. and Hampshire D.P., "Resistivity measurements of the strain, temperature and angular dependence of the upper critical field of REBCO tapes up to 8 T," *IEEE Transactions on Applied Superconductivity*, vol. 33, pp. 1-5, 2023.

Declaration

I confirm that the work presented in this thesis does not contain material that has been submitted for any other degree other than this one in this or any other University. The work of this thesis is solely from my own research endeavors under the supervision of Damian Hampshire.

All sources used to aid this study have been correctly acknowledged and referenced in accordance with academic integrity conventions.

Acknowledgements

Accomplishing this PhD over the last four years has been a team effort, where I've been given the opportunity to work and spend time with a fantastic and uplifting group of people who have made the journey such a motivating but also fun and memorable one. My biggest thanks of course go to my supervisor Damian Hampshire, who has given me so much encouragement and guidance throughout the PhD and remained consistently positive in my work and my potential even when the experiments didn't go as planned (or things blew up!). For such support, and for all the opportunities I've been given, I am extremely grateful and I hope I can become as inspiring one day to an early career scientist in the future.

My next thanks must go to my office mates, namely Mark Raine, Rollo Hutson, Daniel Scobbie, Yahya Nasir, Charles Haddon, Rifa Alkhozondar, Freddie Daniels and all other members of the Superconductivity Group. Although perhaps productivity was compromised at times for extreme levels of fun and banter, I never imagined working in such a happy environment with such a kind group, and I thank them very much for making it so special. I hope also that the panda will be well looked after!

I must thank graciously all staff members who have spent a large amount of their time helping me with my work. I am especially grateful to Leon Bowen who has gone above and beyond in helping me with the microscopy work

that has formed the backbone of my PhD, it has been extremely fun working together and solving many complex problems. I thank also the team from the mechanics workshop who were always ready to help and built numerous parts for my experiments which have worked very well.

I would also like to give many thanks to the ITER group, namely Min Liao, Alexandre Louzguiti, Christine Hoa and Junjun Li who warmly welcomed me at ITER and gave me the most exciting experience, but also gave me a new level of confidence in my academic abilities that became a turning point in my career, and for that I am very grateful.

On a personal level, I would like to thank all the lovely friends I have made, and the important people I have met, throughout the duration of my PhD for their support and the fun times we've had. As well as hard work, PhD life at Durham University has been extremely fun and full of happy memories that I will cherish. My biggest thanks go to my extremely loving and supportive family, including Mum, Dad, Dan, Nanny, and to my Grandad who sadly passed last year, who have always been there providing unconditional love and support every step of the way; all of my achievements are thanks to their support and I hope I can make them proud.

Contents

Nomenclature

APC	Artificial Pinning Centre
CC	Coated Conductor
EBSD	Electron Backscatter Diffraction
FEA	Finite Element Analysis
FIB	Focused Ion Beam
HTS	High Temperature Superconductor
IBAD	Ion Beam Assisted Deposition
IPF	Inverse Polarity Figure
MCF	Magnetic Confinement Fusion
MOCVD	Metal-Organic Chemical Vapour Deposition
REBCO	Rare Earth Barium Copper Oxide
SEM	Scanning Electron Microscope
SG	Strain Gauge

Chapter 1

Introduction

In this doctoral thesis we present the research that was done to determine the critical current density (J_c) dependence on magnetic field, temperature and strain in narrow tracks of REBCO CC down to 5 µm in width.

The motivation of this work was to investigate the potential for the use of REBCO superconductor in the magnet system of future magnetic confinement fusion reactors. Nuclear fusion energy will likely be an important member of the future energy sources due to its large scale energy production, large fuel reserves and zero greenhouse gas emissions to combat global warming. The superconductor REBCO will likely be selected for use in future Tokamaks and Stellarators due to its higher critical surface, enabling the production of much stronger magnetic fields required for a good fusion plasma confinement, and overall more compact and cheaper fusion reactors.

To reliably construct cables and magnets for future Tokamaks and Stellarators out of REBCO CC, it is vital to ensure that the REBCO CC tape can perform well in the required operating conditions. The operating conditions of the REBCO magnets will likely be at low temperatures down to 20 K and exposed to high fields of up to 20 T which are the fields required for a com-

pact confinement of the fusion plasma. These high fields will also generate large Lorentz forces on the REBCO cables, generating large strains in the REBCO which must also be studied carefully, especially their effect on J_c.

To test the performance of REBCO CC in the operating conditions of the REBCO magnets, i.e. at 20 K and 20 T, the I_c of a full-width tape of REBCO CC is over 100 A, and is over 1000 A at 20 K in self-field, generating large amounts of ohmic heating and bulky experimental setups. We therefore aimed to lower the currents required to below one amp by preparing narrow tracks of REBCO CC, and compare their critical $J_c(B, T, \theta, \varepsilon)$ surface to that of a full-width tape, to determine whether the tapes can be characterised instead with narrow tracks of REBCO. This has several advantages, firstly it enables a characterisation of REBCO CC at much lower temperatures where I_c is usually too high, and also at much higher fields where the magnet bore size becomes very small and requires a miniaturised experimental setup to fit, for example at the > 60 T pulsed field magnets at Los Alamos where the sample space diameter is less than 10 mm. In summary, the use of small currents allows for cheaper and easier measurements at lower temperatures, higher fields, and under large strains, which also includes the use of a Cold Head cryocooler.

Therefore, to address the question of whether narrow tracks can be used to characterise full-width REBCO CC tapes, especially in Tokamak and Stellarator operating conditions, this doctoral thesis will be structured as follows. Firstly, in Chapter 2 an overview of nuclear fusion will be presented and its importance as a future energy source, where the role of HTS REBCO in enabling its success will be highlighted. This will be followed in Chapter 3 by a simplified presentation of the theory of superconductivity and the structure of HTS REBCO when manufactured as a coated conductor, including a description of the microstructure of the REBCO layer. The presentation of the experimental work will begin in Chapter 4 with an overview of some pre-

liminary work to measure $B_{c2}(T, \theta, \varepsilon)$ of full-width REBCO tapes. Following this in Chapter 5, an outline of the REBCO track preparation techniques will be presented, and the results of the $J_c(\varepsilon)$ dependence of these REBCO tracks in liquid nitrogen will be given in Chapter 6. Finally the results from a full set of $J_c(B, T, \theta)$ measurements on REBCO tracks using a Cold Head cryocooler will be presented in Chapter 7.

We will now begin this thesis with an overview of nuclear fusion presented in Chapter 2.

Chapter 2

Nuclear Fusion

2.1 Introduction

The main driver for the work outlined in this thesis is to study the behavior of HTS superconductors for applications specifically in nuclear fusion reactors. This chapter is devoted to providing a background in nuclear fusion energy, including how it works, where we are with it, and how feasible it will be to power the world in the future.

The chapter will begin with an overview of nuclear fusion, outlining the reasons for its development on earth and the benefits it has to offer. Following this will be a study of the physics behind nuclear fusion, including the plasma physics and the mechanism of the reactor. Finally, the chapter will end with a brief outline of the current status of nuclear fusion energy, and a discussion on its feasibility for future energy generation, with a final section on how HTS superconductors can help towards this.

2.2 Fusion Energy Overview

Nuclear fusion is the process of bringing together two light nuclei to overcome their mutual electrostatic repulsion and fuse together to form a larger nuclei. For light elements, this process releases more energy than is needed to overcome the electrostatic repulsion [1], making fusion a candidate for future commercial energy generation.

The call for nuclear fusion is driven by three main factors, a need to meet increasing energy demands, the need to replace non-renewable sources, and the need to combat global warming. Firstly, an increase in the world's energy consumption requires a large scale base-load energy source to meet this demand. The International Energy Agency predicts the worldwide energy usage to increase by 30 % by 2040 due to economic growth and enhanced living standards in developing countries [2]. Energy sources to meet the high energy demands already exist, however cannot power the world indefinitely because they are either non-renewable, or produce electricity that is reliant on external factors, for example, wind and solar depend heavily on the weather conditions [3].

This leads to the second need for nuclear fusion, which is finding an energy source to replace coal, oil and gas which is renewable, or has large fuel reserves. One study in [4] predicts the coal, oil and gas reserves to last around 107, 35 and 37 years respectively from when the study was published in 2009, based off of current energy consumption trends. The other reliable energy source is nuclear fission, whose fuel reserves can last until the end of this century with the current fission reactors used [5].

The final fundamental reason for nuclear fusion is the need for a clean energy source to combat global warming. Due to the emission of greenhouses gases from the burning of fossil fuels, global temperatures have risen by about 1.1 °C from 1850 to 2023 [6], leading to problems such as sea level rise and

changing weather patterns, which will have a significant impact on society.

Nuclear fusion would be able to solve these issues because of the following reasons [7]:

- No greenhouse gases emitted during fusion.
- Large fuel reserves.
- Large energy output per kilogram of fuel burnt.
- Negligible radioactive waste compared to fission.

The drawbacks of fusion mainly concern the difficulties involved in achieving it on earth, as the fusion plasma must be heated to tens of millions of degrees celsius and sustained for a long enough period of time for fusion to occur [8]. This makes the plasma very hard to contain and requires very robust materials and strong magnets to do so. Other drawbacks include the limitation of certain resources required for fusion, including lithium, as well as the irradiation experienced as a result of exposure to the plasma that slowly wears away at the reactor parts over time [9].

In the following section we will explain the physics behind a magnetic confinement fusion reactor.

2.3 Magnetic Confinement Fusion

This section focuses on the main physics and mechanism of magnetic confinement fusion (MCF) Tokamaks. Another popular MCF device is a Stellarator, which again uses magnets to confine the plasma but are shaped in intricate ways as to eliminate the need for a plasma current and hence to operate in steady state. We will however focus on the Tokamak here due to it having the oldest and more established technology. This section is split into two

parts, the first part focusing on the plasma and the second focusing on the general reactor design.

2.3.1 The Plasma

The fusion fuel chosen for almost all Tokamaks is the fusion of deuterium and tritium. Of all other light-element reactions, this reaction has the highest cross section σ (see Fig. 2.1), which refers to the probability of an interaction of the particles resulting in a fusion event [10]. The D-T reaction also has one of the highest energy outputs per reaction. The reaction is given by equation 2.1.

$$ {}_1D^2 + {}_1T^3 \rightarrow {}_2He^4 + {}_0n^1 \tag{2.1} $$

Each reaction releases 17.6 MeV of energy, 14.1 MeV of which is carried by the neutron and 3.5 MeV by the α particle. As the neutron is without charge, it escapes from the plasma and deposits its energy in the reactor walls, which will be used to generate electricity. The alpha particle however is charged and trapped within the plasma, its energy being used to heat the plasma causing further fusion [8].

A point called ignition is reached when the energy from the alpha particle is enough to overcome radiation losses from the plasma and cause fusion with no external heating required, in this case $Q_{plasma} = \infty$, where Q_{plasma} is the ratio of the power output from fusion in the plasma to the power put into the plasma to cause fusion [11]. The power balance at ignition gives rise to equation 2.2, where n is the number density of deuterium or tritium nuclei, τ is the confinement time of the plasma, $\langle \sigma v \rangle$ is the D-T cross section, T is the plasma temperature and E_α the alpha particle energy [8].

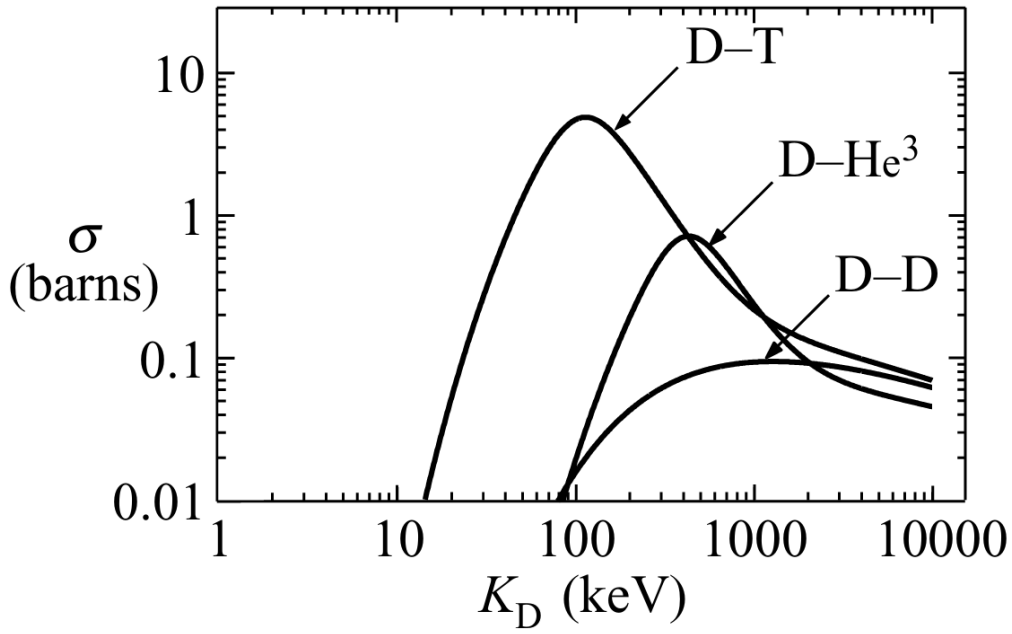

Figure 2.1: Cross sections σ for different fusion reactions as a function of deuterium kinetic energy K_D [10], where σ represents the likelihood of a particle interaction resulting in a fusion reaction.

$$n\tau > \frac{12}{\langle \sigma v \rangle} \frac{T}{E_\alpha} \tag{2.2}$$

For the case of D-T fusion, the quantity $\langle \sigma v \rangle$ is a function of temperature which has a minimum value at T =14 keV, and is approximated around this minimum by $\langle \sigma v \rangle = 1.1 \times 10^{-24} T^2$. Substituting this into equation 2.2 leads to the triple product equation for D-T fusion given by

$$nT\tau > 3 \times 10^{21} m^{-3} keVs \tag{2.3}$$

In reality, since tritium is a limited fuel reserve due to it being radioactive with a half life of 12.3 years, it must be created onsite within the Tokamak. This is generally to be achieved by reacting a neutron with a lithium-6 atom inside the breeder blanket according to equation 2.4 [11]. Therefore, the primary reactor fuels are deuterium and lithium.

$$_3Li^6 + {}_0n^1 \rightarrow {}_1T^3 + {}_2He^4 \tag{2.4}$$

Now the design of the reactor itself will be described, and the role of each component in housing the plasma and extracting the energy from fusion.

2.3.2 The Tokamak

The Tokamak is a device used to confine the hot plasma using very strong magnetic fields. Fig. 2.2 shows the ITER Tokamak. Each component of the Tokamak will be described below using the information given in the ITER website [12].

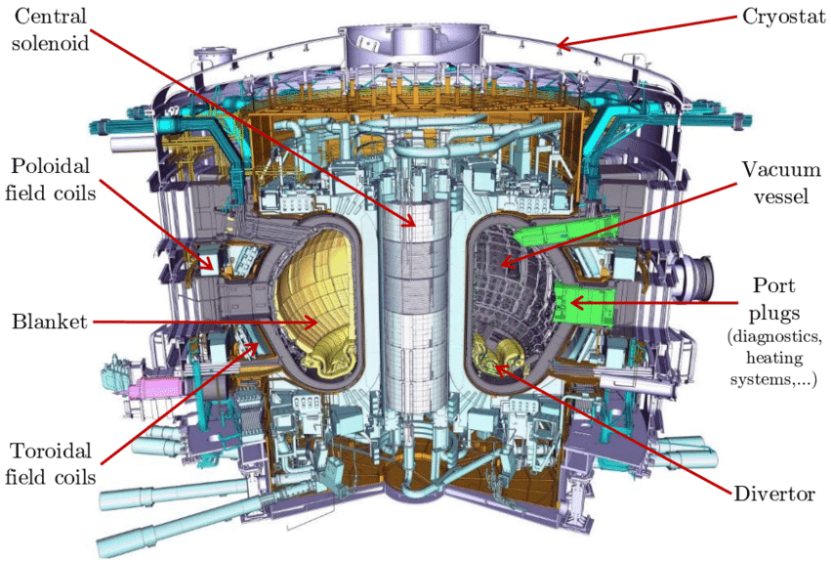

Figure 2.2: Components of the ITER Tokamak [13].

Vacuum Chamber

The plasma is injected into the vacuum chamber and heated via the induced plasma current along with neutral beam injection and high frequency electromagnetic waves [11]. The plasma will circulate within the vacuum chamber and nuclei will fuse generating energy.

Magnet System

The charged ions are tightly contained within the vacuum vessel with limited interaction with the vessel walls by using very strong magnetic fields. Charged particles within the magnetic field experience a Lorentz force, causing them to undergo a gyro motion around the field lines [14].

The toroidal field coils generate magnetic fields in the toroidal direction within the vacuum vessel, restricting the ions to a toroidal direction. However, the non-uniformity of the field leads to the ions drifting outwards towards the walls of the vessel. Therefore, an extra poloidal field is needed to

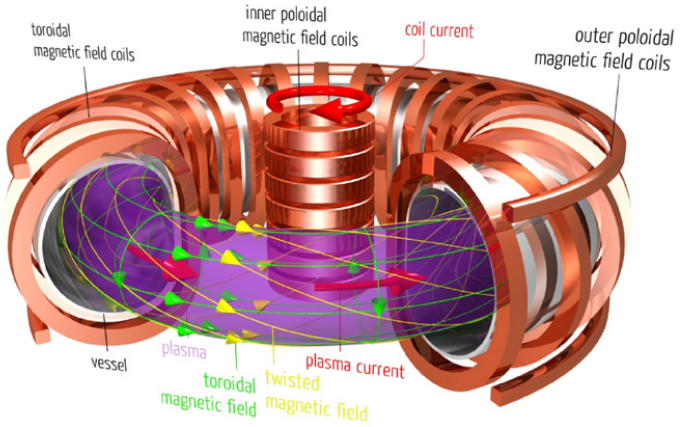

Figure 2.3: The magnetic field configuration inside of a Tokamak.

counteract this motion, creating a magnetic field distribution that is helical (see Fig 2.3) [10]. To create this field, the central solenoid starts up a plasma current by ramping down its magnetic field quickly. This generates a plasma current and the poloidal field required, as well as providing extra plasma heating [15].

The additional magnets such as the poloidal field coils are there to provide additional control and confinement of the plasma.

Blanket

The walls of the vacuum vessel are protected from heat flux and high energy neutrons by many blanket modules. These removable modules are installed side by side and entirely cover the vacuum vessel walls. The plasma-facing surfaces of each module (first wall) are likely to be made out of a low activation ferritic steel or tungsten due to their high melting temperatures, and each module will be filled with breeding material and a coolant, where pebbles of lithium ceramic compounds are an option for the breeder material and flowing helium gas or water as the coolant to keep the steel structure

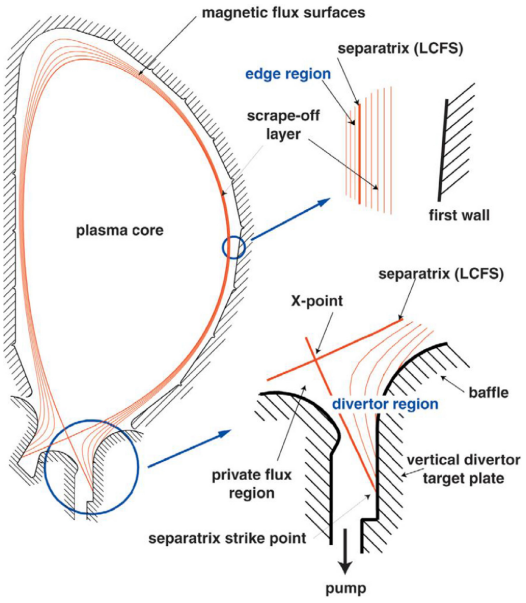

Figure 2.4: Illustration of the magnetic field lines guiding particles to the divertor region [18].

below 800 °C and extract heat from the reactor [16]. Some other designs also consider using liquid lithium-lead metal, or the molten salt containing lithium (known as Flibe), to act both as a breeder and a coolant [17]. The general concept is that the energetic neutrons from the fusion reactions are slowed by the blanket material and deposit their energy into the coolant flowing through the blanket, while also reacting with the lithium in the breeder material to reproduce tritium. The energy deposited into the coolant will be used to generate electricity in future reactors.

Divertor

Once many fusion reactions have occurred, a large amount of heat, unburnt fuel, excess alpha particles and impurities (ash) are created that must be removed from the vacuum vessel before they collide with the vessel walls and produce excess heating. The purpose of the divertor is to channel away this

excess heat, likely to be as much as 15 % of the total fusion power, and ions and ash using plates located at the bottom of the vessel. The ions and heat are channeled down to the bottom of the vacuum vessel along magnetic field lines created by special magnetic coils (see Fig. 2.4). The particles escape through a magnetic gap (separatrix) that surrounds the plasma and form a layer that is guided down to the divertor at the bottom of the chamber and out of the plasma [18]. The divertor plates must be able to withstand the highest heat loads of the reactor (around 15 $\mathrm{MW/m^2}$), as well as sputtering erosion caused by incident particles and any radiation effects. The divertor plasma-facing surface is therefore likely to be made out of tungsten which has the highest melting point of all metals of around 3400 °C, and will be cooled with a circulating water or helium gas coolant flowing through the structure to keep the temperature of the divertor below 1300 °C [19].

Cryostat

Due to the very high heat fluxes from the plasma, all components, especially the vacuum vessel, must be kept very cold to prevent damage from the heat loads. The superconducting magnets must also be cooled to very low temperatures. Therefore, the entire reactor is contained within a cryostat which is maintained under vacuum to minimise heat flux from the plasma, and from the surrounding environment.

Electricity Generation

To generate electricity, the energy from the neutrons will be deposited into the water coolant flowing through the blanket. This will convert water into steam and be used to drive a turbine to generate electricity, as in most other power plants. A diagram of the process in shown in Fig. 2.5.

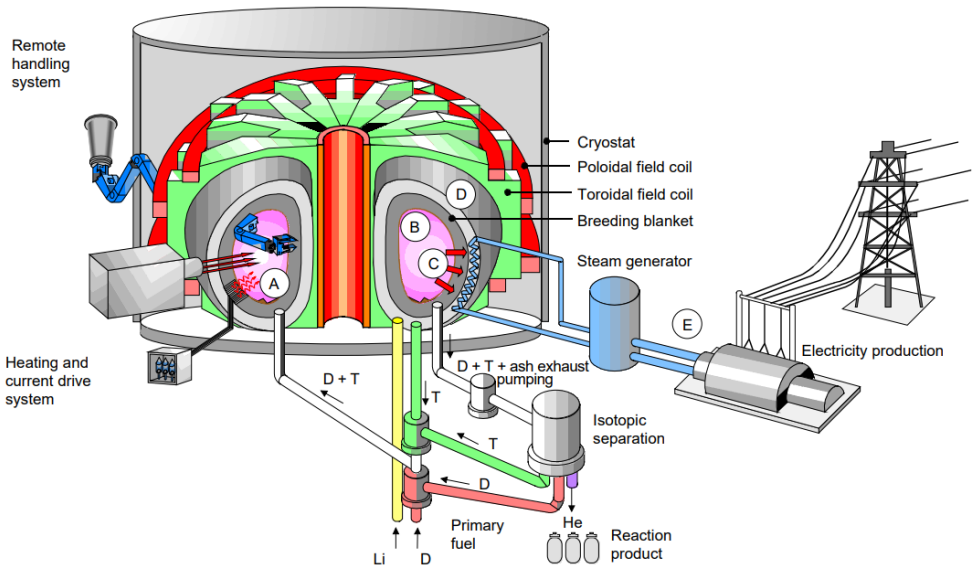

Figure 2.5: Illustration of a nuclear fusion power plant [11].

2.4 Current Fusion Timeline and Status

There are over 150 fusion facilities being built or being operated all over the world [20]. The ones operating however are only experimental reactors; a commercial reactor is yet to be built.

Here several of the important upcoming fusion projects will be outlined, namely ITER (France), STEP (UK), the SPARC and ARC reactors (USA) and EAST (China) which are Tokamak projects, and Proxima Fusion (Germany) and Renaissance Fusion (France) which are companies working on Stellarator projects. These projects aim to deliver breakthroughs in fusion performance that have so far not been achieved. The first main breakthrough is the generation of more energy from fusion of the fuel than is put into the fuel to cause fusion. This is quantified by the Q_{plasma} factor , given by equation 2.5 [10].

$$Q_{plasma} = \frac{net\ thermal\ power\ out\ from\ the\ plasma}{heating\ power\ into\ the\ plasma} \tag{2.5}$$

A Q_{plasma} factor greater than 1 indicates that more power is produced by fusion fuel than is put into the plasma to initiate fusion. It is important to distinguish Q_{plasma} from Q_{total}, where Q_{total} accounts not just for the energy put into the fuel, but for the total energy required to operate the reactor. The current Q_{plasma} factor record for a Tokamak is still held by JET (UK), where it produced fusion energy with $Q_{plasma} = 0.67$ in 1997 [21]. The Q_{plasma} values are expected to be 10 for ITER [22], 10 for STEP [23], 11 for SPARC [24] and 13.6 for ARC [25]. Despite the EAST reactor not aiming to demonstrate large Q_{plasma} factors, it has delivered remarkable plasma confinement times, reaching a current world record confinement time of nearly 17 minutes in 2025 [26]. Both Proxima Fusion and Renaissance Fusion aim to produce Stellarators with Q_{plasma} factors greater than one and with large power outputs, with the Stellaris reactor at Proxima Fusion being designed to produce around 2700 MW of power compared to 500 MW for SPARC and ARC [27].

After generation of net power output, the next breakthrough will be generating large quantities of energy at prices competitive with other energy sources. This goal can be reached by constructing smaller and cheaper reactors with a similar power output. STEP and SPARC aim to address this with their use of stronger HTS magnets allowing for a smaller reactor size [24] (e.g. SPARC will have a major radius of 1.85 m compared to 6.2 m for ITER [20]). Success of the SPARC reactor will lead on to the construction of ARC, one of the first of the generation of fusion reactors connected to electricity grids [28]. The economic and commercial benefits that accompany Stellarators are their ability to operate in steady-state rather than short pulses as in Tokamaks which hints towards Stellarators being more commercially admirable. The companies Proxima Fusion and Renaissance Fusion will also be

utilising HTS technology to minimise the size of their Stellarators, where the plasma volume of Stellaris will be only $425\,\mathrm{m}^2$ compared to $840\,\mathrm{m}^2$ at ITER [27]. Renaissance Fusion is working to develop an even more elegant, easier and cheaper path to fusion which involves patterning the current paths onto the HTS magnets using lasers after the magnets have been installed into the Stellarator [29].

The timeline for construction of each Tokamak is different. The ITER project started construction in 2010 and is planned to begin first plasma experiments in 2034 [30]. The planning for STEP was announced in 2019 and aims to be completed by 2040 [31]. SPARC, began construction in 2021 and aims to begin operation by 2026 [32]. After that, ARC will be built and is scheduled to operate in the early 2030s [33]. Both Stellarator companies aim to have built their first Stellarators in the 2030s, with the first model reactor named Alpha at Proxima Fusion to be built by 2031 [34]. The reason for the difference in timelines could be due in part to the reactor size and complexity, and in part to the project management and funding. ITER is the largest reactor and an international collaboration, where each member country contributes by building parts of the reactor [35]. STEP will similarly be a project replying on both public and private sectors [31]. SPARC, on the other hand is a much smaller reactor owned by the private company Commonwealth Fusion Systems and MIT's Plasma Science and Fusion Center [32]. Similarly Proxima Fusion and Renaissance Fusion are small private companies with ambitious timelines. It could be argued that the timeline for commercial fusion will be accelerated due to the increased involvement of the private sector [1].

2.5 The Reality of Nuclear Fusion

This section will evaluate the reality of nuclear fusion becoming a clean and reliable energy source for commercial consumption. This includes the difficulties involved in achieving a large energy gain from fusion and whether,

once working, it solves problems that other energy sources can't, such as fuel reserves, safety and cleanliness. In addition, if able to solve the problems above, will fusion energy arrive quickly enough to replace current energy sources and mitigate the effects of global warming, and at a price that is affordable by the general public.

2.5.1 Withstanding Heat and Particle Loads

The first problem is choosing materials that are able to withstand the extreme plasma conditions to build the reactor out of. As mentioned, the plasma must be heated to extreme temperatures and also generates high energy neutrons which cause irradiation damage. These extreme conditions put huge requirements on the reactor components which are beyond the capability of current materials [36].

2.5.2 Large Energy Gains

One of the fundamental benefits of fusion energy is its prospect to deliver a large-scale amount of energy due to the high energy density of fusion fuel. However, even with a reactor able to withstand the extreme conditions required, producing large amounts of energy from fusion is hard to achieve. This is because the plasma itself will naturally lose energy through radiation losses and conduction losses from small-scale turbulence instabilities present in a plasma. These losses are always present in a burning plasma, making a large net energy gain from fusion difficult to achieve [10]. In addition, we must take into account the large energy consumption of the coils, cryogenic systems, auxiliary systems etc as well as the power into the plasma, meaning a Q_{total} requirement of order 50 is more realistic [37].

2.5.3 Resources and Renewability

Another of the advantages to nuclear fusion over the other carbon-based energy sources is its vast supply of fuel reserves. One of the fuel components, deuterium, is very abundant in seawater and able to provide fuel for billions of years. The other primary fuel, lithium is a relatively abundant element found in various minerals and brines, and could provide fuel for the next 1000 years if used only for fusion [38]. It however competes with several other industries, for example the battery industry [39]. Therefore, although abundant, the fuel reserves for fusion are not unlimited.

2.5.4 Cleanliness and Safety

One further favorable quality of nuclear fusion is that the reaction releases no greenhouse gases. The reaction by-products are a neutron and an alpha particle both of which are confined within the reactor and do not harm the environment. This suggests that fusion energy would be a good solution to mitigate global warming. It is not however an entirely clean energy source due to some radioactive waste generated. The two types of radioactive products in a fusion reactor are the tritium fuel (around 1kg of tritium will be used at ITER), and activated materials from high energy neutron irradiation [40]. The radiotoxicity from these products is however several orders of magnitude lower than in fission reactors [40]. Additionally, there is no risk of a chain reaction from nuclear fusion, unlike fission, and hence there is no risk of a nuclear accident [14]. Hence nuclear fusion is deemed a safe, environmentally friendly fuel source.

2.5.5 Fusion Timeline and Cost of Electricity

Currently, nuclear fusion is still in the experimental phase, where reactors are being built to prove that the underlying physics and technology works. As more money is now being invested in nuclear fusion, and many more

companies are working on building reactors, the time until a commercial reactor has sped up. Some ambitious projects such as ARC aim to generate commercial electricity by nuclear fusion by 2035. For the mitigation of global warming effects it is required that nuclear fusion takes off within the next 50 years [41], therefore fusion could likely prevent further global warming. The other important consideration is the cost of electricity from fusion, where prices will need to be competitive with the other energy sources. For fusion to be competitive, the cost for electricity will need to be around $80-100 /MWh at 2020 price, however the expected price for the first power plant is expected to be greater than $150 /MWh [42]. Therefore, even with well-established reactors and technology, fusion energy could still cost 50-80 % more than a present-day fission reactor [43].

2.6 The Need for Superconductors in a Tokamak

The basics and reality of fusion energy has now been discussed, so focus will now be directed to one crucial aspect of nuclear fusion that determines its underlying success, that is the superconducting magnet system.

The magnet system is an integral part of Tokamaks as it is required to confine the plasma in which fusion occurs. Despite this, the magnet system is the most expensive part of the Tokamak, constituting around a third of its total cost [42]. Normal copper magnets are unfeasible to use as the electricity cost of running the magnets would be too high [24] with too much power loss from ohmic heating, so superconducting magnets are the only viable option.

Many Tokamaks have been constructed using the low temperature superconductors Nb_3Sn and NbTi, for example ITER [44]. But the advancement of HTS superconducting technology has since opened up a whole new scope of possibilities, especially the ability to reach much higher magnetic fields larger

than 20 T [45]. The use of higher fields enables a smaller reactor size for the same power output [46], according to the triple product, given in equation 2.6, where R is the Tokamak major radius and B is the magnetic field on the plasma. This presents an opportunity to construct smaller and more compact reactors [1], which would generally be cheaper to build and hopefully reduce the cost of electricity from fusion.

$$nT\tau_E \propto R^{1.3}B^3 \tag{2.6}$$

The HTS material Rare Earth Barium Copper Oxide (REBCO) is now commercially available in long lengths [47]; tapes as long as 1 km are being produced from the manufacturer SuperPower [48], and several fusion companies are starting to exploit this technology, namely SPARC and ARC in the USA, as well as STEP in the UK. These companies are planning to build some or all of their magnets out of the HTS material REBCO.

The contents of this work therefore focus on the high temperature superconductor REBCO, and it's performance in Tokamak-like conditions, including at low temperatures down to 10 K, high fields, and various strains.

2.7 Conclusion

There are many reasons that drive the need for a new, abundant and clean energy source, from an increase in the world energy demand to a need to combat global warming, and nuclear fusion seems to offer solutions here. The solutions include the large fusion fuel reserves, the high energy density of fusion and its emission of zero greenhouse gases. Despite its advantages, nuclear fusion energy poses some difficulties, including several technological and physics constraints, whether there actually are large fuel reserves, as well as whether fusion can start generating electricity within an acceptable time-

line and at an acceptable price. Despite these difficulties, much progress has been made in the last 100 years, including the development of HTS magnets enabling smaller and cheaper reactors, as is being exploited in the SPARC reactor. Therefore due to all the advantages associated with nuclear fusion energy, it is important to continue efforts towards its commercialisation.

Chapter 3

Rare Earth Barium Copper Oxide (REBCO) Superconductor

3.1 Introduction

After providing an outline of MCF in the previous chapter, we now focus on and present an overview of the superconductors that form an integral part of MCF reactors.

The chapter begins by presenting a basic overview of the theory of superconductivity, followed by a closer look specifically at the mechanism of superconductivity in HTS REBCO. Following this we look at the manufacturing process of the REBCO CC that are used to build strong electromagnets, and how the manufacturing route creates a specific microstructure within the REBCO layer. We finally investigate the components within the REBCO microstructure that lead to specific dependencies of J_c on an applied field, the angle between the tape normal and the field, and an applied strain.

3.2 Superconductivity

3.2.1 Type I and Type II Superconductivity

The phenomenon of superconductivity was first discovered in 1911 by H. K. Onnes, who found materials that exhibited zero resistance once cooled below a certain critical temperature T_c [49]. This was followed by the second important discovery of superconductivity known as the Meissner effect in 1933 [50].

Type I Superconductors and the Meissner Effect

The Meissner effect, which is characteristic of a Type I superconductor, is the expulsion of all the magnetic field from within a superconductor once it is cooled below its T_c. This however does not occur for all magnetic fields applied across the superconductor, and when the applied field is above a certain critical field $H_c(T)$ value, the Meissner effect can be overcome and the field will fully enter the material again, leading to a loss of superconductivity. Type I materials are denoted as perfect diamagnets below T_c, since their magnetization must be equal but in the opposite direction to the applied field to eliminate magnetic field from within the material, i.e. $\mathbf{M} = -\mathbf{H}$ (see Fig. 3.1).

Type II Superconductors

Despite the successful discovery of Type I superconductors, they had few practical applications due to their inability to carry much current due to their low values of H_c. This minimum current that causes superconductivity to be lost is called the critical current I_c. In Type II superconductors the situation is more complicated. Type II superconductors behave like Type I and exhibit the Meissner effect up to a certain field H_{c1}. Beyond H_{c1}, instead of allowing the full field to penetrate they allow partial penetration

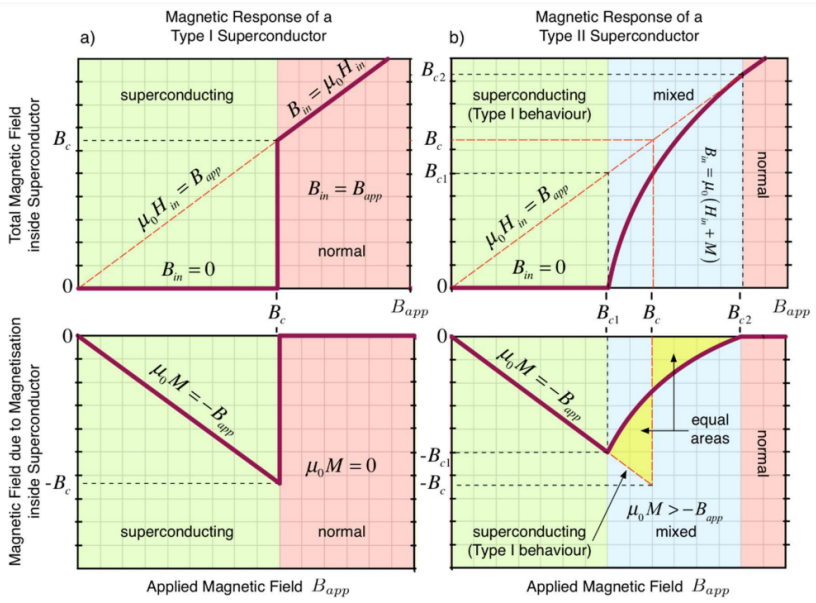

Figure 3.1: The magnetic response of a) Type I and b) Type II superconductors [51].

of it in the form of magnetic vortices known as fluxons (see Fig. 3.2). As the applied field increases, the amount of field penetration increases until the upper critical field H_{c2} is reached, then the applied field fully penetrates the material and superconductivity is lost. This much higher value of H_{c2} means that a Type II superconductor can carry much more current.

Penetration Depth and Coherence Length

Whether a material will behave as a Type I or Type II superconductor depends on two parameters, the penetration depth λ and the coherence length ξ [52]. A magnetic field applied across a superconductor can penetrate a small distance into the material; the field falls off exponentially over a mean distance of λ. The size of λ is about 0.25 µm, so essentially $B = 0$ T inside a bulk superconductor. The other parameter ξ refers to the interaction length between a pair of electrons that are responsible for superconductivity, or

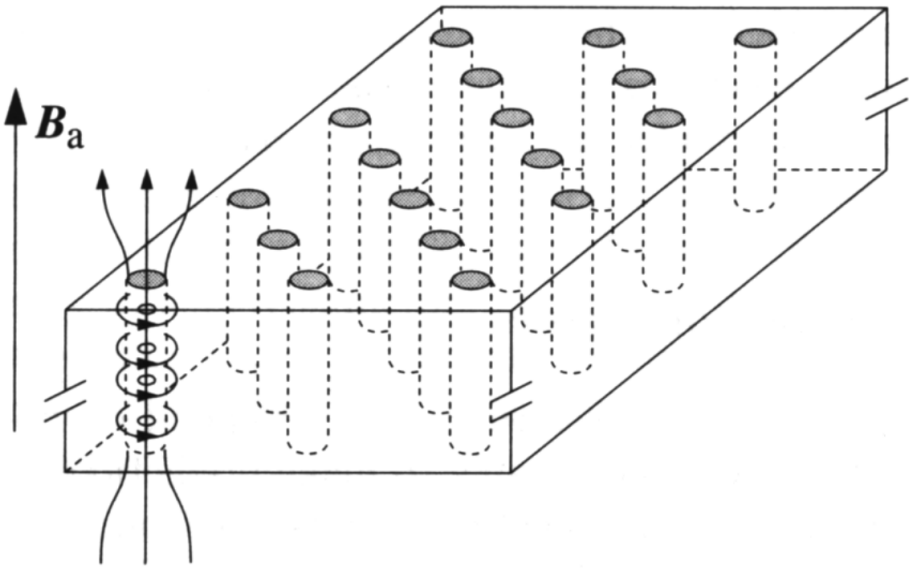

Figure 3.2: Penetration of the applied field as fluxons within a Type II superconductor.

the likelihood of them interacting. For Type I superconductors, ξ is around 0.3 µm and for Type II superconductors it is a few nanometers.

The ratio of these parameters $\kappa = \lambda/\xi$, known as the Ginsburg-Landau ratio, characterises whether a material is Type I or Type II. Type I occurs when $\kappa \leq 1/\sqrt{2}$; superconductivity can occur in this case because applied fields below H_c cannot penetrate far enough into the material to affect the electrons within a coherence length, and Type II when $\kappa > 1/\sqrt{2}$; in this case superconductivity occurs because the electrons are bound by such a small coherence length that the field up until H_{c2} does not affect them.

Fluxons

For a Type II superconductor, the field enters the material one fluxon at a time, where a fluxon is the quanta of magnetic field given by $\Phi_0 = h/2e = 2.0678 \times 10^{-15}$ Webers, and has a radius size on the order of a coherence

length. The fluxon forms a cylindrical region of normal material that traps the field, and is circulated by a superconducting current that shields the field. The fluxons repel each other and arrange themselves into a hexagonal pattern known as an Abrikosov lattice, allowing current to flow between them.

As the value of H_{c2} is much larger than H_{c1}, 10 T as opposed to 0.01 T, Type II superconductors are able to carry a much higher current even in large fields. The current however produces a Lorentz force on the fluxons given by $\mathbf{F} = \mathbf{J} \times \mathbf{B}$ which can cause the fluxons to move and dissipate energy in the lattice, this is equivalent to a resistance. Therefore, I_c can be enhanced by "pinning" the fluxons in place using grain boundaries or other special pinning sites.

3.2.2 Microscopic Theory of Superconductivity

A theory to explain the phenomenon of superconductivity was proposed in 1957 by Bardeen, Cooper and Schrieffer and is known as BCS theory. It is a microscopic theory because it explains superconductivity in terms of the interaction between electrons and the lattice that surrounds them.

The theory is based on the assumption that superconductivity arises due to a weak electron-electron interaction that is mediated by a lattice phonon, and this attraction overrides the electron coulomb repulsion leading to a sea of electron pairs, known as Cooper pairs. These Cooper pairs are bound pairs of electrons that occupy states with equal and opposite momentum and spin, and are separated by a distance equal to the coherence length. The Cooper pairs are the superconducting charge carriers.

The Cooper pairs occur because the stability of the superconducting state is higher than the normal ground state Fermi sea of electrons all with $k < k_F$. This can be explained as follows: if there is a weak attractive interaction between electrons, some electrons will be scattered and therefore have a final

momenta k which is above the Fermi surface, although this raises the overall kinetic energy of the system, the electron-electron interaction actually lowers the bound state energy with respect to the Fermi surface by an amount given by equation 3.1 [53].

$$E \approx -\frac{2\hbar\omega_D}{exp[2/V_0 D(E_F)] - 1} \tag{3.1}$$

Here $\hbar\omega_D$ is the phonon energy, V_0 (units eV) is the interaction energy, and $D(E_F)$ (units $/eV$) is the density of states at the Fermi surface.

This lowered potential energy more than compensates for the increase in kinetic energy caused by having electrons occupy states with $k > k_F$, regardless of how weak the attraction is. It is therefore energetically favorable for electrons to exist as bound Cooper pairs.

3.2.3 Ginzburg Landau Theory for Superconductivity

Despite the success of BCS theory, it has limitations as it predicts superconductivity not to occur above 30 K, whereas many superconductors have $T_c > 30$ K. One other phenomenological theory that does not explain the mechanism for superconductivity but rather accurately predicts the behavior of supercondutcors in magnetic fields was proposed in 1950 by Ginzburg and Landau. The Ginzburg-Landau (GL) theory focuses solely on the superconducting electrons, describing them by a complex order parameter ψ such that $|\psi|^2$ is proportional to the density of superelectron pairs n_s.

According to GL theory, current in the superconducting state is carried by superelectrons of mass m^*, charge e^* and density n^*. The charge of the superelectron is either negative (for electron-like) or positive (for hole-like). These quantities are related to those of normal electrons as shown below.

$$m_s = 2m^* \quad e_s = \pm 2e^* \quad n_s = \frac{1}{2}n_e \tag{3.2}$$

GL theory determines the superelectron density and distribution within a material through solving the two GL equations. These equations come from minimising the Gibb's Free energy in equation 3.3 with respect to variations of the order parameter and the magnetic vector potential. The two GL equations are given by equations 3.4 and 3.5.

$$G_s(\psi) = G_n + \frac{1}{V}\int d^3\mathbf{r}\left[\frac{1}{2m^*} \times (i\hbar\nabla - e^*\mathbf{A})\psi^* \cdot (-i\hbar\nabla - e^*\mathbf{A})\psi \right. \\ \left. + \left(\frac{1}{2\mu_0}\right) B^2(r) - \mu_0\mathbf{H(r)} \cdot \mathbf{M(r)} + \alpha|\psi|^2 + \frac{1}{2}\beta|\psi|^4 + ...\right] \tag{3.3}$$

$$\frac{1}{2m^*}(i\hbar\nabla + e^*\mathbf{A})^2\psi + \alpha\psi + \beta|\psi|^2\psi = 0 \tag{3.4}$$

$$\nabla \times (\nabla \times \mathbf{A}) + \frac{i\hbar e^*}{2m^*}(\psi^*\nabla\psi - \psi\nabla\psi^*) + \frac{e^{*2}}{m^*}\mathbf{A}|\psi|^2 = 0 \tag{3.5}$$

The results from solving these two equations agree with many of the thermodynamic calculations made for superconductors. The success of GL theory is also highlighted in the fact that the coherence length, penetration depth and the fluxon all fall out as natural parameters of the theory. Furthermore, despite the two different approaches, it was shown that GL theory is actually a limiting form of BCS theory at temperatures near T_c. This further added to its success and acceptance as a macroscopic quantum mechanical treatment of superconductivity.

3.2.4 High and Low Temperature Superconductors

Prior to 1986, BCS theory convinced the world that superconductivity could not exist beyond 30 K. The community was however shocked and surprised at the finding of barium-doped La_2CuO_4 with a T_c just above 30 K [54]. This led to continuous attempts to raise T_c further.

From simply testing various combinations of different atoms, superconductivity was found by adding a rare earth element to the perovskite structure $BaCuO_3$, and this was found to have a T_c of above 90 K [55]. This led to the discovery of the set of materials that were ceramic, anisotropic, and based on copper oxide, and exhibited superconductivity at high temperatures near 100 K [56]. These materials are presently known as the HTS superconductors.

Despite the breakthroughs, it was still not understood how to explain HTS materials theoretically. Improved understanding of BCS theory however has shown that superconductivity in HTS can be explained if the extreme anisotropy is accounted for, where previously BCS theory considered only isotropic cases. This significantly raises the level of difficulty as the mass of the charge carriers are now described differently along the x, y and z axes, and the super electrons originate from, and move within, the copper-oxide planes only, with restricted motion between planes. Therefore, the theory of HTS is complex, however the materials themselves are extremely useful [55].

HTS materials are named as such because they are superconducting when cooled with liquid nitrogen (boiling point of 77.347 K), as opposed to LTS materials which must be cooled with expensive liquid helium (boiling point 4.2 K) in order to superconduct. This means that refrigeration costs for HTS can be reduced [57], even by a factor of 1000 [55], making them more desirable for industrial applications. HTS materials also generally have a much higher critical surface than LTS materials (see Fig. 3.3), allowing them to produce stronger fields and operate at higher temperatures [58]. The problems with

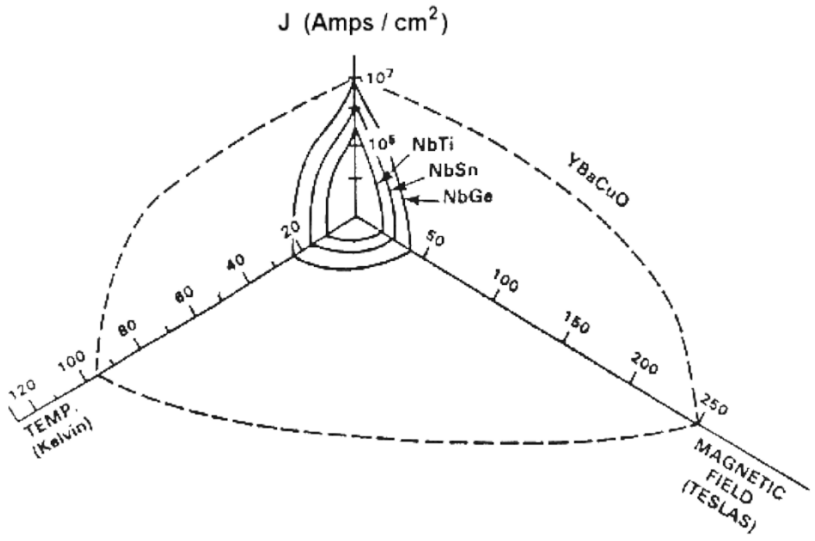

Figure 3.3: The critical surface of LTS and HTS superconducting materials [60]. J_c is of the REBCO layer and not the entire tape.

HTS materials include their brittleness, because they are ceramics, and their requirement for precise grain alignment to allow supercurrent to flow. The need for high grain alignment in HTS is due to the small value of ξ in HTS, and the fact that a grain boundary is an insulating layer with a dimension greater than the HTS ξ, creating a weak link and current blocking effect. This problem does not occur in LTS as ξ is much bigger. The other reason for grain alignment in HTS is purely due to the anisotropy of the unit cell and the restriction of current to the 2D CuO planes [59].

As the useful qualities of HTS materials strongly outweigh their drawbacks, these materials are being developed and used in many industrial applications. These applications include MRI scanners, particle accelerators, and magnetic confinement fusion reactors [61]. The rest of the chapter, and this thesis, will concentrate on understanding and characterising one of the more promising HTS materials, namely REBCO, and its application in magnetic confinement

fusion reactors. REBCO is popular due to its much larger irreversibility field H_{irr} than the other HTS materials, where H_{irr} is the applied field at which flux motion is significant, and its ability to be deposited as a thin film and hence made into flexible cables [62].

3.3 Rare Earth Barium Copper Oxide (REBCO)

3.3.1 REBCO Unit Cell

The Rare-earth Barium Copper Oxide ($REBa_2Cu_3O_{7-\delta}$, also known as REBCO) unit cell consists of three perovskite units ($BaCuO_3$, $RECuO_2$ and $BaCuO_2$) stacked on top of each other (see Fig 3.4) [53]. This means its c lattice parameter is approximately three times larger than the a lattice parameter. The rare-earth element used can be any, but for commercial purposes is usually Yttrium as YBCO was the first superconductor discovered that has a critical temperature above the temperature of liquid nitrogen. The REBCO unit cell consists of CuO planes separated by insulating layers; the CuO planes are responsible for the superconductivity and the flow of Cooper pairs, and the insulating layers supply the charge carriers to the CuO layers [63]. The two types of CuO planes are the puckered CuO_2 layers, and the flat CuO chains, both of which contribute to the superconducting properties.

REBCO comes in a tetragonal and orthorhombic form, with the orthorhombic unit cell shown in Fig. 3.4. The tetragonal form contains extra oxygen atoms in the chain layer, where the orthorhombic form only has oxygen atoms along the b direction forming the CuO chains. It is however only the orthorhombic phase which is superconducting [55], and the oxygen vacancy along the a direction causes $a < b$. The dimensions of the unit cell are $a = 0.382\,\text{nm}$, $b = 0.388\,\text{nm}$, $c = 1.168\,\text{nm}$ [62].

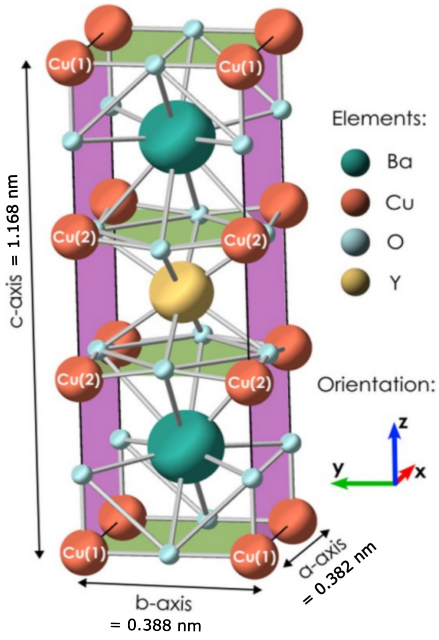

Figure 3.4: The unit cell of YBCO [65].

The oxygen content in the unit cell is important as this is closely linked to the superconducting performance of REBCO [64]. The δ indicates that a fraction of the expected oxygen content is missing, and this value affects the T_c, where the maximum T_c is 92 K when $\delta = 0.15$. When $\delta = 0.5$, there is an equal chance of vacancies to appear along the a and b directions, causing the unit cell to have square symmetry (tetragonal) [55]. The supercurrent is conducted by holes formed at the oxygen sites of the CuO_2 planes, and the oxygen occupancy at the chain site influences the carrier density in the CuO_2 planes [62].

3.3.2 REBCO Coated Conductor Manufacturing Processes

To manufacture bulk REBCO means stacking many unit cells together. However, as mentioned previously, supercurrent flows only when the unit cells are closely aligned and the grain boundary angles are low. But to achieve a perfect, single crystal lattice, or a low grain boundary angle polycrystalline material is very difficult, and hence REBCO is difficult to manufacture in bulk.

A solution to the problem involves growing a thin layer of REBCO epitaxially onto a substrate with an appropriate texture [66]. The problem is that it is very hard to produce a flexible kilometer long single crystal to use as a template [67], so generally the texture is a biaxial one with a grain misalignment of $< 3^\circ$ [68] formed in the substrate or buffer layer. The REBCO is grown epitaxially along its c-axis and develops a biaxial texture in its ab plane. This is the concept behind the second generation (2G) HTS, or the REBCO coated conductor (CC) shown in Fig. 3.6. As the REBCO layer is thin and deposited on a flexible substrate, it is possible to also bend the REBCO tape despite its brittleness. In this way REBCO CCs can be wound to form strong superconducting electromagnets for use in Tokamaks.

The role of each layer in the CC will now be discussed.

Substrate

The substrate forms the mechanical backbone of the conductor, providing it with strength. The substrate can also provide the textured template required for REBCO growth, in this case, the substrate is textured using a process called the Rolling-Assisted Biaxially Textured Substrate (RABiTS) [69], shown in Fig. 3.5. If not forming the template, then the substrate is simply a smooth electroplated surface. Common materials for the sub-

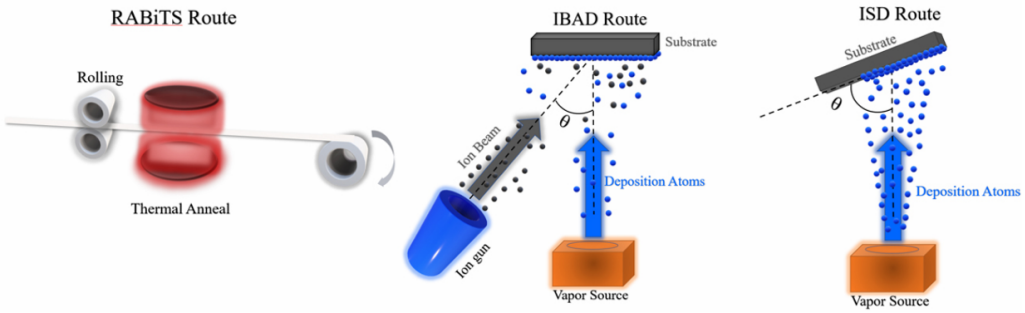

Figure 3.5: The three techniques to generating a biaxial template for REBCO epitaxial deposition in coated conductors.

strate include nickel, nickel alloys, copper or steel [70]. Hastelloy C-276 is a Ni-based alloy and a popular substrate as it is not susceptible to heat and oxidation, [71], and has outstanding mechanical properties [72].

Buffer Layers

The buffer layers are deposited on top of the substrate and collectively form a seed layer, a barrier layer and a template layer [73]. The first seed layer simply forms the base on which to deposit the other buffers layers, which are generally oxides, onto the substrate [74]. The role of the barrier layer is then to prevent atomic diffusion between the REBCO layer and substrate. Diffusion can occur during the deposition of the REBCO in an oxygen atmosphere at high temperatures, whereby the substrate can oxidise and damage the REBCO layer, or diffusion can occur of the metal ions from the substrate up into the REBCO [69]. The third template layer only exists if the substrate has not been used to produce texture (i.e. by RABiTS), otherwise no texture layer is needed. Texture in the buffer layer is achieved using either Ion Beam-Assisted Deposition (IBAD) [75] or Inclined Substrate Deposition (ISD) [76].

REBCO Layer

After deposition of the buffer layers, the REBCO is grown on top of the buffer layers epitaxially as a thin layer of about 1 µm. The REBCO crystal matches the template produced by the buffer layer (or substrate) textured template. The REBCO can be grown using several methods, including Pulsed Laser Deposition (PLD), Metal Organic Chemical Vapour Deposition (MOCVD), reactive electron beam co-evaporation (RCE) and metal organic deposition (MOD) [77]. The REBCO can be grown either in situ, which is a one-step process involving no additional post-thermal treatment, or ex situ, which first deposits the precursors and then requires a post-thermal treatment to complete the crystallisation of the REBCO [78]. In situ processes (e.g. PLD and MOCVD) can produce high quality films with high J_c values, and Ex situ processes (e.g. RCE and MOD) are simple, low-cost, and easy to scale up [79].

Silver and Copper Layer

A thin layer of silver, followed by a thicker layer of copper then coats the whole tape to produce the CC. The silver is deposited usually by sputtering and protects the REBCO whilst providing good electrical contact, also allowing oxygen to diffuse into the REBCO during an oxygen anneal [80]. The copper adds additional reinforcement and also carries away the current when the REBCO loses superconductivity to mitigate quenching. The copper is usually deposited using electroplating technology.

Commercial Manufacturers of REBCO CC

Table 3.1 gives a list of common manufacturers of REBCO CCs and the methods used to fabricate each layer [82]. These superconducting tapes have J_c values of up to $1\,\mathrm{MA/cm^2}$ and T_c values of 90 K.

The current obstacles affecting all manufacturers in their production of the

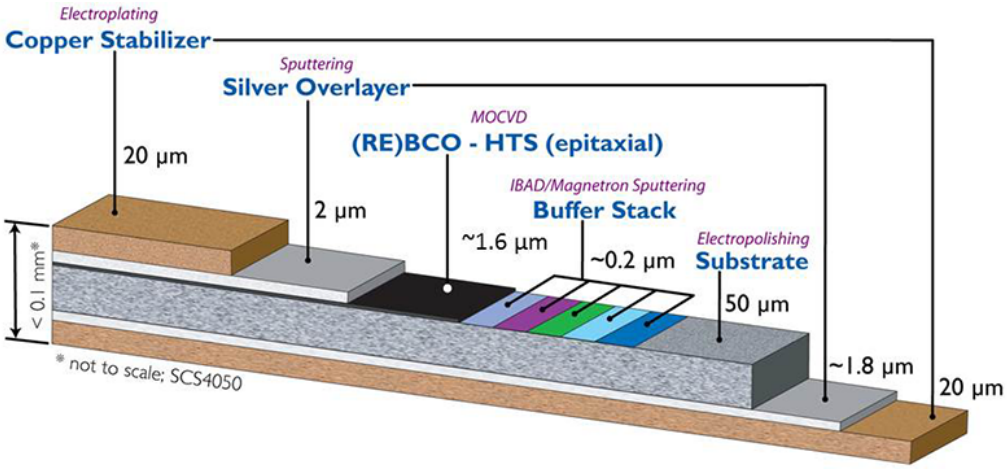

Figure 3.6: REBCO coated conductor type SCS4050 manufactured by SuperPower [81].

CCs is the difficulty in manufacturing tapes with even higher J_c values and in longer lengths. To manufacture CCs with higher J_c values for a given tape width requires depositing a thicker layer of REBCO and optimisation of the pinning landscape [66]. The problem however is the degraded microstructure and increased quantity of current-blocking defects, especially a-axis grains [83], that come with increasing the REBCO thickness leading to a reduced J_c [67], [84]. Even with high-J_c, the tapes must be manufactured in long enough lengths in order to be wound around to form a magnet. The first 1 km length REBCO tape was developed by SuperPower in 2008, and now most companies are able to produce long-length (> 1000 m) REBCO CCs [85].

For the use of REBCO CCs in MCF reactors it is vital to reduce the cost of manufacturing and scale up the production [66]. It currently costs around \$100 kA/m to manufacture the tapes, but this figure is expected to fall to \$10 kA/m with improved technology and stiffer competition among manufacturers [73]. The total world production of REBCO is also increasing as shown in Fig. 3.7. For example, in 2023 SuperPower has doubled their pro-

Table 3.1: Manufacturers of commercially produced REBCO CCs and their manufacturing routes.

Manufacturer	**Substrate**	**Buffer Layers**	**REBCO Layer**
SuperOx, Faraday Factory	Polished	IBAD	PLD
Fujikura	Polished	IBAD	PLD
Shanghai Superconductor	Polished	IBAD	PLD
SuperPower	Polished	IBAD	MOCVD
Theva	Polished	ISD	RCE
SuNAM	Polished	IBAD	RCE
American Superconductor	RABiTS	Sputtering	MOD

duction capacity from 120 km/yr to 240 km/yr [86], and in 2025 there has been over 5000 km of 12 mm REBCO CC produced over half of which was from PLD deposition [87]. This increase in production rate is vital for the success of REBCO magnets in MCF reactors, for example, SPARC alone will require approximately 10 000 km of 4 mm wide REBCO tape [88]. Therefore, the success of MCF fusion depends largely on the success of the REBCO CC manufacturing.

SuperPower 2G CC

In this thesis work, the SuperPower® 2G HTS Tape SCS4050-AP tape [89] provided by SuperPower was used and is shown in Fig. 3.6. SuperPower uses IBAD to fabricate the third buffer layer which is MgO and generates most texture [90], it then deposits all the other buffer layers using magnetron sputtering, and the substrate onto which they are deposited is electropolished Hastelloy C-276 substrate. After the buffer layers have been deposited, the REBCO layer is deposited via MOCVD where the tape is passed across a heated surface and the precursor vapour reacts to form the REBCO on the textured surface. The vapour also contains Zr, which forms BZO columnar structures in the film, to act as artificial pinning centres (APCs) to trap magnetic flux [86]. After deposition of the REBCO, the superconductor is

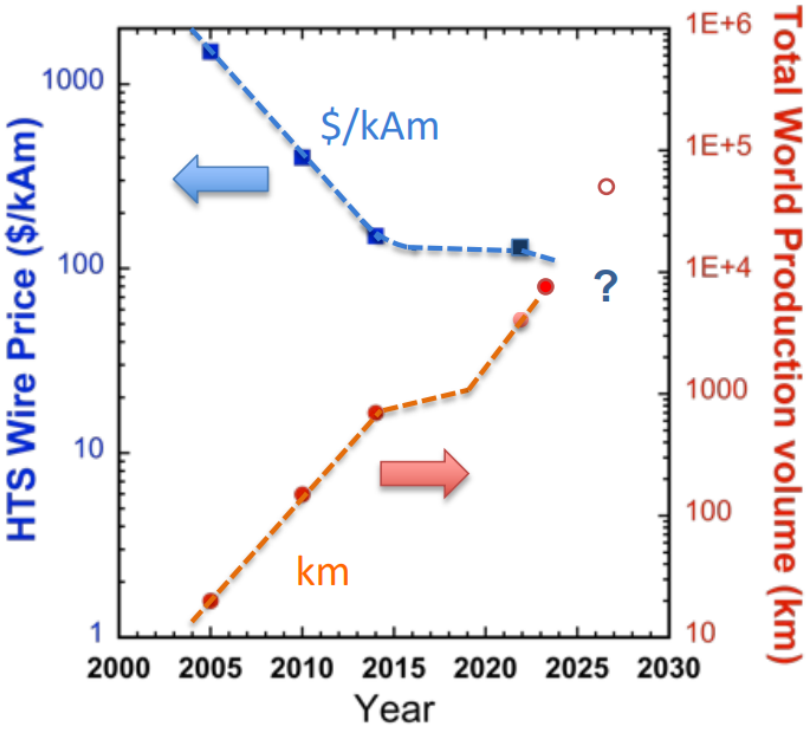

Figure 3.7: Cost of REBCO CC production (blue) and total world production (red) over the last 20 years [73].

coated with the silver layer using cylindrical magnetron sputtering on tapes that are 12 mm wide. The tapes are then mechanically cut to various widths after which the copper stabilizer is deposited using electroplating [80].

3.3.3 Microstructure of the REBCO Layer in the CC

The way in which REBCO films are grown, and whether grown in-situ or ex-situ, strongly affects the microstructure of the REBCO layer [67]. For example, PLD tapes have a wide range defect pinning structures, whereas MOCVD and RCE produce relatively poor inherent pinning structures [85].The microscopic components are shown in Fig 3.8. These natural components are in-

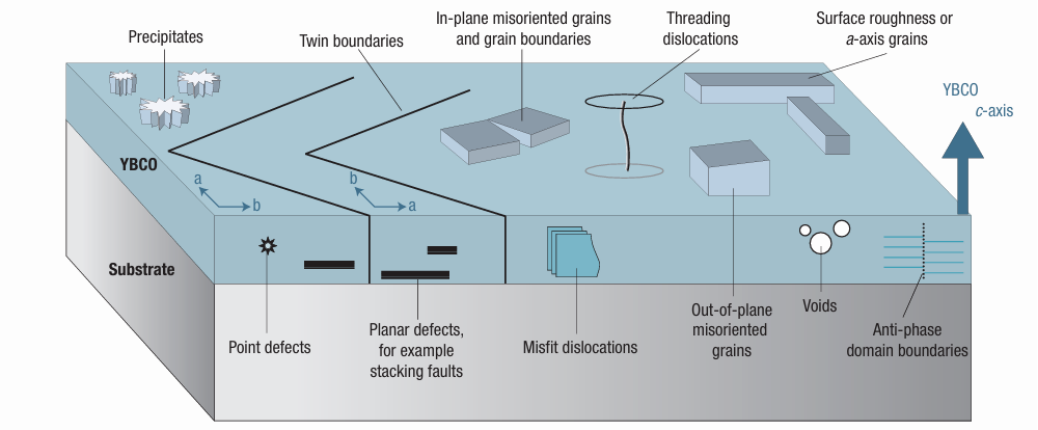

Figure 3.8: The components present in the microstructure of the REBCO layer in coated conductors.

corporated in order to produce positive effects, providing additional pinning to the fluxons and increasing J_c [78], e.g. point defects and grain boundaries. However, some components can instead obstruct the current and lower J_c, such as a axis grains [91]. The components that are present in the SuperPower tapes will be described in terms on their origin and their effects on the performance of the tapes.

Grains and Grain Boundaries

Grains and grain boundaries in the REBCO layer result from the non-uniform growth of the crystal during the REBCO crystallization process. A grain boundary separates two REBCO regions (grains) which have slightly different crystallographic orientations, and can provide excellent pinning provided the grain boundary angle is small. This is because the misalignment of the a and b axis at the grain boundaries generates strain and dislocations which enable vortex pinning and enhanced J_c [62]. If the grain boundary angle is too high however, above 4°, then the interface effectively becomes a Josephson Junction leading to weak coupling and a reduced J_c [92].

Precipitates and a axis Grains

These defects have the primary effect of reducing J_c as they block the current path, effectively reducing the cross sectional area. The precipitates formed are usually secondary phases such as Y_2O_3 and CuO [93] and can reduce I_c by reducing the area [94], but can also contribute to flux pinning [62]. The a axis grains are needle-like particles that have their c axis rotated by 90°. They are generally 5 µm in size and penetrate through the full thickness of the REBCO layer [95], and they are orientated along the tape length or perpendicular to it. The a axis grains usually form when the deposition temperature of the REBCO layer is low; the grains are typically a-axis orientated at $T = 780\,°C$ and shift to being c-axis orientated at 790 °C [96]. The a axis grains have been shown to block current [97] as well as lower the pinning force F_p in the tapes by 40 % [98]. The a axis grains become more prevalent in REBCO films over 1 µm in thickness [91], limiting the J_c of thick films.

Point and Columnar Defects

Point defects are usually on the nanometer scale and offer the best pinning due to their similarity in size to the vortex size; the column diameter is typically 5 - 10 nm and the magnetic vortex core diameter is ≈ 2 nm [99]. SuperPower add Zr to the precursor mix which forms $BaZrO_3$ (BZO) columns in the superconductor film along the c axis [77]. These artificial pinning sites (APCs) are very effective at trapping flux and provide significant enhancement in J_c. The effectiveness of the APC pinning however depends on the applied field, since higher fields create fluxons that are closer together, therefore requiring a higher APC density to effectively trap all these fluxons. Therefore the optimum APC density depends on applied field, angle of the c axis to the field, as well as temperature [99]. For example, for the APC SuperPower tape, 15 % Zr tapes have a lower J_c than 7.5 % Zr tapes below 2 T, but a higher J_c above 2 T [100].

Domains and Twin Boundaries

Twin boundaries arise from the formation of an anisotropic crystal of REBCO. In MOCVD, REBCO crystals are grown from oxygenation of the REBCO at a high temperature by passing the deposited precursors along a heated surface [101]. The formation of the tetragonal REBCO phase occurs between 700 - 900 °C, and slowly cooling it in an oxygen atmosphere to 500 °C causes a phase change to the orthorhombic phase, and this releases a lot of stress [62]. This release of stress results in some parts of the REBCO having their a axis aligned along the length of the tape, but some other parts having their b axis aligned instead [102]. Regions where the a axis is aligned along the length of the tape are called A domains, and those with the b axis aligned are called B domains. The boundary separating the two domains is called a Twin Boundary (TB). As the crystals are grown on a cubic lattice template (MgO), it is energetically quite easy for propagation to switch from a to b [55], leading to a REBCO layer of which approximately 50 % of the area consists of A domains, and 50 % of B domains [103].

The orientation of the twin boundaries and of the domain axes depends on the deposition route of the REBCO layer; i.e. MOCVD tapes have the a and b axes oriented along the tape length, whereas ISD tapes have them oriented at 45° to the tape length [104]. The structure of the domains for the MOCVD route REBCO tapes is shown in Fig. 3.9. This tape consists of grains a few micrometers in size, and within the grains are microtwins that are twinned along the {110} planes and with a width of a few hundred nanometers [105].

Twin boundaries can affect flux pinning, causing flux motion easily along the boundaries but not across them. The domain structure of the tape also affects the response of REBCO under strain which will be discussed in section 3.4.

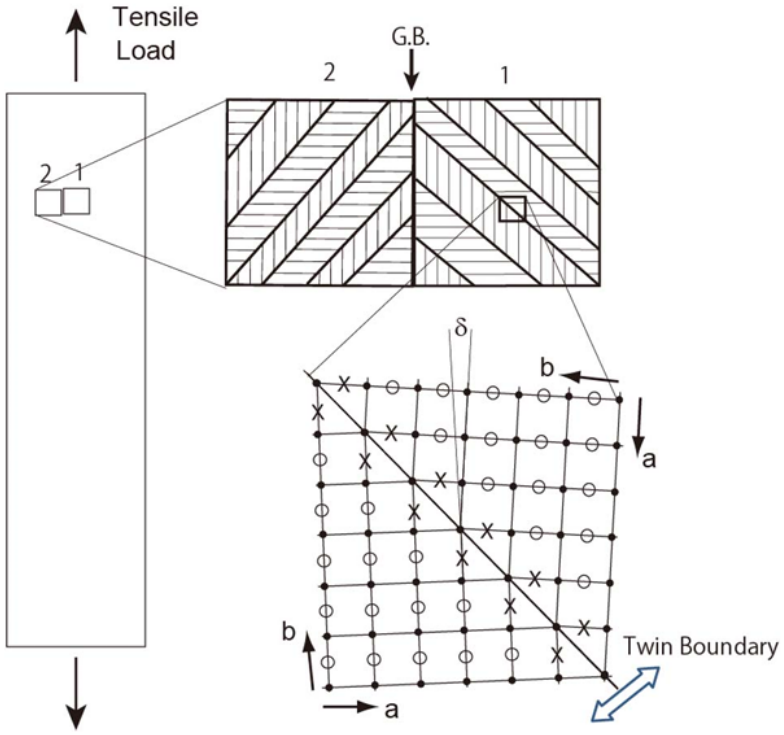

Figure 3.9: The structure of the domains and twin boundaries within the grains in the REBCO layer of IBAD-MOCVD tapes [105].

3.4 The REBCO CC Critical Current Density Dependencies and Links with Microstructure

After having explained the structure of the REBCO CC, including the overall tape structure and REBCO layer microstructure, we will now look at how this structure gives rise to a J_c of the tape that has specific dependencies on the magnetic field, angle between the c axis and the field, and an applied strain, with focus specifically on the SuperPower APC tape.

3.4.1 Field Dependence

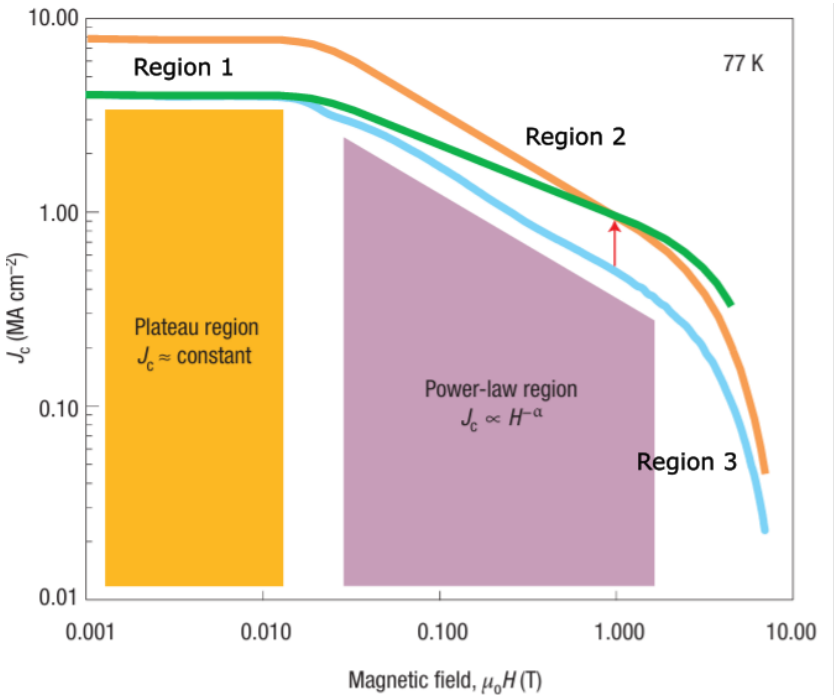

Figure 3.10: J_c versus applied magnetic field for a REBCO CC (blue). The curve but with double the self field is shown in orange, and one with a smaller α is shown in green [67].

The dependence of J_c on magnetic field is divided into three regions as shown in Fig. 3.10 [67]. Region 1 appears as a low-field plateau in J_c. In region 2 there is a smooth decrease in J_c with applied field which can be characterised by a power law: $J_c \propto B^{-\alpha}$. Typical values of α have been found to lie between 0.55 and 0.75 with values that depend on the manufacturing route [106]. Finally in region 3 there is a steep drop in J_c at fields higher than the irreversibility line.

Region 1 is known also as the single vortex pinning regime, because the small applied field results in the vortex density being much less than the density of the APCs, and hence the vortices barely interact with each other [107]. In

region 2, vortex-vortex interactions become relevant, and a linear decrease in J_c with increasing field in log-log space is observed. Region 3 then begins as the irreversibility field is reached [108].

A mathematical treatment of the JJ model, from which the field dependence of J_c emerges, will be presented in section 3.4.4.

3.4.2 Angular Dependence

The origin of the dependence of J_c on the angle between the magnetic field and the tape normal in an applied field is fundamentally due to the anisotropy of the REBCO unit cell [109]. Some features of the angular dependence are also due to the manufacturing route of the CC. The distinct shape of the J_c versus angle curve depends strongly on the temperature and the magnitude of the applied field for a given manufacturer [110].

The main feature of the angular dependence is a large increase in J_c at $90\,^\circ$ when $B \parallel ab$ plane [110], and this anisotropic behavior exists in REBCO CCs from many different manufacturers as shown in Fig. 3.11. This peak is due to the pinning of fluxons between the CuO layers when the field is applied parallel to the ab plane. The pinning between planes creates trapped staircase vortices which enhances J_c causing a peak in the angular distribution [109].

The second feature of the angular dependence is a second peak located at $0\,^\circ$ when $B \parallel c$ axis, seen also in Fig. 3.11. This peak is apparent in tapes that have added impurities that create columnar defects parallel to the c axis [111]. In the SuperPower APC tapes, these columnar defects are from $BaZrO_3$ (BZO) doping [80].

Some other features of the angular distribution include a slight offset of the $B \parallel ab$ peak from 90° by about 2° for the IBAD-MOCVD tapes. This occurs because the REBCO is deposited with a small vicinal tilt; the ab-planes are tilted with respect to the tape surface by an angle of around 2° [112], [113].

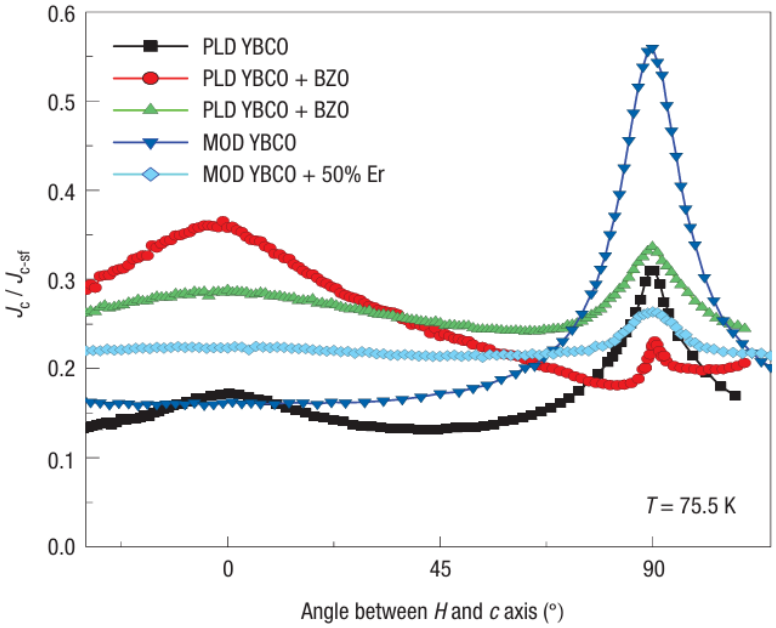

Figure 3.11: J_c normalised to self-field values (J_{c-sf}) versus angle between the applied field and tape c axis for various REBCO CCs made from different manufacturing routes [67].

3.4.3 Strain Dependence

The J_c dependence on a uniaxial strain applied parallel to the tape length depends on the twinned structure of the REBCO layer. As mentioned in section 3.3.3, due to the release of stress from the tetragonal to orthorhombic phase transition of the REBCO unit cell during manufacturing, many domains are created with neighboring domains having their a-axis aligned perpendicularly.

Previous work on detwinned REBCO tapes has found that the J_c dependence on strain is different for the A and B domains. Applying a strain parallel to the a-axis causes J_c and T_c to decrease in compression, whereas applying it parallel to the b-axis causes J_c to increase in compression [114], [115]. The J_c dependence on strain for the two domains found experimentally in [114]

is shown in Fig. 3.12.

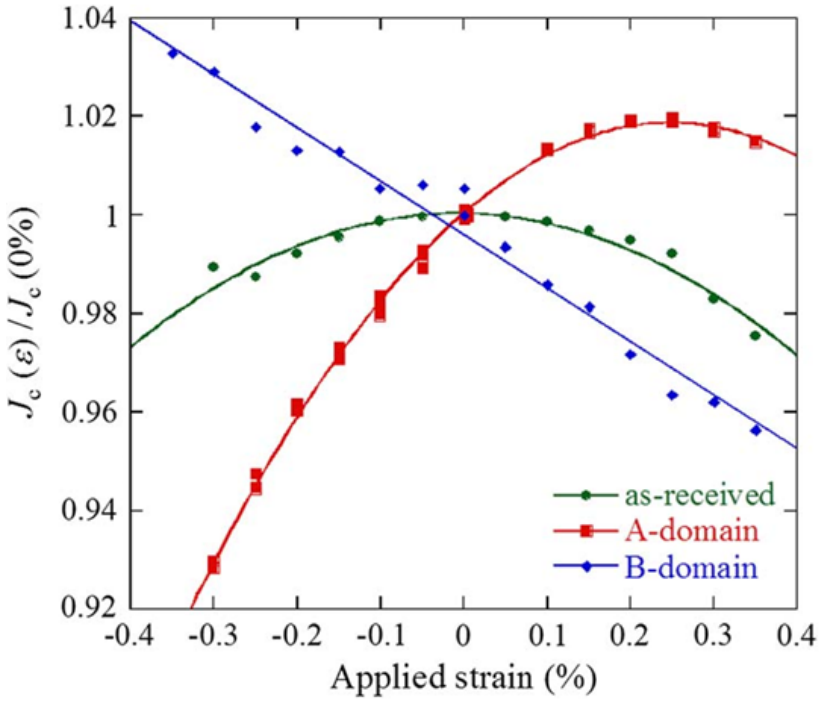

Figure 3.12: Normalised J_c versus strain for SuperPower APC REBCO tape twinned with the a-axis along the tape (red), the b-axis along the tape (blue), and for a normal tape with no annealing (green) [114].

The overall strain dependence of a full-width REBCO tape depends on the precise map and orientation of the domains. It is well known that for the IBAD-MOCVD route, the J_c has an inverse parabolic dependence on strain for a uniaxial strain applied along the tape length [116]. However, for the ISD route for REBCO deposition, where the a and b-axis are 45° tilted from the direction of the tape [104], there is only a very weak strain dependence on J_c [117], [118]. These different dependencies can be explained by the bimodal chain model described below.

The Bimodal Chain Model

The bimodal chain model was developed to determine $J_c(\varepsilon)$ for a uniaxial strain applied along two twinned domains A and B connected in series with domain fractions f and $1-f$ respectively [103]. The model works specifically for the case where the A and B domains are oriented along the direction of the uniaxial strain and current, such that the current has to flow repeatedly across these A and B domains [104].

We start by quoting the well known power law for the electric field E produced by a superconductor carrying a current I in equation 3.6, where E_c and n are the electric field criterion and index of transition respectively.

$$E = E_c \left(\frac{I}{I_c} \right)^n \tag{3.6}$$

When the bimodal chain model was first developed, it was assumed that the strain dependence of I_c in each domain was linear but opposite and given by equation 3.7.

$$I_{ci} = \begin{cases} I_c(0)(1 + g_A\varepsilon), & i = A \\ I_c(0)(1 - g_B\varepsilon), & i = B \end{cases} \tag{3.7}$$

Where $g_A = g_B$.

However, actual measurements of the J_c dependence on strain within each domain for detwinned REBCO found the strain dependencies of each domain to be slightly different (shown in Fig. 3.12), with the A domain instead showing a parabolic behaviour with the dependencies of each domain given in equations 3.8 and 3.9 [114].

$$I_{c,A} = I_{c,A-max} - I_{c,A}(0) g_A (\varepsilon - \varepsilon_{A-max})^2 \tag{3.8}$$

$$I_{c,B} = I_{c,B}(0)(1 - g_B \varepsilon) \tag{3.9}$$

The electric field generated by the chain is then given by the sum of the electric fields from both domains.

$$E = E_c f \left(\frac{I}{I_{cA}} \right)^n + E_c (1 - f) \left(\frac{I}{I_{cB}} \right)^n \tag{3.10}$$

Equation 3.10 assumes that n is the same in both domains. When $E = E_c$ (and hence $I = I_c$) and we substitute the strain dependencies of I_c for each domain, where here we use the original linear strain dependencies given in equation 3.7, equation 3.10 then becomes

$$1 = f \left(\frac{I_c}{I_c(0)(1 + g_A \varepsilon)} \right)^n + (1 - f) \left(\frac{I_c}{I_c(0)(1 - g_B \varepsilon)} \right)^n \tag{3.11}$$

Equation 3.11 can be used to determine I_c as a function of ε if the constants $I_c(0)$, n, f and g are known. For the IBAD-MOCVD REBCO tapes, and most other tapes, the fraction of area occupied by the A and B domains is roughly equal, such that $f = 0.5$ [103], and hence the solution to equation 3.11 is an inverse parabola centered at $\varepsilon = 0$, as shown in Fig. 3.12. In this model, when $f > 0.5$ we expect the peak in the strain to shift towards the tensile region, and when $f < 0.5$ it instead shifts to the compressive side.

For the ISD route, the domains are rotated 45° to the direction of the applied strain, and so the strain response in each domain is now similar, and hence there is only a weak strain dependence on J_c for these tapes [117].

3.4.4 The Josephson Junction (JJ) Model

Here we present a parametrisation of the $J_c(B, T, \theta, \varepsilon)$ data using a Superconducting-Normal-Superconducting (SNS) Josephson-Junction (JJ) model. This model includes the wave-particle duality of the superelectrons, and takes into account the barriers of normal material present in superconducting materials, which both serve as pinning sites for the fluxons and act as barriers through which fluxons must quantum tunnel. Standard scaling laws do not take these complexities into account, and are found to break down when trying to parameterise HTS materials.

The JJ model is presented in equation 3.12 [119]. It represents the limit where the normal barrier width w_s is on the order of the fluxon-fluxon spacing, resembling the high field limit, but the barrier thickness is large. In this case, we are referring to region 2 of the J_c versus field plot shown in Fig. 3.10.

$$J_c(B, T, \varepsilon) = \frac{1.2}{c_1} \left(\frac{\phi_0}{B w_s^2} \right)^{c_1} J_s \left(1 - \frac{B}{B^*_{c2}} \right)^{3/2} \frac{1 - \sqrt{1 - \tilde{s}\tilde{f}^2_{d/2}}}{\tilde{s}\tilde{v}} \exp\left(\frac{-\tilde{d}}{\tilde{\xi}_n} \right) \tag{3.12}$$

Where ϕ_0 is the quantum of flux, c_1 a constant and ξ the coherence length. The $J_c(B)$ power law emerges in the first part of 3.12, where $J_c \propto (1/B)^{c_1}$. The ε dependence of J_c arises from the ε dependencies on the effective critical temperature (T^*_c) and hence effective upper critical field (B^*_{c2}), the junction thickness (d), and junction width (w_s) given by equations 3.13, 3.14 and 3.15 respectively.

$$T^*_c(\varepsilon_{app}) = T^*_c(0) \exp\left(1 - (1 + c_{\varepsilon 1}\varepsilon_{app} + c_{\varepsilon 2}\varepsilon^2_{app})^2\right) \tag{3.13}$$

$$d(T, \varepsilon_{app}) = d(0) + \zeta_1 \left(\frac{T}{T_c^*(\varepsilon_{app})} \right) + \zeta_2 \left(\frac{T}{T_c^*(\varepsilon_{app})} \right)^2 \tag{3.14}$$

$$w_s(T, \varepsilon_{app}) = w_s(0) - \zeta_1 \left(\frac{T}{T_c^*(\varepsilon_{app})} \right) - \zeta_2 \left(\frac{T}{T_c^*(\varepsilon_{app})} \right)^2 \tag{3.15}$$

Where $c_{\varepsilon 1}$, $c_{\varepsilon 2}$, ζ_1 and ζ_2 are fitting parameters for the strain dependencies. The tilde symbols of equation 3.12 denote normalised parameters and the subscripts denote ratios of the normal parameter values to the superconducting electrode ones, for example $\tilde{\xi}_n = \xi_n/\xi_s$ and $\tilde{d} = d/\xi_s$.

Within the magnetic field dependence on J_c there is a temperature dependent cross-over field below which J_c is independent of field [120] (see Fig. 3.10). For this low-field region, a flat line up to this cross-over field is fitted to the data.

The other terms of equation 3.12, namely J_s, $\tilde{f}_{d/2}$, $\tilde{s}$, $\tilde{v}$, $\tilde{\xi}_n$ are presented in [119] and are themselves functions of B, B_{c2}^*, $\tilde{\alpha}_n$ and $\tilde{\beta}_n$ (the GL parameters), and include the terms $\tilde{m}_n$ (the normalised effective mass), λ_L (the London penetration depth), w and ν (constants). In chapter 6, we will use the JJ model to fit the J_c data and to find best free fitting parameters and discuss their significance.

3.5 Conclusion

In this chapter we have presented an overview of superconductivity and the development of HTS REBCO tapes that can be formed into very strong magnets for use in MCF reactors.

We began by looking at the theory behind superconductivity with a closer look at the specific case of REBCO superconductors. We then investigated

the process of manufacturing REBCO CCs for application in strong electromagnets for commercial purposes, and how the deposition of the REBCO creates a microstructure that leads to a specific $J_c(T, B, \theta, \varepsilon)$ critical surface.

Understanding the link between the manufacturing route, the microstructure and the critical surface of REBCO tapes is very important in the design of magnets for MCF reactors. In addition, the microstructure of the REBCO tape is important in understanding the results presented in the following chapters. Therefore, the contents outlined in this chapter are very important to grasp.

Chapter 4

Preliminary High Field Results

4.1 Introduction

This chapter presents the results of a preliminary experiment to find the critical temperature as a function of strain $T_c(\varepsilon)$, and the upper critical field as a function of temperature, magnetic field angle and strain $B_{c2}(T, \theta, \varepsilon)$ of 4 mm wide REBCO tapes. The results were presented at the Applied Superconductivity Conference (ASC) 2021 as a poster, and later presented and published as a conference paper.

The motivation of this study was to find $B_{c2}(T, \theta, \varepsilon)$ dependence on temperature, angle and strain for small 7 mm long REBCO tapes using simple resistivity measurements. The use of small currents (maximum 0.1 A) in this experiment enabled the use of a Cold Head [121] and Physical Properties Measurement System (PPMS) [122], and the small sample dimensions (below 10 mm in length) opens up a larger possibility of different measurements that can be done, specifically at much higher, pulsed magnetic fields where the magnet bore size becomes small [123].

Two experiments were performed during this campaign, one of which involved using a Cold Head to measure $T_c(\varepsilon)$, and the other using a PPMS system to measure $B_{c2}(T, \theta, \varepsilon)$. This section will begin by describing the equipment used and the experimental methods. Following this the results of the dependencies will be presented along with a presentation of the theory. Finally, the chapter will end with a discussion of the results.

4.2 Method

Both the Cold Head and the PPMS measurements are described in the following sections.

4.2.1 The Cold Head Measurements

Measuring T_c involved changing and holding fixed the strain, and then changing the temperature in a controlled manner whilst continuously measuring the resistance. A Cold Head is a variable temperature apparatus that was used for this, which cools via expansion and compression of a circulating helium gas.

The Cold Head Hardware

The Cold Head used was a Janis closed cycle refrigerator. It operates by compressing and expanding a closed loop of helium gas following the Gifford-McMahon thermodynamic cycle. The components of the Cold Head are listed below [124].

- Compressor: A unit that feeds high pressure helium gas into the Cold Head.
- Cold Head: The area where the helium gas is cooled, consisting of two stages.

- Gas Lines: Pipes where helium gas is fed to and from the Cold Head.
- Vacuum Jacket: An outer steel vessel surrounding the sample space, allowing it to be held under vacuum within the Cold Head.
- Radiation Shield: An aluminium shield connected to first stage between the sample space and the vacuum jacket. It is used to intercept radiation from room temperature to the sample space to achieve low temperatures ($< 4\,\mathrm{K}$).
- Sample Platform: A copper stage where the sample sits.
- Temperature Controller: An external unit used to control and set the temperature of the Cold Head.
- Thermometry and heating: A thermometer and heater used to measure and control the temperature of the Cold Head.

The high pressure helium gas from the compressor reaches the Cold Head where it is expanded and cools providing cooling to two heat stations. The gas is then returned to the compressor. Heat is drawn away from the sample via conduction through the copper sample platform connected to the second stage, allowing temperatures below $4\,\mathrm{K}$ to be reached.

Varying the Temperature

Good thermal contact of the sample to the sample platform was essential and was achieved by tying the sample down using dental floss into a thin layer of thermal vacuum grease and onto a piece of cigarette paper for electrical insulation as shown in Fig. 4.2 [125]. The temperature of the sample was controlled using the interplay between a silicon diode thermometer and 25 Watt heater located in the second stage. To set the temperature, a model 340 LakeShore temperature controller [126] varies the power output of the heater according to the temperature measured by the diode to overcome

the cooling power and reach the set-point temperature. The time taken for the Cold Head to reach the set-point temperature, and the stability of the temperature at this set-point, is adjusted by varying a set of PID parameters on the temperature controller and typically took around an hour. It was found that PID: 30, 15, 5 was optimum for this setup and this was found simply using trial and error mainly by adjusting the Proportional factor (P). The value of P was lowered in increments until the large oscillations in the thermometer temperature around the setpoint were reduced and the optimum value found when the setpoint temperature was reached smoothly without overshooting (no oscillations).

Varying the Strain

The strain in the REBCO tapes was varied using a miniature, PACMAN style [127] strain board designed, built and commissioned in Durham. The board was made out of beryllium-copper (CuBe) due to its solderability, and its high elastic limit of -1% [128], allowing the board to reach a large, uniform strain range between -1% and 0.5%. The REBCO tape was soldered to the strain board substrate side down using PbSn solder and compressive strain achieved by moving the flanges together, where a central screw and nuts system was used to adjust the flange separation as shown in Fig. 4.1 and 4.2. To determine the strain distribution across the strain board we used the technique of finite element analysis (FEA), which is a numerical method of determining how a structure will behave under certain conditions by breaking it up into smaller elements, using the software Ansys. The strain uniformity at -1% strain is shown using FEA in Fig. 4.3.

The strain in the tape was measured using a small 2 mm long, 120 Ω strain gauge (SG) [129] adhered adjacent to the REBCO tape on the strain board. Applying compression and tension changed the length, and hence the resistance, of the grid, and the resistance was found by dividing the voltage measured across the grid by the small 100 µA current passing through it.

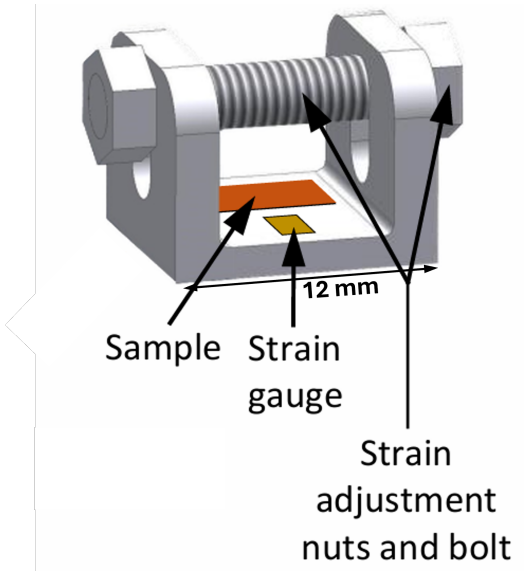

Figure 4.1: A CAD drawing of the PACMAN style strain board. Spanners are used to tighten the outside screws bringing the flanges closer together to apply compressive strain.

The relation between the SG resistance and strain is then given by equation 4.1.

$$\varepsilon = \frac{1}{GF}\frac{R - R_0}{R_0} \tag{4.1}$$

where GF is known as the gauge factor and is provided with the strain gauge by the manufacturer. For the strain gauge used here GF = 1.74.

Uncertainties

There were several uncertainties involved in determining the strain in the REBCO layer. The first uncertainty arose from adhering the SG to the strain board rather than directly to the surface of the tape. A small correction was therefore needed to account for the small increase in distance from

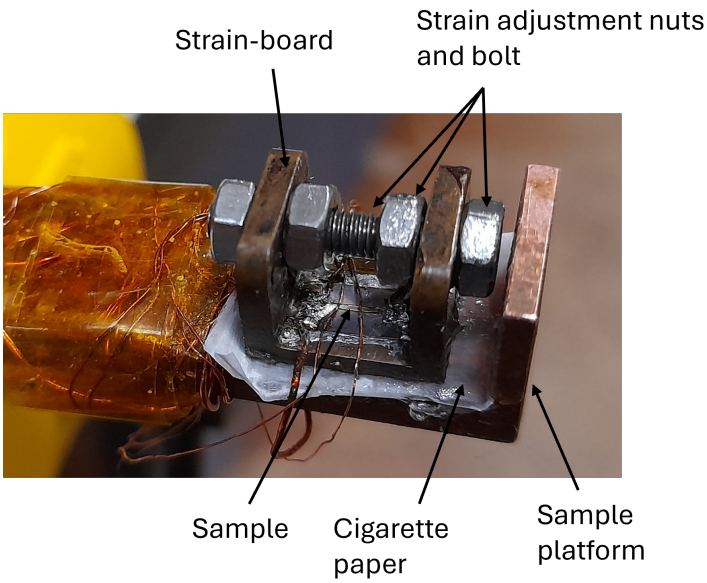

Figure 4.2: Assembly of the strain-board on the sample platform. Tightening of the outer nuts generates compression and tightening of the inner nuts generates tension in the sample.

the neutral axis of the REBCO layer compared to the SG. Simple bending beam geometry was used to determine this, finding the strain magnitude at the REBCO layer to be a factor of 1.013 larger than in the SG such that $\varepsilon_{REBCO} = 1.013 \times \varepsilon_{SG}$ [130]. This calculation relies on the uncertain assumption of there being a full transmission of the strain from the strain board into the REBCO layer through the solder. Furthermore, the additional strains from the differential thermal contractions between the REBCO tape and strain board would not have been picked up by the SG [131], [132]. Accurate knowledge of the REBCO strain would have instead been achieved through adhering the SG directly to the top of the REBCO tape.

Secondly, due to the inability to apply strain during operation of the Cold Head, the strain was applied and measured at room temperature only. However, on cooling, the strain state changes due to the differential thermal

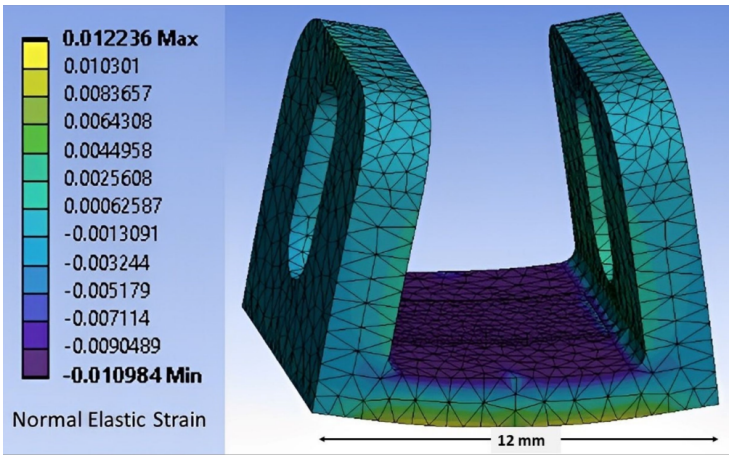

Figure 4.3: Finite element analysis showing the elastic strain distribution within the strain-board when under compression (Side flanges closer together). Good homogeneity is shown (in the region in blue) where the sample and strain gauge are mounted. The strain board is made of CuBe (alloy 25).

contraction between the strain board and the SG grid. The resistance of the SG grid material itself also changes with temperature. Therefore, the cryogenic strain was different from the room temperature strains quoted. To compensate for cooling, the residual strain arising from changes in the temperature-dependent resistance of the SG was subtracted from the room temperature strain values, with the temperature response of the specific SG given by equation 4.2 (T in °C). The differences in the coefficients of thermal expansion of the CuBe and the ferritic steel SG grid were not included in the calculations.

$$\varepsilon_{res} = -33.12 + 2.98T - 7.37 \times 10^{-2}T^2 + 3.04 \times 10^{-4}T^3 \qquad (4.2)$$

The other issue with the application of strain at room temperature was the gradual relaxation of the strain reading over time, especially at higher strains. This was because of the gradual plastic deformation of the solder layer when applying large strains, and this again could not be prevented.

Measuring the Resistivity

T_c was determined from a set of resistance versus temperature graphs. The resistance was calculated from standard four-terminal voltage and current measurements [133]. The current used was 100 mA and the voltage measured using a Keithley 2100 multimeter connected to a 50,000 gain amplifier. The voltage and current connections were soldered to the top of the REBCO tape, and it is expected that some current was shunted through the strain board although this was not measured. To prevent thermal voltages, the current was reversed after every 10 data points and an average of the absolute values of voltage were calculated.

In the case of the Cold Head, the temperature was swept to a set-point at a constant sweep rate both set using the temperature controller, and the voltage was continuously measured during the sweep. T_c was defined as the temperature of the steepest point on the resistance versus temperature graph. Despite T_c generally being at zero current, a current was needed to generate a measurable resistance for the resistivity measurements. Therefore, a small current of 100 mA was chosen, which is small enough to assume that the measured T_c is equivalent to the true T_c of the superconductor.

Due to the large conductive path between the thermometer and the sample along the sample platform, there was a thermal time lag between the sample temperature and the thermometer temperature. This caused the measured

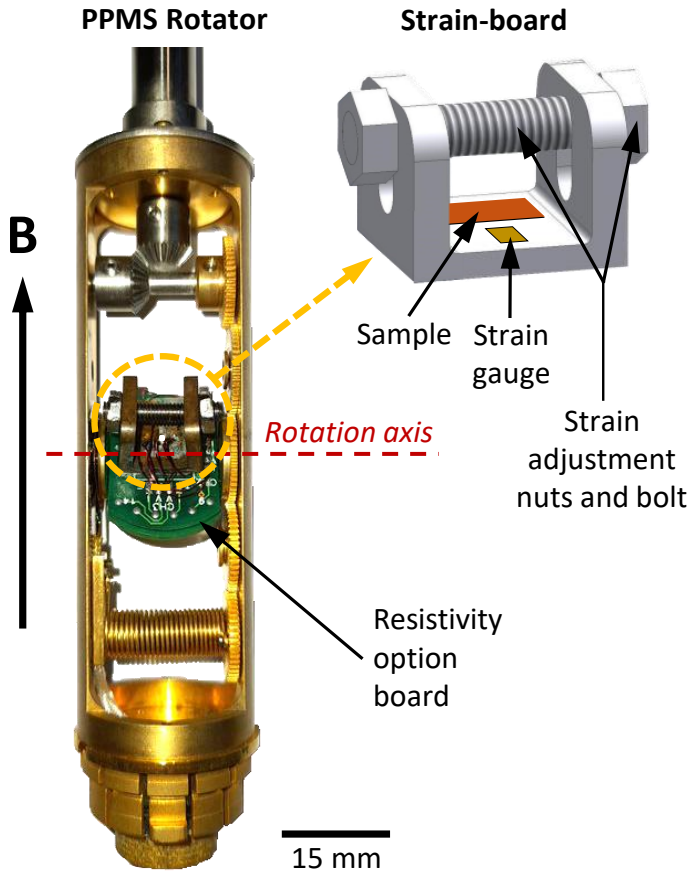

Figure 4.4: PPMS rotator with the strain-board. The sample and strain gauge are attached to the strain-board. The nuts are placed outside the side flanges (as shown) and have to be tightened to apply a compressive strain. The nuts are placed inside the side flanges to apply a tensile strain. The direction of the applied field and the axis of rotation are shown.

T_c to depend on the temperature ramp rate and the direction of the sweep (temperature increasing or decreasing). A faster ramp rate caused T_c to be further from its true value, with sweeping up in temperature causing it to be lower than its true value while sweeping down causing it to be higher. The actual T_c was taken as an average of the up and down sweeps for different ramp rates (see Fig 4.5). The ramp rates chosen were $\pm$ 0.5 K/min, $\pm$ 0.25 K/min and $\pm$ 0.125 K/min.

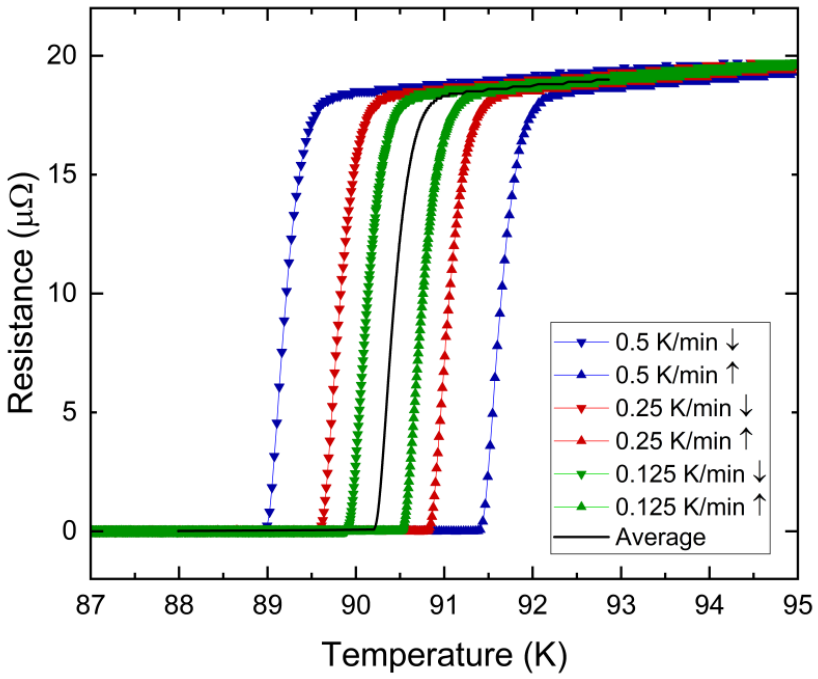

Figure 4.5: Resistance versus temperature measurements for various temperature ramp rates, with the average of all ramp rates, taken to denote equilibrium data, shown in black.

4.2.2 The Physical Properties Measurement System (PPMS) Measurements

For the variable field and temperature measurements, required to find B_{c2}, the PPMS was used. The PPMS is a fully automated low-temperature and variable magnetic field system that can measure material properties like electrical transport properties. It can reach a temperature range of 1.9 K to 400 K by circulating liquid helium, and magnetic field range of 0 - 9 T [122]. The PPMS costs a lot more to operate due to its use of liquid helium rather than helium gas, but was used due to its ability to apply a large magnetic field and hence deduce B_{c2}. To vary the angle of the REBCO c-axis to the magnetic field generated in the PPMS, the sample on the strain board was wired to a specialised PPMS rotator, that enabled variable angle measurements [134] (see Fig. 4.4). The size of the magnet bore limits the sample size to the dimensions of 13 mm by 13 mm.

For the PPMS measurements, the temperature was ramped at a constant rate and the resistance continuously measured. The resistance versus temperature graph was calculated from the average of the increasing and decreasing temperature sweeps. The temperature of a transition was defined as the steepest point on the resistivity curve. Between each sweep, the sample was warmed sufficiently to drive it into the normal state.

4.3 Results and Discussion

4.3.1 $B_{c2}(T, \theta, \varepsilon)$ Measurements

Measurements of the dependence of T_c on strain were first made using the cryocooler. Figure 4.6 shows the resistance versus temperature graphs for three different strains: 0 %, −0.28 % and −0.55 % and a repeat at 0 %.

Afterwards, the dependence of B_{c2} on temperature, strain and angle was

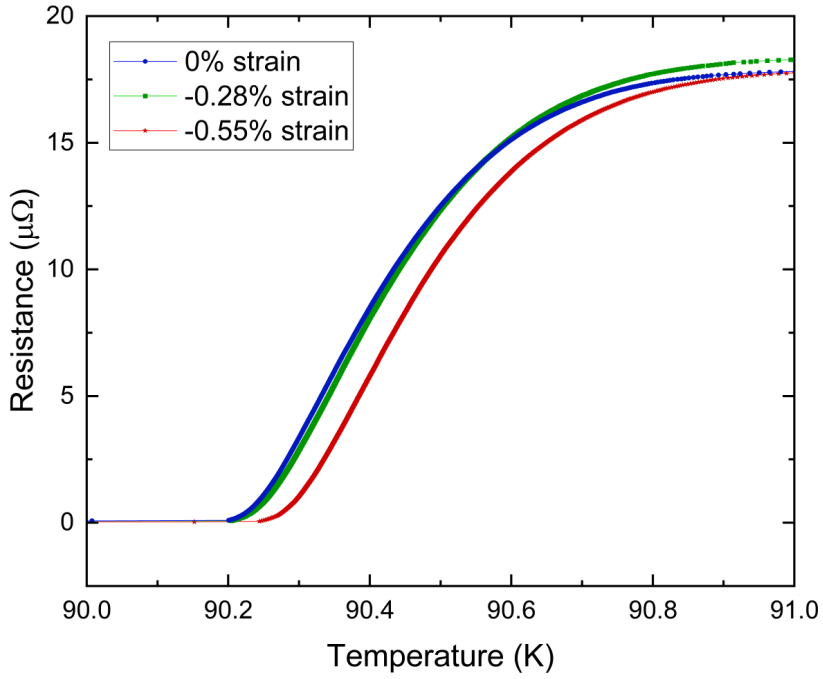

Figure 4.6: Average resistance versus temperature measurements on a RE-BCO tape under strains of 0 %, −0.28 % and −0.55 % taken using the Cold Head.

measured in the PPMS. Resistance versus temperature sweeps were made at magnetic fields from 1 T to 8 T in 1 T intervals at three different angles, 0°, 34° and 60°. This was repeated at three different strains 0 %, −0.55 % and −1.1 %. An example of a set of resistance versus temperature curves for the different fields at 0° and 60° is shown in Figure 4.7. It can be seen that with increasing field, the gradient of the transition decreases. Also at higher angles, the resistance curves are closer together along the temperature axis.

To find B_{c2}, a graph of the applied field versus the respective transition temperature at this field was plotted. A single crystal Klemm equation (see

section 4.3.2) was fitted to the data and extrapolated back to $T = 0\,\mathrm{K}$ to find $B_{c2}(0)$. Figure 4.8 shows the applied field versus temperature data for the different angle and strain combinations along with the Klemm fits.

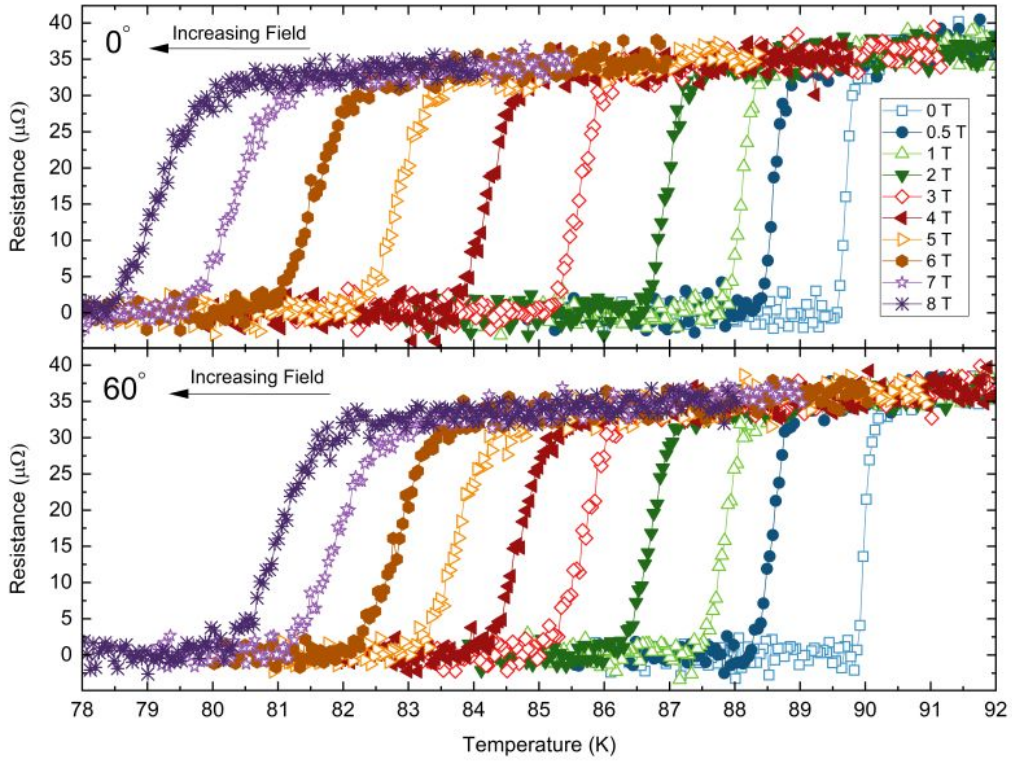

Figure 4.7: Resistance versus temperature measurements on a sample under $-0.55\,\%$ strain for angles between the tape normal and the B-field of 0° (top) and 60° (bottom) taken using the PPMS. Measurements were made in magnetic fields up to 8 T.

4.3.2 Theory

The theory of the temperature and angular dependence of B_{c2} has been found for an anisotropic superconductor for both layered [135], [136], and artificial multilayered systems [137], [138]. It is given by equation 4.3 in the form given by [139] .

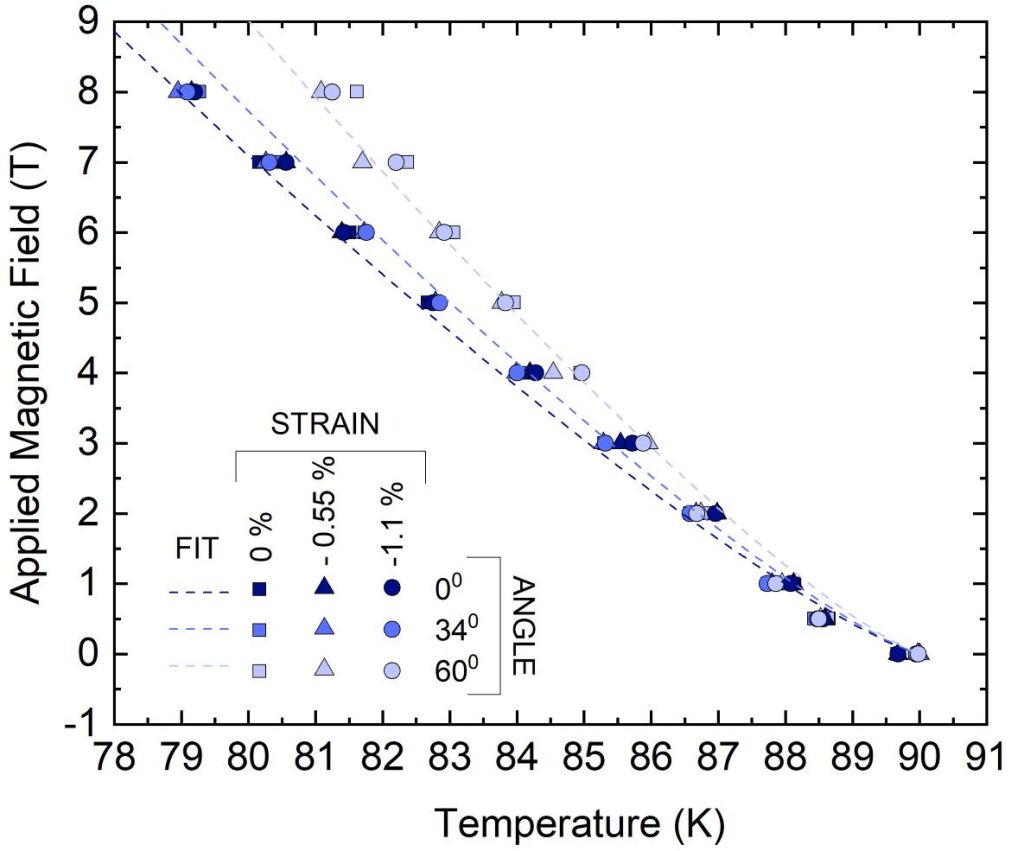

Figure 4.8: B_{c2} versus temperature for a sample at strains of 0 %, −0.55 % and −1.1 % and angles between the tape normal and B-field of 0°, 34°, and 60°. Global fits of the data to the Klemm equation shown as dashed lines.

$$B_{c2}(T,\theta,\varepsilon) = B_{c2}(0,\theta,\varepsilon)\left[1-\frac{T}{T_c(\varepsilon)}\right]^n \tag{4.3}$$

where θ is the angle between the applied field and the normal to the tape, n is the temperature index and T the temperature. A series expansion for the angular dependence of $B_{c2}(T,\theta,\varepsilon)$ is provided by Klemm [140], and to first order is given by equation 4.4 [139].

$$\left\{\frac{\eta^2}{8}\frac{\sin^4(\theta)}{\gamma^2 a^2(\theta)}\right\}[B_{c2}(T,\theta,\varepsilon)]^2 - a(\theta)B_{c2}(T,\theta,\varepsilon) + B_{c2}(T,0,\varepsilon) = 0 \tag{4.4}$$

where

$$a(\theta) = (\cos^2(\theta) + \gamma^{-2}\sin^2(\theta))^{\frac{1}{2}} \tag{4.5}$$

In equation 4.4 there are two free parameters, the anisotropy factor γ and η, where η is related to the interlayer spacing (s), the elementary charge (e) and Planck's constant $\hbar$ where $\eta = s\sqrt{e/\hbar}$.

In fitting equation 4.4 to the data, it was found that γ and η were strongly correlated. Therefore, the value of the interlayer spacing s was set to 12 Å to extract the γ values corresponding to the best fit, with 12 Å being the unit cell size for REBCO [141]. The fitting parameters obtained after fitting equation 4.4 to the $B_{c2}(T,\theta,\varepsilon)$ data are given in Table 4.1.

4.3.3 Discussion

From Fig. 4.6, it can be seen that the measured T_c appears to have almost no dependence on the strain, with a variation of less than 0.1 K.

This result can be explained from the microstructure of the REBCO CC tapes, whereby the REBCO lattice structure is not purely single crystalline,

Table 4.1: Coefficients from fits of Klemm's equation for $B_{c2}(T, \theta, \varepsilon)$ for the entire dataset (Global) and at each strain (ε), where in all cases η is held as a fixed parameter.

Parameter	**Global**	$\boldsymbol{\varepsilon = 0}$	$\boldsymbol{\varepsilon = -0.55\%}$	$\boldsymbol{\varepsilon = -1.1\%}$
T_c (K)	90.00	89.97	90.00	89.98
B_{c2}(0,0,0) (T)	103.38	105.81	100.7	103.7
n	1.219	1.231	1.207	1.218
γ	1.422	1.542	1.335	1.417
η - Fixed	0.047	0.047	0.047	0.047

but is composed of two different domains A and B that are separated by twin boundaries and whose unit cells are perpendicular to each other. The A domains have their a axis oriented parallel to the tape length whereas the B domains have the b axis oriented parallel to it [142]. It has been shown in previous work on detwinned REBCO tapes [115] that, on applying compressive strain, the T_c intrinsic to the A domains will decrease, and the T_c intrinsic to the B domains will increase, and vice versa for tension. The literature has shown T_c to decrease by about 2 K in the A domain, and increase by about 0.5 K in the B domain under a $-0.3\,\%$ strain [115].

Due to the small current of 0.1 A used in this work, and the large low-resistance shunt provided by the strain board, the current will choose a path through the REBCO domains corresponding the highest critical parameters. In this case, under the compressive strains applied, the current will preferentially flow through the B domains which have a slightly higher T_c compared to the A domains, therefore, we expect the measured T_c to only vary by a small amount, or even increase, depending on how much T_c changes in each domain under strain. This explanation is reflected in Fig. 4.6, where T_c does not appear to change much under strain, except for a slight increase of about 0.1 K under $-0.55\,\%$ strain.

In terms of the dependence of B_{c2} on strain, there also appears to be a

very weak dependence even after an application of $-1\,\%$ strain, which can explained using the same reasoning.

Previous work has however shown much larger effects of strain on B_{c2}. High current resistivity measurements on REBCO tapes (with [143] and without [117] APC) at $-1\,\%$ strain, found that the temperature at which B_{c2} is $8\,\mathrm{T}$ changes by about $3\,\mathrm{K}$ [115], in tapes aligned along the a-axis. High current measurements differ from low current measurements in the sense that the current is forced through all parts of the tape instead of choosing a percolative path of low resistance. Therefore, high current measurements characterise the material based on the broad range of critical parameter values found in a strained tape, and therefore lead to average (and hence lower) critical parameter values. A small current characterises the parts of the tape instead with the highest critical parameters [103].

In terms of the temperature and angular dependence of B_{c2}, the results are similar to those found in previous studies. The values of the parameters extracted from the fit to the Klemm equation shown in Table 4.1, such as the anisotropy constant (γ=1.4) and the temperature index (n=1.2), were found to be similar to those of previous ac susceptibility measurements [139].

4.4 Conclusion

This chapter outlines the preliminary work of measuring the B_{c2} dependence on temperature, angle and strain, as well as the T_c dependence on strain. A Cold Head was used to measured T_c from resistivity measurements with a small current of 100 mA under different compressive strains. A PPMS was then used to measure the dependence of B_{c2} on temperature, strain and angle also from small current resistivity measurements. It was found that although the temperature and angular dependence of B_{c2} agreed with previous work, and was modelled using the Klemm equations with fitting parameters similar

to those found from ac susceptibility measurements, there appeared to be almost no strain dependence. We attribute the independence of T_c and B_{c2} to strain to the twinned nature of the REBCO microstructure, and the small, percolative current used which characterised the parts of the REBCO with the highest critical parameters, regardless of the strain applied, instead of average parameters that are expected in high current measurements.

This preliminary work established the foundations of the main work that constitutes this thesis, namely, exploring the measurements that can be done on small REBCO samples using small currents. The next step involves small current J_c measurements on narrow tracks of REBCO, where the formation of narrow tracks is achieved using both chemical etching and focused ion beam milling.

Chapter 5

Preparation of REBCO Tracks from 4 mm to 5 µm

5.1 Introduction

The remainder of this thesis covers the experimental work done on REBCO tracks, with this chapter presenting the methods used to fabricate tracks a few microns wide, from a 4 mm wide tape for the $J_c(T, B, \theta, \varepsilon)$ measurements.

There is a great interest behind characterising REBCO using tracks rather than full-width tapes. The main reason is because narrow tracks have a much lower I_c than full-width tapes, and hence carry a smaller current and generate a smaller amount of ohmic heating. This can be beneficial for several reasons, firstly it allows for a better temperature control of the REBCO, especially in a variable temperature system such as a Cold Head where the heat generated must be removed through conduction through a sample platform [144]. Secondly, as I_c increases with decreasing temperature, the use of smaller currents enables transport measurements at lower temperatures down to 4.2 K, where the I_c of a full width tape would normally be too high

[106], [145]. This means that the tapes can be characterised at the operating temperatures of future Tokamaks such as SPARC (between 10 K - 30 K) [146]. The third benefit of using tracks is that the whole scale of the experiment, including sample size and current wiring, can be reduced. This small setup allows for measurements at higher fields beyond (the current world record) 35 T [147] , where the magnets are pulsed and the magnet bore size becomes very small (typically < 10 mm). The chapter begins by describing the techniques used to fabricate the narrow REBCO tracks. These include chemical etching, to create tracks down to 100 µm in width, followed by focused ion beam (FIB) milling on the chemically etched tracks to reduce the width further down to 5 µm. The scaling of I_c with track width will then be shown to demonstrate the success of the track fabrication. Finally, due to their fragility, an investigation into the sources of degradation of the tracks will be looked at to prove their robustness for testing.

5.2 Chemical Etching

The chemical etching process removes the copper, silver and REBCO from either side of a thin strip located near the centre of the tape approximately 100 µm wide. This produces a narrow track of REBCO covered with silver and copper on top of an exposed substrate. As the substrate is electrically insulating, the current is now forced to flow through the narrow central track which has a much smaller area than the full-width tape. As the J_c is the same at all points in the tape, and $I_c = J_c \times$ Area, the I_c of the track is hence reduced compared to a full-width tape. For example, at 77 K, the I_c of a full-width tape in self-field is around 130 A, but for a 100 µm track it is only 3 A. An example of a chemically etched track is shown in Fig. 5.1.

The procedure to make the tracks will now be described, with the steps involved shown in Fig. 5.2. We thank Awaji and Okada from Tohoku University for their instructions for the removal of copper, silver and REBCO

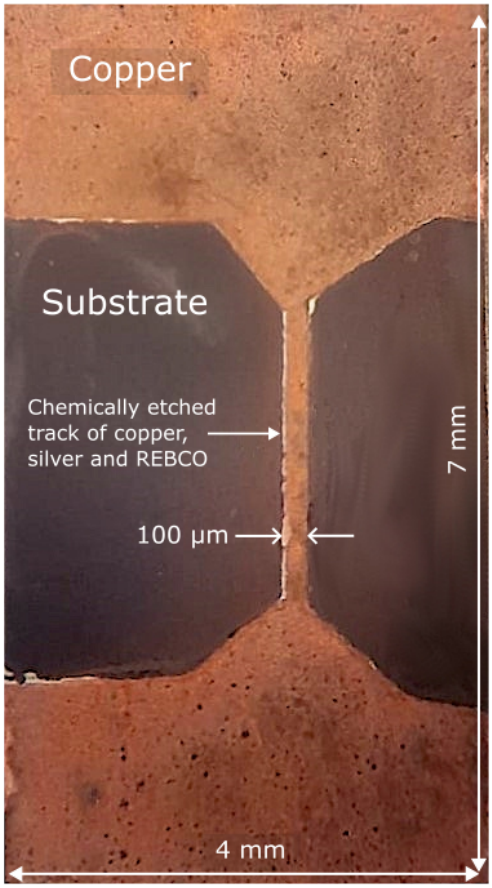

Figure 5.1: A chemically etched REBCO track.

from the REBCO CC by chemical etching [148]. In step 1, a Kapton mask is placed on the sample with its REBCO side up, and the sample is coated with a thin layer of varnish [145]. Once the varnish has dried, the mask is removed such that the copper under the mask is not coated with the varnish, and this part is etched away but the track and current contact areas are protected.

In step 2, the sample is placed in a beaker containing 25 % ammonium hydroxide (NH_4OH) solution [149] and 30 % hydrogen peroxide (H_2O_2) [150] with a volume ratio of 12:5. The solution etches away the copper and the

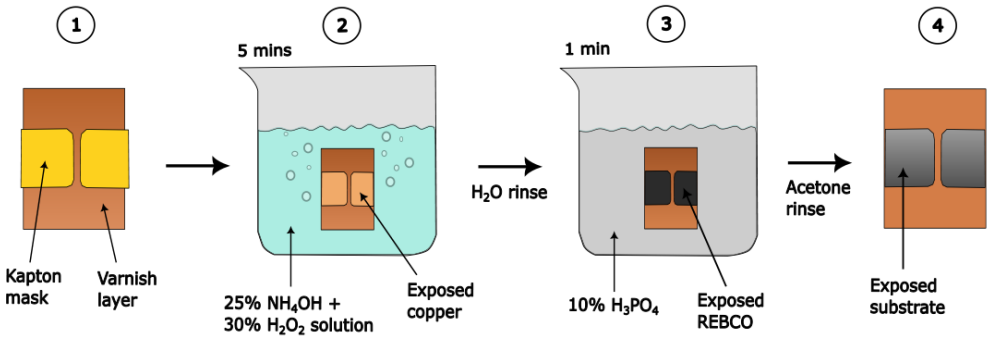

Figure 5.2: The chemical etching process of REBCO tracks. Sample held in $NH_4OH + H_2O_2$ solution for 5 minutes, and in H_3PO_4 for 1 minute.

silver layers, revealing the REBCO, and the sample is held in the solution until all of the unprotected copper and silver is removed, which takes around 5 minutes. The timing is important however, because if the sample is held in the solution for too long then etching starts to occur underneath the varnish, removing copper from the track. Many trials were done to determine this optimum etching time, any longer than 5 minutes and it was found that under-etching of the track under the varnish began to occur. The layer of copper and silver on top of the REBCO track was important to protect the REBCO from moisture and any damage.

After step 2, the sample is rinsed in water to remove the ammonia solution, and in step 3 the sample is placed in a beaker filled with 10 % phosphoric acid (H_3PO_4) [151] which removes the exposed REBCO and buffer layers, leaving behind a narrow track of REBCO, silver and copper on an exposed substrate, and this takes 1 minute. In the final step, the sample is rinsed in acetone to remove the protective varnish layer, leaving behind a track as shown in Fig. 5.1. Many samples of various widths were produced and tested to optimise this etching process of which around 70 % were successfully produced and the other 30 % were damaged or etched too much during the chemical etching process.

5.3 Focused Ion Beam Milling

For I_c measurements at very low temperatures down to 4.2 K, the I_c of a full-width tape can reach beyond 1000 A [152], and 25 A for a chemically etched track, which is still a high current. Hence we require even narrower tracks down to 5 µm in width to reduce the current sufficiently.

It is not possible to create tracks this narrow using chemical etching due to the non-uniformity in the rate of etching, leading to variations in track widths of up to 10 µm. Therefore, the technique of FIB was used to mill out straight-edged tracks within a chemically prepared track that were 5 µm wide. The FEI Helios NanoLab 400 DualBeam was used to do this [153]. This is a system that integrates an ion beam and an electron beam for simultaneous FIB operations and SEM imaging.

5.3.1 The FIB Procedure

To make the tracks, gallium ions were used to mill out wells that were deep enough to cut through the copper, silver and REBCO layers and hence could electrically separate off areas of the REBCO.

As the FIB is an expensive process, we aimed to minimise the area that required milling, which led to the concept shown in Fig. 5.3. The FIB cut two U-shaped wells into either side of the chemically etched track, represented by the black outline in Fig. 5.3. This electrically separated off parts of the track and forced current to flow between the 5 µm-separated wells.

The pattern for milling read by the Helios NanoLab was firstly drawn using the software Clewin [154]. It was exported as a .gds file and then opened in the software GDSTODB [155] to input the FIB settings. It was then saved as an ASCII stream file to be imported into the Helios NanoLab. The pattern design and milling settings are shown in Fig. 5.4. These files are listed in Appendix I.

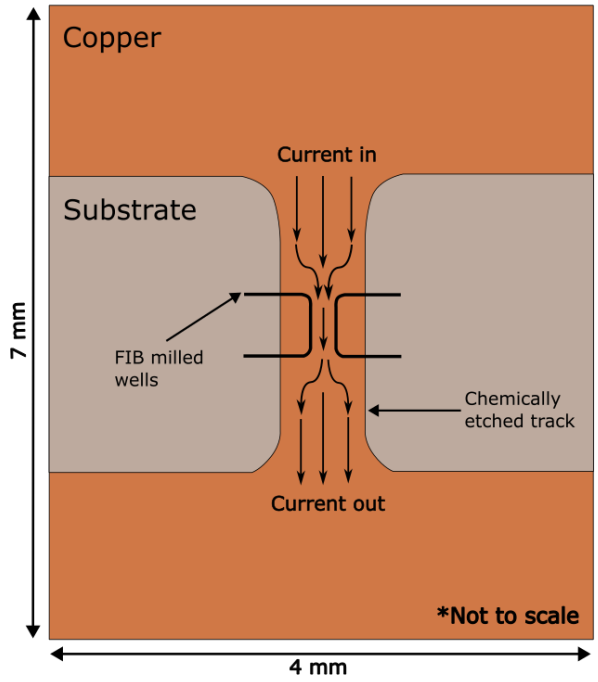

Figure 5.3: The current path through the chemically etched and the FIB milled track. The thick, black U-shaped lines represent the area milled.

The total milling time depended on the gallium ion beam current used and the dwell time. We chose a high ion current of 9.3 nA and a dwell time, which represents the milling time of each pixel, of 100 µs. This resulted in an overall milling time of around 5 hours.

To operate the FIB, the sample was installed into the chamber, which was then pumped down to form a vacuum. After focusing the ion and electron beams, the sample was tilted to 52° such that the sample surface was perpendicular to the ion beam, as shown in Fig. 5.5.

The electron and ion screen magnifications were coupled and the correct magnification for the pattern size was set. Then the region for milling was found on the ion beam screen and the pattern was imported, the gallium

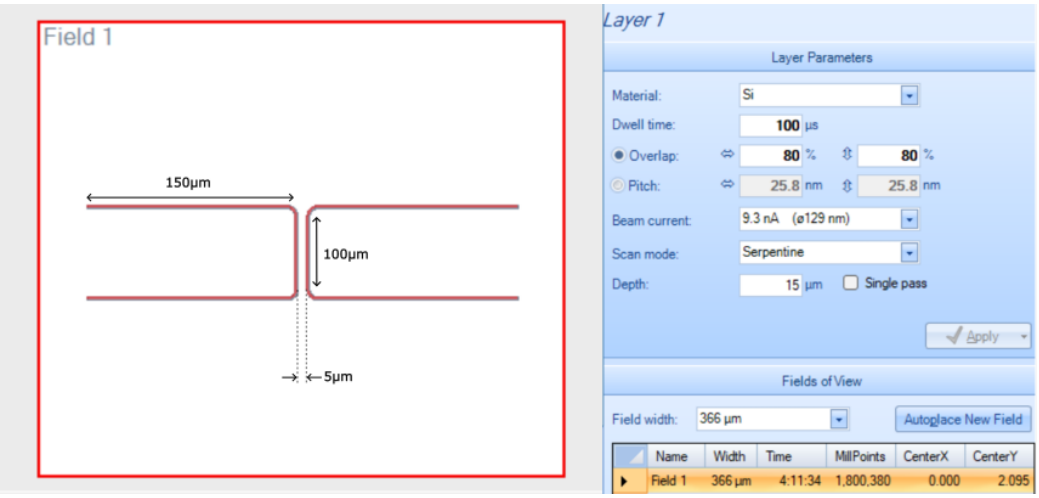

Figure 5.4: The pattern to be FIB milled, and the appropriate milling settings using GDSTODB software.

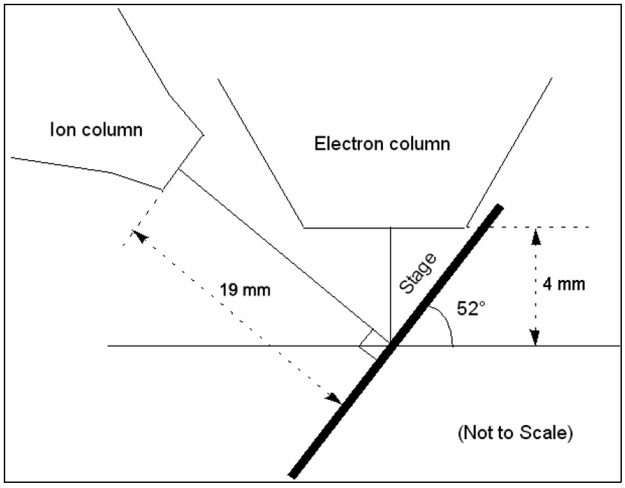

Figure 5.5: Positioning of the sample and the ion and electron beams for milling in the FIB.

ion current set to 9.3 nA, and the milling was started. During milling, the progress could be seen live on the electron beam screen using the SEM.

Some difficulties occurred in the making of the FIB tracks. The first problem

occurred where the FIB failed to mill deep enough to cut through the REBCO layer, which was underneath about 10 µm of copper and silver. This was because of re-deposition due to the high depth-to-width ratio of the wells, meaning that the milled material could not properly be removed from the well. This problem was overcome simply by making the wells wider, at least 2 µm, and by using a Serpentine scan mode.

Another problem occurred because of the first pattern design, which had 90° corners instead of rounded ones. These sharp corners caused cracks to form across the track, especially when strain was applied, and this was prevented simply by rounding off the corners of the pattern.

An SEM image of the final FIB cut is shown in Fig. 5.6, and two tracks with a higher magnification are shown in Fig. 5.7.

5.4 Scaling of I_c

One of the first checks after the etching was to test whether the I_c scaled linearly with the REBCO track width. To check this, many samples were fabricated with various different widths using chemical etching and FIB milling and their I_c values measured. These measured I_c values were plotted against the track width of each sample to see whether there was a directly proportional, linear relationship between the I_c values and track widths as expected.

To measure I_c, current and voltage joints were soldered to either end of the REBCO tracks to measure the current through and voltage across the tracks. Each REBCO tape was mounted to a G10 probe (see section 6) using thermal grease and Kapton tape. The current was slowly increased and the voltage measured.

The electric field was found by dividing the voltage by the gauge length, i.e. the length of the tracks (≈3 mm for the chemically etched tracks and

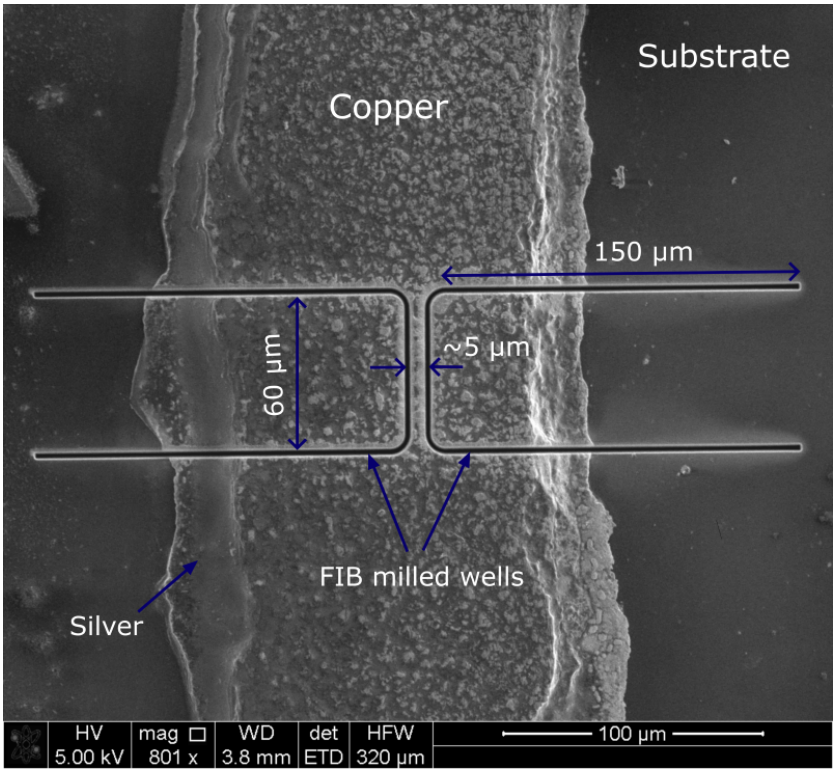

Figure 5.6: SEM of a FIB track on top of a chemically etched track.

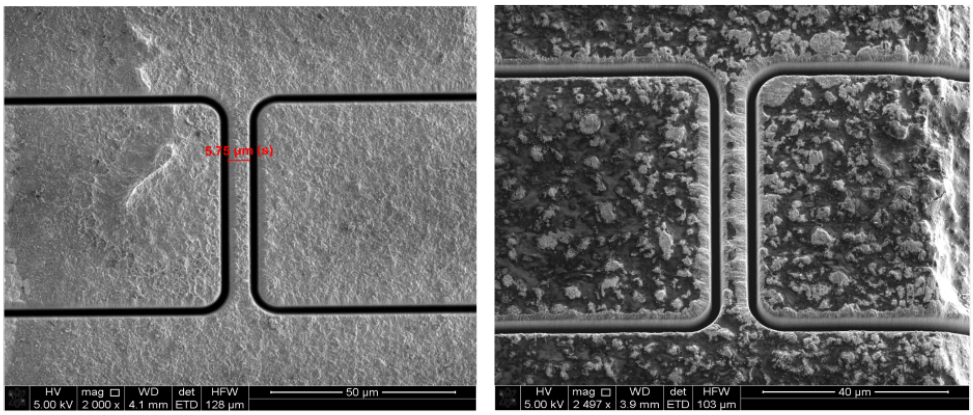

Figure 5.7: SEM of two FIB tracks, higher magnification.

≈100 µm for the FIB tracks). As the FIB gauge lengths were much smaller than the chemically etched ones, the electric fields they produced were much larger, so we chose quite a large electric field criterion of 1000 µVm^{-1} to compare all samples.

We measured I_c for each sample in liquid nitrogen (≈77 K) at self field, but later on samples were also measured at 0.5 T as the self field for each track width may be slightly different. The track width was measured on a magnified image of the sample, such as those in Fig. 5.1 and Fig. 5.6. The non-uniformity of the track width from the etching process led to a measurement error of 5 %.

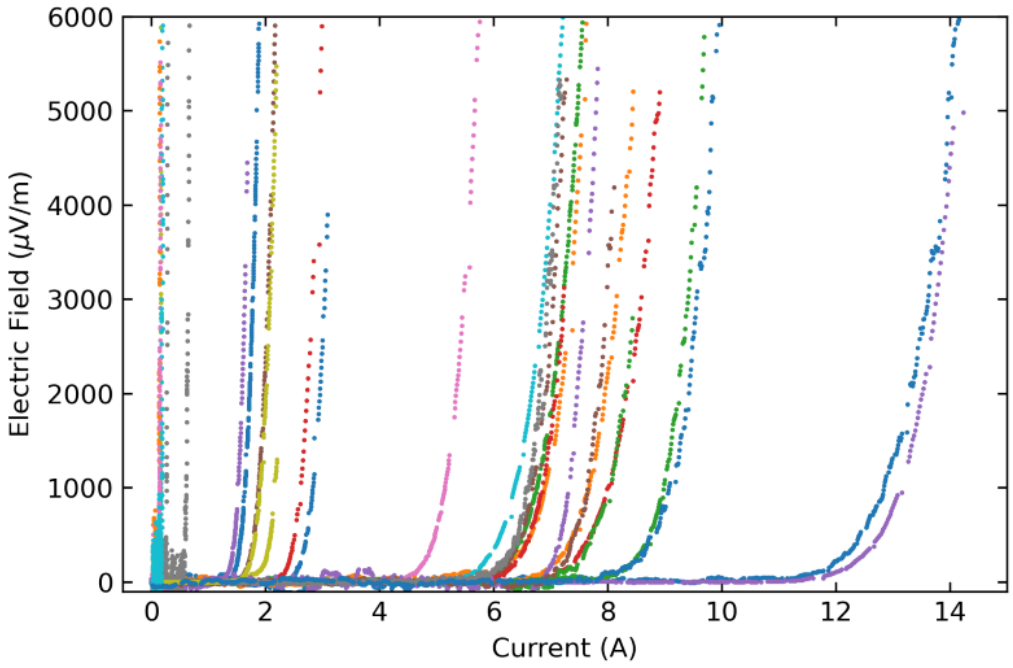

Figure 5.8: VI traces for all chemically etched and FIB samples at 77 K and in self field.

In total, 31 samples were measured in self field and the V-I traces for these samples are shown in Fig. 5.8. The widths of the tracks ranged between 5 µm

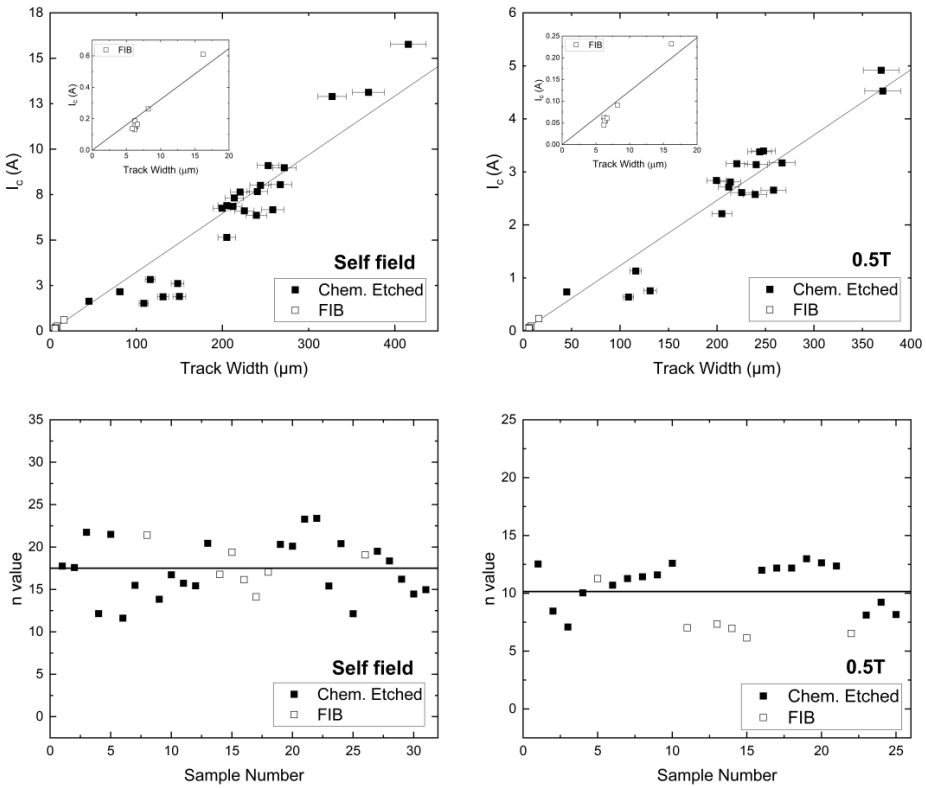

Figure 5.9: I_c versus width of chemically etched and FIB samples measured at 77 K in self field (top left) and 0.5 T (top right). Corresponding n values are shown in self field (bottom left) and 0.5 T (bottom right). Open symbol data points are FIB samples.

and 400 µm; any larger widths than this carried currents which generated too much ohmic heating. Fig. 5.9 presents the I_c versus width of all samples along with a linear fit to the data which passes through the origin and 129 A and 49 A at self field and 0.5 T respectively at 4 mm width. There is a linear fit as expected, hence confirming that the I_c scales correctly with track width. Furthermore, the fit passes through the correct values of I_c that have been measured for a full-width tape at self field and 0.5 T [156].

Fig. 5.9 also shows the transition index (n value) measured for each sample by a linear fitting of the power law between $1000\,\mu Vm^{-1}$ and $10\,000\,\mu Vm^{-1}$. This large electric field criterion was used to ensure that the data used in the linear fit was above the baseline noise of all samples. The n value measured is independent of the track width, with a mean of 17.4 in self field, and 10.1 at 0.5 T. Previous measurements on full-width tapes measured an n value of 14 at 0.5 T [156]. The FIB samples, shown as open symbols, have n values similar to the chemically etched samples, which implies that the REBCO is not being damaged by the FIB milling, where we would expect a damaged sample to have a lower n value [157].

5.5 Degradation Mechanisms

Due to the small width and the exposed edges of the REBCO tracks, there was a concern that the tracks would be easily damaged.

There are several ways that REBCO can be damaged, these include applying mechanical loads, thermal cycling, exposure to heat and exposure to water. Therefore an investigation was done to test the robustness of the samples to various degradation mechanisms.

A damaged or degraded REBCO sample is characterised by a permanent drop in I_c and the n value. Each degradation mechanism will in turn be investigated.

5.5.1 Mechanical Degradation

Mechanical degradation involves any sort of stress applied to the REBCO. Applying stress can cause effects such as delamination and crack generation, both of which damage the REBCO layer [158]. It has been found in previous work [159], that applying tensile strains greater than 0.3 % causes an irreversible drop in I_c. Also, repeated strain cycles have been found to weaken

the bonding between layers leading to delamination.

5.5.2 Degradation due to Heat

Applying too much heat to REBCO can cause oxygen out-diffusion from the REBCO layer, causing an oxygen deficiency in the REBCO layer resulting in partial loss of superconductivity [160].

The REBCO experiences heating during the soldering of the current and voltage joints, as well as soldering it to the strain board. Further heating is required to adhere the strain gauge to the sample. For the specific strain gauge used, the curing settings required are 120 min at 170 °C [161]. These settings however have been found to degrade the I_c of our specific tracks. Therefore, a curing time of 180 min at 150 °C was chosen instead.

5.5.3 Degradation due to Thermal Cycling

Thermal cycling of the samples can cause delamination of the REBCO tapes because of the differential thermal contraction that occurs between the layers [162]. The delamination has been found to occur mainly at the Ag/REBCO interface.

A test was done on a REBCO track to see whether the I_c degraded after thermal cycling. The sample was placed in liquid nitrogen, a VI trace was taken, and then the sample was immediately warmed up to room temperature using a heat gun to prevent condensation. Fig. 5.10 shows the VI traces for 10 thermal cycles, and suggests that there is no significant drop in I_c over this number of cycles. This is important to know for the experiments presented in this thesis, where the samples on average experienced a few thermal cycles during their testing and measurement processes. However, in large scale applications of REBCO in the magnets of Tokamaks there will be hundreds to thousands of thermal cycles during the lifetime of the reactor,

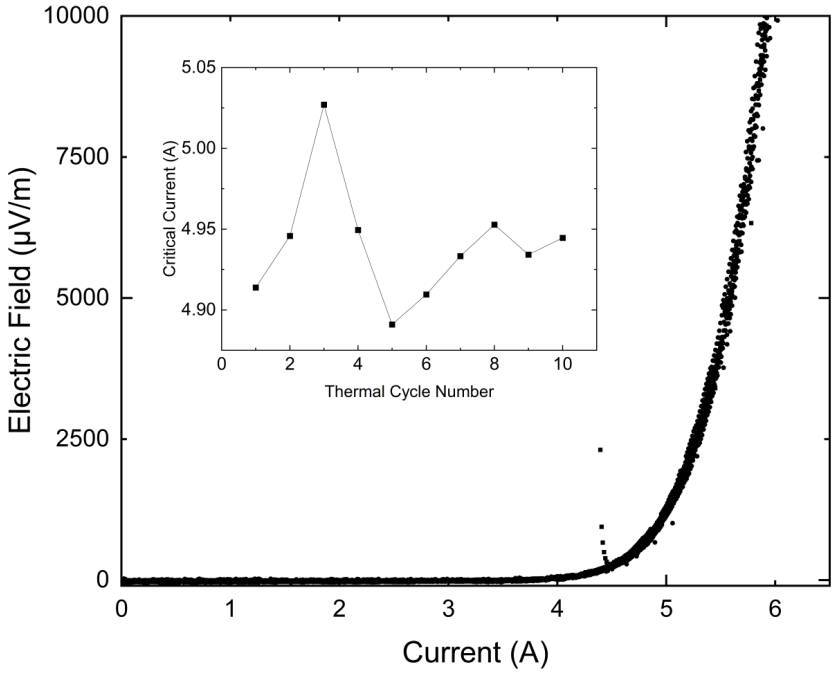

Figure 5.10: VI traces of a REBCO track at 0.5 T and in liquid nitrogen for 10 thermal cycles. Inset: Corresponding I_c values for each cycle.

and therefore this investigation was not applicable to large scale applications of REBCO CC.

5.5.4 Degradation due to Water Exposure

It is known that $YBa_2Cu_3O_7$ reacts with water to produce Y_2BaCuO_5 according to the reaction:

$2YBa_2Cu_3O_7 + 3H_2O \rightarrow 5CuO + 3Ba(OH)_2 + Y_2BaCuO_5 + 1/2O_2$.

The Y_2BaCuO_5 is a semiconducting green phase which is non-superconducting, and in this way, water can degrade REBCO [163].

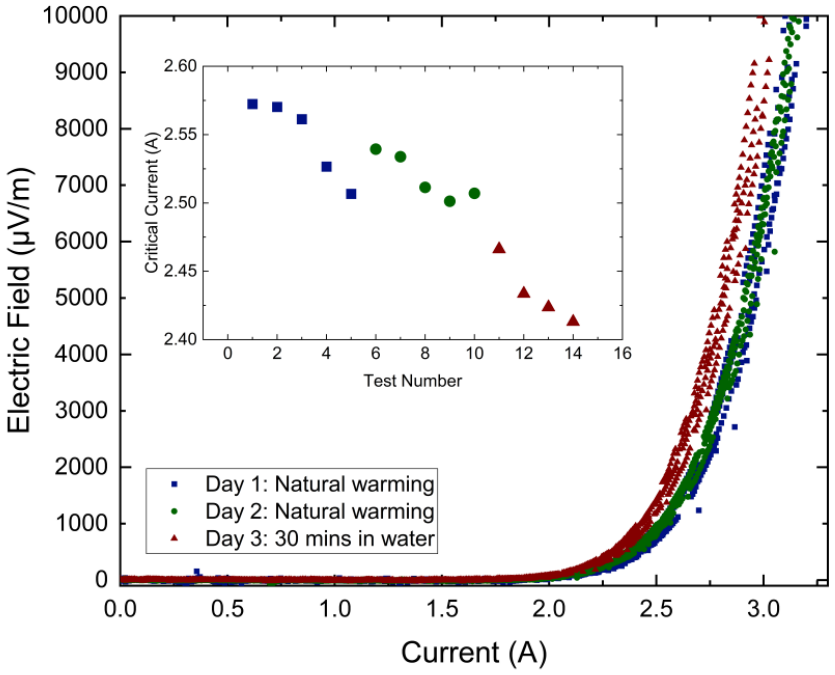

Figure 5.11: VI traces of a REBCO track at 0.5 T in liquid nitrogen for 5 thermal cycles with natural heating (blue squares), another 5 cycles a day later (green circles), and 4 cycles between which the sample is held in water for 30 minutes (red triangles). Insert: Corresponding I_c values for each measurement.

To investigate the effects of water on REBCO, three tests were done. During the first test the I_c in liquid nitrogen was measured 5 times, and between measurements the sample was allowed to warm up naturally without the heat gun causing the track to frost over and become wet. The first test is represented by the blue data in Fig. 5.11. The second test was a repeat of the first test but done the next day such that the sample had been left overnight, and this data is represented by the green data in Fig. 5.11. During the third test the I_c was measured 4 times but between measurements the sample was

warmed naturally and held in water for 30 minutes, and this is represented by the red data.

It can be seen from Fig. 5.11 that the presence of water causes the I_c to drop consistently, which is most likely due to the exposed edges of the tracks being in direct contact with the water. Therefore, these results have highlighted the importance of protecting the tracks from moisture, and to do this we warmed the samples using a heat gun immediately after testing to prevent the formation of frost, and we covered the tracks with a thin layer of GE varnish to protect the exposed edges from moisture in the atmosphere.

5.6 Conclusion

In this chapter, the methods of preparing the narrow tracks of REBCO, namely chemical etching and FIB milling, have been presented. After having outlined the fabrication process, we presented results of the I_c measurements for different track widths to prove that the I_c scaled linearly with width, and also passed through the origin and the correct value for a full-width tape (of around 130 A in self field). After confirming the success of the track fabrication, the various degradation mechanisms of the REBCO were explored, including the effects of mechanical stress, heat, thermal cycling and water exposure. Tests were done to show that the tracks were resilient to thermal cycling, but had their I_c values lowered when exposed to water.

The REBCO tracks described in this chapter will be the samples from which data is collected and presented in the following chapters of this thesis, where now in the following chapter we present the $J_c(\varepsilon)$ measurements on the chemically etched and FIB samples in liquid nitrogen.

Chapter 6

The Dependence of the Critical Current Density of REBCO Tracks on Strain at 77 K

6.1 Introduction

In this chapter the measurements of the J_c dependence on ε for chemically etched and FIB milled narrow tracks of REBCO CC are presented.

The layout of this chapter is as follows. Firstly we present a small overview of previous work that has measured the $J_c(\varepsilon)$ of REBCO tracks. Our experimental setup and method is then outlined, followed by the results of the $J_c(\varepsilon)$ curve for the chemically etched and FIB tracks and how they compare to the full-width tape data. After presenting the results, we provide an explanation for the $J_c(\varepsilon)$ data found for the FIB tracks by fitting the data to the chain model and imaging the tracks using electron backscatter diffraction (EBSD) to investigate the domain landscape.

6.2 Previous Work of $J_c(\varepsilon)$ on Tracks

The use of REBCO tracks made from full-width REBCO tape using laser or chemical etching has been used in many other studies to characterise the J_c dependence on field and temperature [106], [145], [164]. Some work has also been done to characterise the REBCO CC using FIB milled tracks [164]. There is however less work that uses tracks to determine the response of J_c to an applied strain [118], [165]

The work presented in [165] demonstrates the use of laser etched and FIB milled tracks to measure the strain dependence of J_c for YBCO tape. This is adjacent to the work and results presented in this chapter, which uses chemically etched and FIB tracks of REBCO CC. The conclusions drawn from the work of [165] is that all tracks produced a dependence of J_c on ε that can be expressed by the same power-law function: $J_c(\varepsilon) = J_c(\varepsilon_m)(1 - a|\varepsilon - \varepsilon_m|^{2.18\pm0.02})$ where ε_m is the strain at which the curve maxima occurs, and the strain sensitivities of J_c of each track, given by a, extracted from the fits were found to be higher for the FIB tracks compared to the laser etched ones (a =10 500 $\%^{-1}$ compared to a <7000 $\%^{-1}$). As this study was focused towards investigating the effects of grain boundaries on strain, not much treatment was done to compare the individual strain curves for each track, presenting the strain curves as raw data sets with thermal offsets in the curve peaks and finding a variation in the strain sensitivities a of between 5600 $\%^{-1}$ and 6900 $\%^{-1}$ for the laser tracks. In addition, the FIB tracks milled for this study were confined to cross only one grain boundary, which is not a representation of the full microstructure of the tape.

As the work we undertook was motivated by checking for consistency in the track data, we took a more rigorous approach that involved carefully centering the strain curves and comparing them with intricate chain models, and also designing FIB tracks which were long enough to span over several grains and therefore contain the same landscape of the microstructure as the

tapes.

The process of FIB milling involves firing a beam of low energy ions, usually gallium ions, onto the surface of REBCO, and this process is somewhat analogous to irradiating REBCO with high energy ions to simulate the neutron flux that a REBCO magnet would experience in a Tokamak. Many studies have been done to investigate the effect of ion irradiation on the microstructure [166], [167], finding the irradiation to cause a displacement of oxygen atoms in the unit cell, or in more severe cases a detwinning of the REBCO due to a tetragonal transition caused by an oxygen deficiency after irradiating with 1 MeV helium ions [166]. Detwinning of REBCO has also been found to occur by applying strain at high temperatures to the REBCO [114]. FIB milling using 30 kV gallium ions ($\approx$ 1 MeV) as used in this work could potentially cause a similar displacement of the oxygen atoms in the REBCO microstructure, as well as a production of heat both of which could lead to a disappearance of the twin boundaries and a change in the superconducting performance of REBCO.

Bearing this information on the potential effects of FIB milling in mind, we now proceed to present our work done to measure $J_c(\varepsilon)$ on the chemically etched and FIB tracks, beginning with an overview of our experimental method.

6.3 Experimental Method

Our experimental setup allowed for variable magnetic field up to 0.7 T, variable angle between the field and the tape c axis, and variable strain measurements on a REBCO track in liquid nitrogen. We present our experimental procedure, starting with the sample preparation, assembly of the sample to the measuring probe, and finally collecting the VI traces and changing the field, angle and strain.

6.3.1 Sample Preparation

The samples used were the 5 µm to 400 µm wide tracks. The sample setup process involved soldering it to the strain board and attaching a strain gauge. This last step was the most challenging as the heat involved sometimes degraded the REBCO.

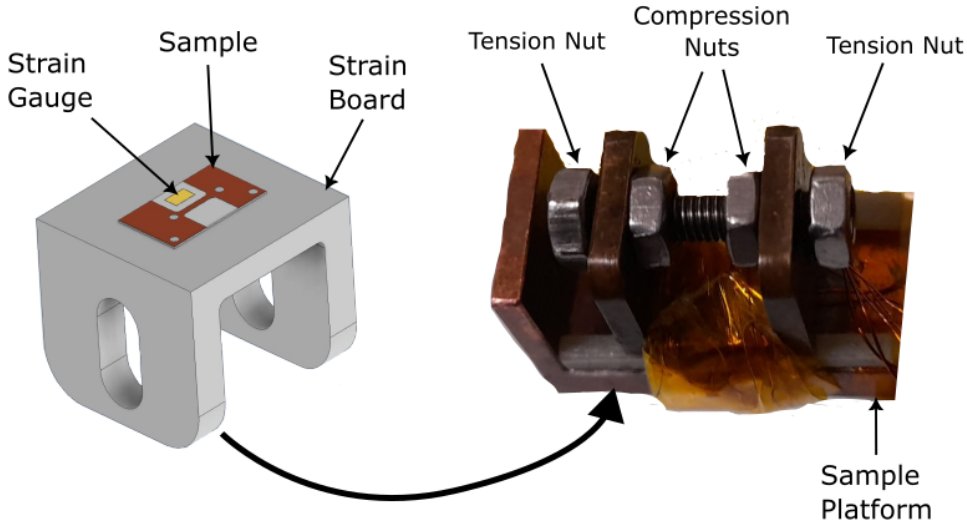

Figure 6.1: Positioning of the REBCO tape on the strain board, and of the strain board on the 77 K sample platform.

Firstly, the voltage and current joints were soldered to the tape surface, and a preliminary I_c measurement was done to check the etching process had been successful. The positioning of the current joints on the top side of the REBCO sample was chosen to minimise the amount of current shunting.

Afterwards, the sample was soldered substrate side down to the strain board using 60-40 PbSn solder on a hot-plate at 200 °C. This process was done in less than 10 seconds to prevent degradation caused by excess heating. The sample was soldered to the outside of the strain board (see Fig. 6.1) as opposed to the inside of the board as done in Chapter 4. This was because,

when the sample was on the inside the nuts and bolt mechanism caused some damage to the sample, whereas placing it on the outside avoided this problem altogether.

The next step was to attach a strain gauge (SG) to the sample. The SG was placed on the exposed substrate directly next to the track. Previously in Chapter 4, the SG was placed on the strain board next to the sample, however placing it now on the sample allows for a more direct measurement of the strain state of the REBCO. The surface was cleaned with acetone and the SG was glued and heat treated for 3 hours at 150 °C. This heat treatment was found to not degrade the sample.

After the SG glue had set, the sample and SG current and voltage wires were soldered on. The strain board was then placed on the end of the sample platform as shown in Fig. 6.1, with two G10 spacers that distanced the sample from the sample platform and cigarette paper used again for electrical insulation of the sample from the sample platform. The strain board was secured to the sample platform using kapton tape, and the strain-applying nuts and bolt were screwed on.

6.3.2 The Measurement Probe

With the sample in place, the sample platform was then bolted to a G10 measurement probe that was designed and commissioned in Durham (see Fig. 6.2), drawings of the probe are given in the Appendix. Electrical connectors were placed on the probe to connect the sample wiring to the external wiring. The probe was designed to enable variable field and variable angle between the magnetic field and tape c axis (magnetic field angle) measurements of the sample in liquid nitrogen. The length of the T-shaped probe allowed the sample to be suspended within a narrow dewar filled with liquid nitrogen such that the sample was positioned at the centre between the poles of the iron-core horizontal magnet as shown in Fig. 6.3. The arms of the probe

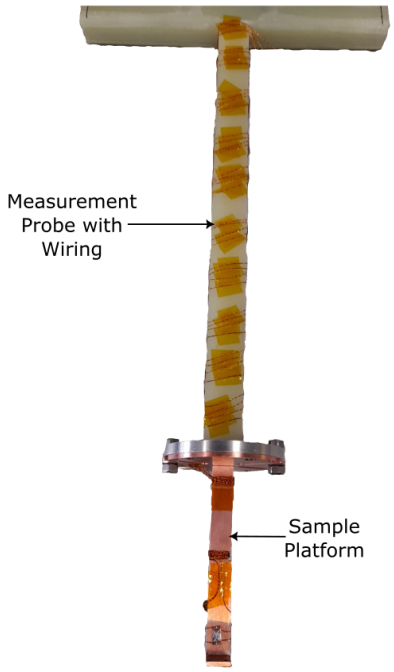

Figure 6.2: G10 measurement probe and sample platform.

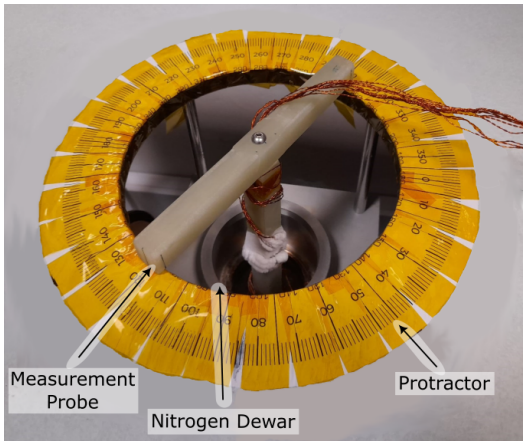

Figure 6.3: The measurement probe setup on the table-top protractor for variable magnetic field angle measurements.

rested on a table with a protractor attached, and small marks on the probe arms were aligned with the protractor markings to vary the angle.

6.3.3 Measuring the VI Traces

The entire experimental setup is shown in Fig. 6.4. In this setup, there was an additional open nitrogen dewar in which the strain could be changed with the sample submerged in liquid nitrogen. This was an improvement from the setup in Chapter 4 where the strain was changed at room temperature. Changing the strain within liquid nitrogen prevented the need to consider differential thermal contractions and the temperature-dependent change in

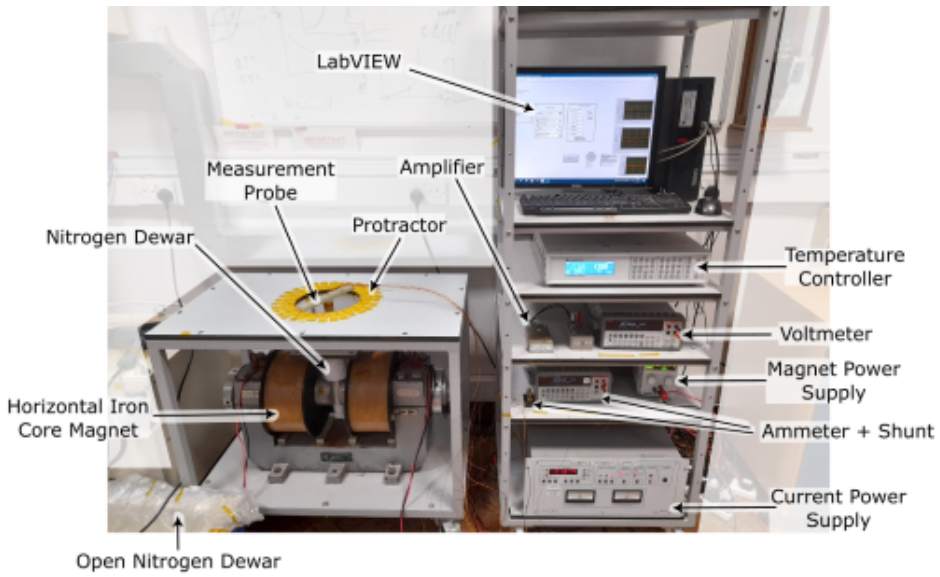

Figure 6.4: The experimental setup for $J_c(\varepsilon)$ measurements in liquid nitrogen.

resistance of the SG grid, also eliminating thermal cycling in general. The strain was determined according to equation 4.1, with R_0 being the resistance of the SG under zero-applied strain and R the resistance with strain applied all measured in liquid nitrogen. To apply compression, the outside nuts were loosened and the inside ones tightened against the strain board using a pair of long-handled spanners. Alternatively, to apply tension, the inside nuts were loosened and the outside ones tightened.

Once the strain was set in the open dewar, the probe was quickly transferred to the nitrogen dewar. It took only 5 seconds to do this, such that the warming of the sample was negligible. The angle of the sample was set manually by aligning the arms of the probe with the protractor. A code was written on LabVIEW to set the magnetic field across the sample through control of the current in the magnet power supply, relying on a calibration to convert magnetic fields to currents. The field was always set to a slightly higher value than required by 0.05 T, and then lowered to the correct value to

clear the flux pinning landscape. The current was ramped through the sample at a rate chosen by the user while the sample voltage was simultaneously measured using a Keithley multimeter connected to a 50,000 gain amplifier. The sample current was measured using a Keithley multimeter connected across a 10 mΩ shunt that was wired in series with the current power supply. The speed of data acquisition was around one reading per millisecond.

The choice of the current ramp rate was important. If it was too slow then the trace time was too long and there was likely to be heating. But if it was too fast then not enough data was collected on the VI trace. It was found that the I_c measured did not depend on the ramp rate. The ramp rate was determined by dividing an estimated I_c value by the trace time, which was taken to be 24 seconds, in this way, the ramp rate was roughly constant for all VI traces.

Once the VI trace had finished, the next magnetic field was set automatically. Once the VI traces were collected at all fields, the probe was placed back into the open dewar to change the strain, and the process repeated at this new strain.

6.3.4 Analysing the VI Traces

The raw voltage-current traces were converted to electric field-current traces by dividing by the gauge length, which was generally 3 mm for chemically etched samples, and 100 µm for the FIB samples.

Due to the limited space on the sample, the separation between the current contacts and voltage contacts was only around 2 mm. The current-transfer length was generally smaller than this separation, but for some samples that had delaminated slightly at the current joints, the current-transfer region was lengthened causing there to be a resistive baseline. We tried to prevent delamination by using thinner fly wires to connect the sample to the external

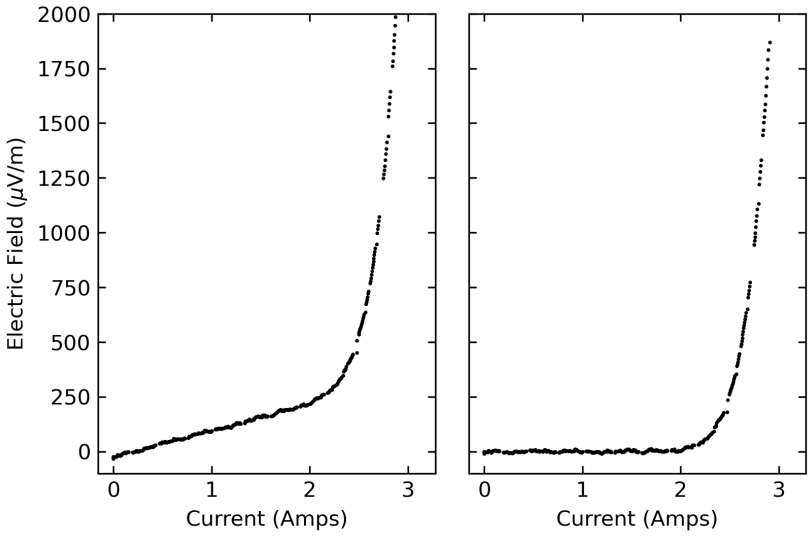

Figure 6.5: Example of a raw VI trace (left), and a baseline corrected trace (right).

circuitry to reduce stress on the copper layers, and this had a very positive effect on preventing delamination. The thinner wires were however easier to burn through and currents were limited to below 10 A to avoid this.

To correct for the resistive baseline, a linear fit was made through the baseline data and subtracted from all data in the VI trace following the well-known approach [125]. An example of a raw VI trace and a baseline-corrected trace is shown in Fig. 6.5.

Choosing the Electric Field Criterion

The I_c was found by interpolating the corrected data points and determining the current at which the $E = E_c$. The chosen criteria were $1000\,\mu\mathrm{Vm}^{-1}$ for the chemically etched samples and $5000\,\mu\mathrm{Vm}^{-1}$ for the FIB samples.

The E_c for the chemically etched and FIB tracks were different because of their different gauge lengths (100 µm for the FIB compared to 3000 µm for

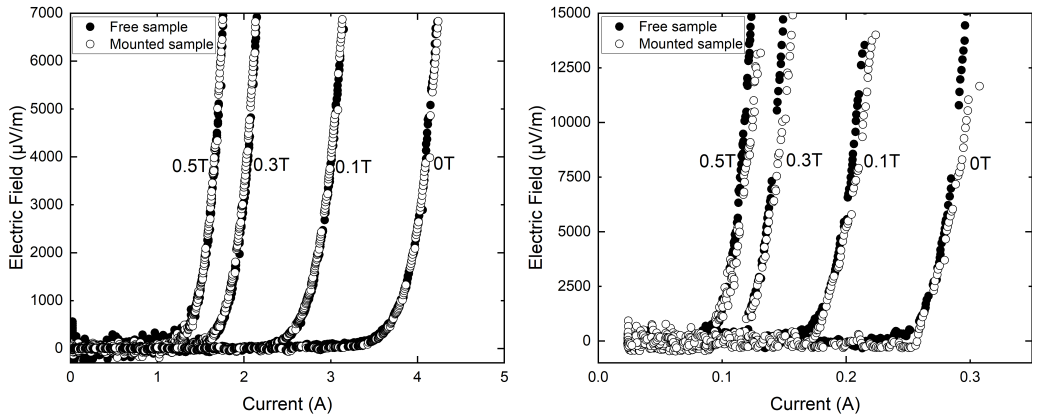

Figure 6.6: VI traces for a chemically etched sample (left) and FIB sample (right) before and after soldering it to the strain board at 77 K.

the chemically etched tracks). The electric fields were therefore amplified due to the small gauge length of the FIB tracks, including the baseline noise. It was found that the minimum E_c values that were clear from the baseline noise for every VI trace from each sample were $1000\,\mu\mathrm{Vm}^{-1}$ and $5000\,\mu\mathrm{Vm}^{-1}$ for the chemically etched and FIB tracks respectively. Fig. 6.6 shows the VI traces of an I_c test for a FIB and chemically etched sample before and after the sample was soldered to the strain board, where it is clear that the electric fields of the FIB sample are much larger than the chemically etched one. However to compare between FIB and chemically etched data an E_c of $5000\,\mu\mathrm{Vm}^{-1}$ was used.

The n values were found from the gradient of a linear fit to the E-I data in log-log space, and were chosen to be evaluated between $1000\,\mu\mathrm{Vm}^{-1}$ and $5000\,\mu\mathrm{Vm}^{-1}$ for the chemically etched, and $2000\,\mu\mathrm{Vm}^{-1}$ and $10\,000\,\mu\mathrm{Vm}^{-1}$ for the FIB.

It was expected that after soldering the REBCO tape to the strain board, there would be some current shunting through the strain board causing the I_c to look artificially high. But it was found that there was a negligible amount

of current shunting below the chosen E_c values, as shown in Fig. 6.6. This was due to the location of the current injection points, which were directly soldered to the top of the REBCO tape, causing the resistance of the path through the superconductor to be significantly less than the path through the strain board. This led us to assume there was a negligible amount of current shunting, and hence all I_c values were taken as true values for the REBCO tracks.

After having explained the data acquisition and analysis process, we now present the results of $J_c(\varepsilon)$.

6.4 The $J_c(\varepsilon)$ Strain Dependency

In this section we present the results of the $J_c(\varepsilon)$ curve for the chemically etched and FIB REBCO tracks. This standard $J_c(\varepsilon)$ curve represents the case where both the uniaxial strain and the current are oriented along the length of the tape, referred to in section 7.3 as the $I_x\varepsilon_x$ setup. This is the standard current and strain direction used for all strain work on REBCO in the literature, so we use this to compare our data to other strain work done on 4 mm wide REBCO tapes.

The motivation of the work presented here was to investigate whether the tracks behaved the same way under strain as a full-width tape. This involved comparing the chemically etched and FIB $J_c(\varepsilon)$ data to a full-width tape. Table 6.1 lists all two chemically etched and four FIB samples on which the $J_c(\varepsilon)$ curve was measured.

To obtain a strain curve, the cycle of measurements was as follows. Firstly a 0 % strain I_c measurement was taken with loosened nuts on the strain board. Afterwards, I_c measurements were made under compressive strain down to -1 % in 0.1 % increments by tightening the inside nuts. Then the strain was released back to 0 % strain with I_c measurements taken again every 0.1 % to

Table 6.1: The samples used to measure $J_c(\varepsilon)$.

Sample	**Track Width** /μm	**Track** I_c /A (Self Field)
Chem. etch. (1)	212.1	6.86
Chem. etch. (2)	218.4	6.61
FIB (1)	8	0.26
FIB (2)	5.7	0.15
FIB (3)	17.8	0.61
FIB (4)	5.9	0.16

check for reversibility. Finally, measurements in tension up to 0.3 % and then back to 0 % were taken in 0.1 % increments. It was found that the strain of the strain board with the nuts loose was slightly different to that after the compressive cycle (by at most 0.005 %). This was attributed to some plastic deformation of the strain board. The strain curves were measured at four different magnetic fields: 0.7 T, 0.5 T, 0.3 T, 0.1 T and at 0° angle.

The I_c values were converted into J_c values according to the formula $J_c = I_c/A$. The area A of the track was the track width multiplied by the REBCO layer thickness, taken as 1.6 µm [81].

6.4.1 $J_c(\varepsilon)$ of Chemically Etched Tracks

Firstly we present the results from a chemically etched track.

The J_c versus ε curves were found to have an inverse parabolic shape and a $J_{c,peak}$ that was at non-zero strain. This non-zero strain peak offset was most likely caused by a differential thermal contraction between the tape and the strain board on cooling, leading to an inherent thermal pre-strain. To characterise this, a parabola was fitted to the strain curve for data above $0.95J_{c,peak}$. The maxima in the parabola was found and the curve shifted by

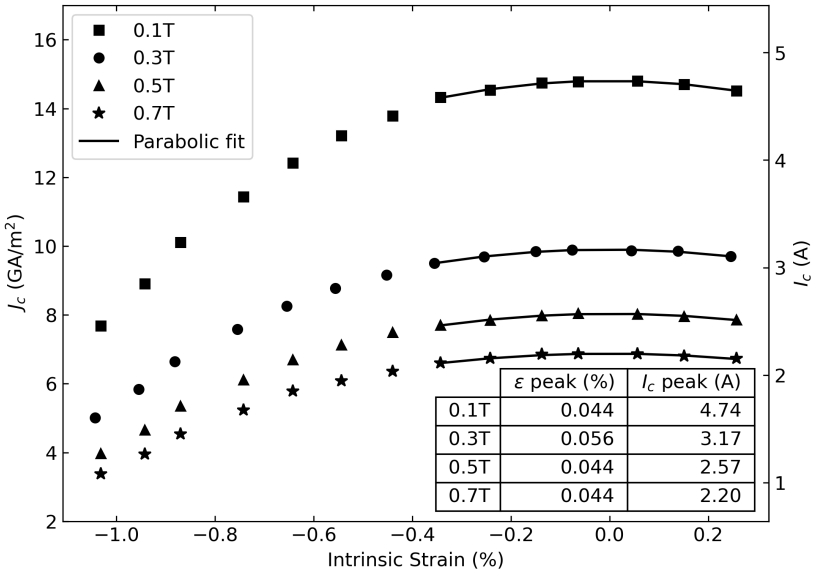

Figure 6.7: $J_c(\varepsilon)$ data with parabolic fit between 0.95 $J_{c,peak}$ and $J_{c,peak}$ for chem. etch. (1). The position of the maxima of the strain curves at each field were derived using a parabolic fit above 0.95 $J_{c,\,peak}$ (shown in bold) and are given in the inset table.

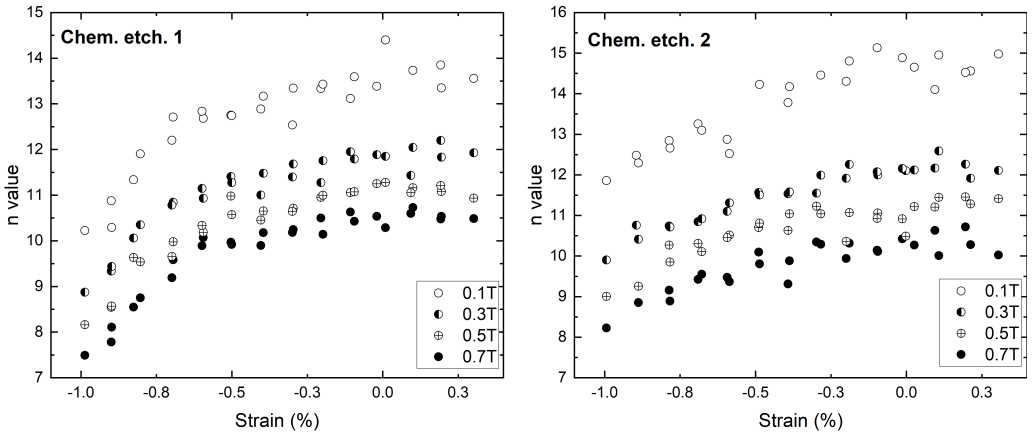

Figure 6.8: The n values versus ε for chem. etch. (1) (left) and (2) (right).

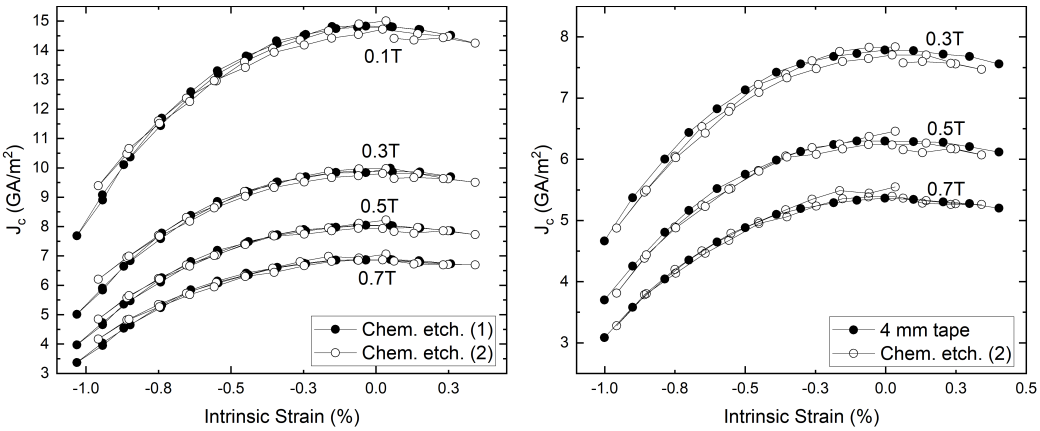

Figure 6.9: Comparing $J_c(\varepsilon)$ curves for chem. etch. (1) and (2) (left), and for a 4 mm tape and chem. etch. (2) (right). $J_{c,peak}$ centred at 0% strain.

subtracting the strain of the maxima (ε_m) from each strain value to centre the peak at 0 %. A new set of intrinsic strains given by $\varepsilon_{int} = \varepsilon - \varepsilon_m$ were therefore defined. Fig. 6.7 shows the $J_c(\varepsilon_{int})$ curves for chem. etch. (1), where the solid lines represent the parabolic fits around the peak of the data. From the table in Fig. 6.7 it can be seen that ε_m is at maximum around 0.05 %, and is independent of the magnetic field.

The corresponding n value versus strain for chem. etch. (1) and (2) are shown in Fig. 6.8. It can be seen that the n value follows a similar trend to J_c. This similarity between the n value and J_c dependencies has been seen in previous work done measuring Nb_3Sn strands under strain [168].

Comparison of the Strain Curves

Chem. etch. (1) and (2) were chemically etched samples on which $J_c(\varepsilon_{int})$ was measured, and a superposition of the two curves is shown in Fig. 6.9, where it can be seen that the strain curves are reversible, such that measurements on applying strain and returning to zero strain had the same I_c values. This confirmed that the strain gauge was reliably measuring the strain in the

REBCO layer, and the tracks were not being damaged during the strain cycle.

The two curves in Fig. 6.9 are in good agreement, and confirm that the strain curves of the etched tracks are reproducible. Fig. 6.9 also shows a comparison of $J_c(\varepsilon_{int})$ for a full-width tape (data from [156]) and chem. etch. (2) using a criterion of $E_c = 100\,\mu\mathrm{Vm}^{-1}$ (the baseline of chem. etch. (1) was too noisy to enable the extraction of I_c values at $E_c = 100\,\mu\mathrm{Vm}^{-1}$). The figure shows that there is consistency between $J_c(\varepsilon_{int})$ of a full-width tape and the chemically etched tracks, and hence the chemically etched tracks can successfully be used to characterise the J_c versus strain dependence at 77 K of REBCO CCs.

6.4.2 $J_c(\varepsilon)$ of FIB Track

We now present the $J_c(\varepsilon)$ of the FIB tracks and see if their behavior is comparable to chemically etched tracks.

The ε dependence of the small FIB tracks was measured in the same way as the chemically etched tracks. However, due to their small size, these tracks were susceptible to damage and their I_c values degraded easily, especially during the soldering process and on applying ε, which would cause cracks to easily propagate across the narrow track width. Therefore, extra care was taken to reduce degradation, including minimising heat exposure with quick soldering times of maximum 10 seconds. Furthermore, the FIB milled tracks themselves were very costly to make, due to the high cost of the FIB milling process. Therefore, $J_c(\varepsilon)$ was only measured on four FIB tracks, and their $J_c(\varepsilon)$ data is shown in Fig. 6.10.

FIB (1) was the first sample to be measured. On applying compressive strain, the J_c decreased rapidly by $\approx 80\,\%$ from $0\,\%$ to $-0.8\,\%$, compared to the chemically etched samples that decreased only by $\approx 30\,\%$ over this strain

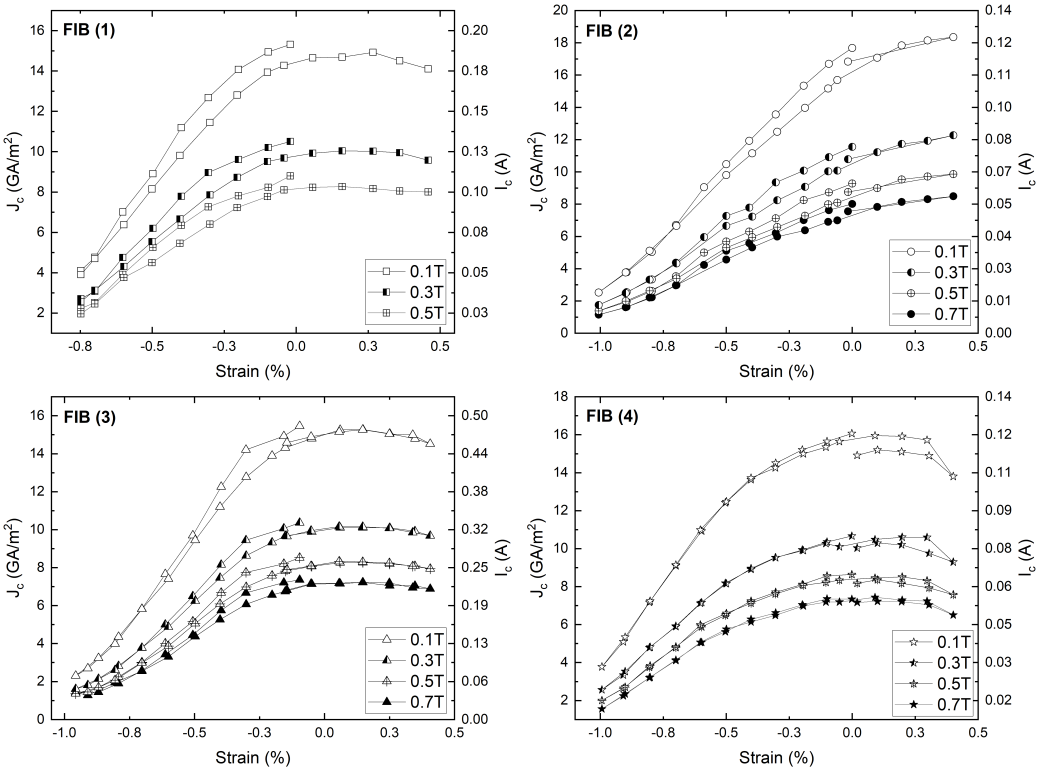

Figure 6.10: $J_c(\varepsilon)$ curves for the FIB samples.

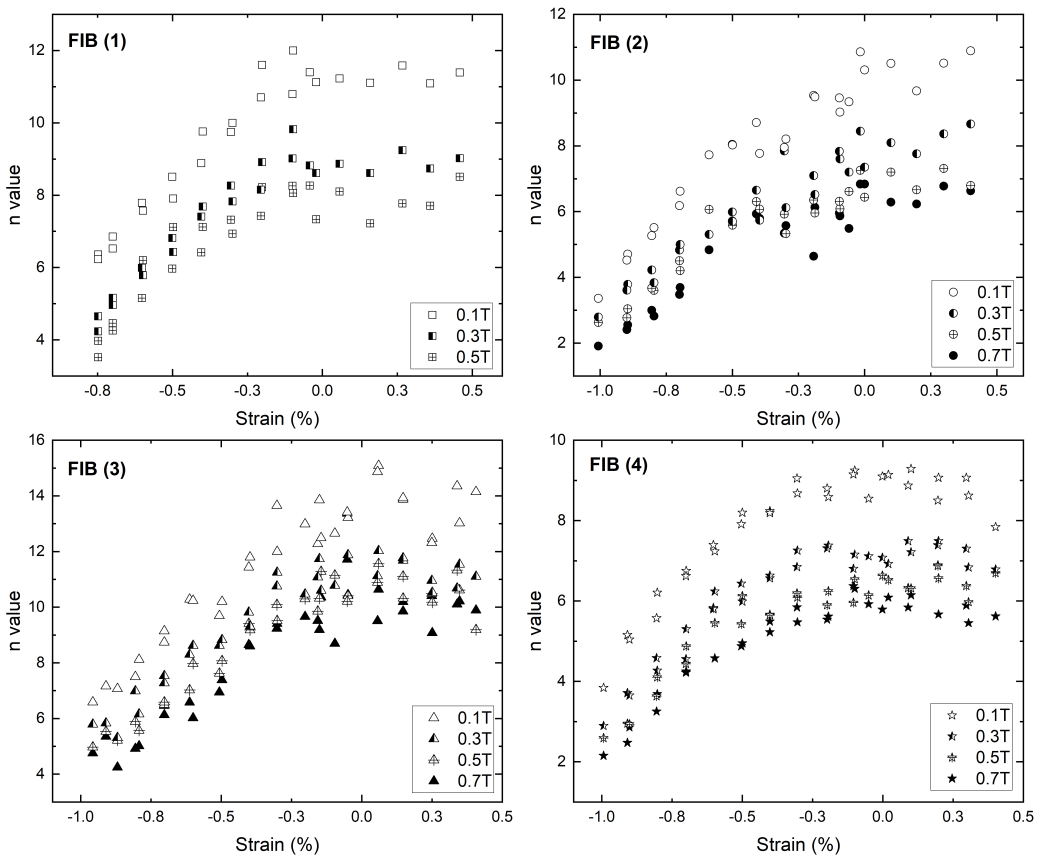

Figure 6.11: The n values versus ε for the FIB samples.

range. It was initially thought that the REBCO had degraded, however on removing the strain, the J_c recovered to 93 % of the initial $J_c(0)$. The compressive region of the strain cycle was not perfectly reversible and this will be discussed further. Afterwards, a tensile strain was applied, and J_c continued increasing until around 0.2 % strain, where the peak occurred. This sample was taken further into tension up to 0.5 % to investigate the peak region; it permanently degraded at 0.6 % strain. Due to limitations of the current delivered by the Glassman LV60-18, 60 V, 18 A magnet power supply at the time, only fields up to 0.5 T could be reached. However for subsequent measurements, the Xantrex XPD120-4.5, 120 V, 4.5 A higher voltage power supply was used and enabled measurements at fields up to 0.7 T. Fig. 6.11 shows that the n values followed a similar behavior under strain as J_c.

FIB (2) was the next FIB track for which $J_c(\varepsilon)$ was measured. Again there was found to be a large drop in J_c by ≈ 70 % from 0 % to -0.8 % strain, which recovered on releasing the strain to 93 % of its initial $J_c(0)$ value. The J_c again continued to rise under tension, where no peak was observed up to the highest strain measured of 0.4 %. A final check of $J_c(0)$ after tension proved that the sample had not degraded. The $J_c(\varepsilon)$ curve still showed a hysteresis on applying and releasing the strain measurements, and the n values again followed the same trend as the J_c values under strain.

FIB (3) had a slightly wider track of 17.8 µm, but despite this still produced a steep drop in J_c of 70 % from 0 % to -0.8 % and a shift in $J_{c,peak}$ to the tensile region. The reversibility of the curves was however slightly better in the up and down strain sweeps. One noticeable feature of this curve was a slight curvature at the high compressive strains.

FIB (4) produced a strain curve that had less hysteresis, but some degradation occurred after applying 0.4 % strain. The J_c dropped by around 55 % from 0 % to -0.8 % strain. The shift of the peak to the tensile region was once again observed.

The hysteresis in the J_c versus strain curves of the FIB samples could be due to several reasons. One possible explanation is that the SG reading was not able to accurately represent the strain state of the very small 100 µm long FIB track simply due to its small size, such that the strain measured by the SG may have been different to the strain in the FIB track. This would be especially true if the strain distribution of the strain board was not completely uniform. Also, if plastic deformation of the strain board was occurring this would also cause a hysteresis between the SG reading and the actual strain in the track. Another explanation for the hysteresis could be due to some delamination of the track on applying strain as this would cause a change in the amount of current shunting for different strains.

There were three noticeable characteristics of all the FIB $J_c(\varepsilon)$ curves that were not seen for the chemically etched or full-width tapes. The first is an unusually large drop of J_c in compression compared to the chemically etched tracks. The second is a large shift in $J_{c,peak}$ of the strain curve to the tensile region. Table 6.2 gives the strains at which this peak occurs (ε_m) for all samples, found by fitting a quadratic parabola from $0.95J_{c,peak}$ to $J_{c,peak}$. The table shows that the peaks occurred above 0.15 % for the FIB samples compared to below 0.05 % for the chemically etched samples. The third characteristic was a slight curve or tail-off of the FIB strain curves, especially FIB (2) and (3), at high compressive strains.

Table 6.2: The strains at which $J_{c,peak}$ occurs for all samples.

	Chem. Etch. (1)	Chem. Etch. (2)	FIB (1)	FIB (2)	FIB (3)	FIB (4)
ε_m	0.044%	0.01%	0.201%	0.399%	0.146%	0.155%

There are several explanations for the large drop in J_c and shift in $J_{c,peak}$ seen. One explanation could be the current distribution, where instead of assuming that the current shunting through the strain board is negligible,

it could instead be non-zero and change as we apply strain. To explain the large drop in J_c by current redistribution, the amount of current shunting would need to decrease on applying compressive strain, forcing I_c to drop much more under compression. This could potentially have occurred if there was delamination at the current injection points, increasing the resistance of the shunt path. One other reason for the large drop in J_c could be due to an unknown strain state of the track, or if the track buckles creating a high stress concentration, although in this case we would expect the fragile track to break and degrade J_c. The reason for the large shift in $J_{c,peak}$ could be due to a thermal pre-strain, although this pre-strain is large compared to the chemically etched tracks (>0.1 % compared to <0.05 %). The position of ε_m is also always in tension for the FIB tracks, whereas a thermal pre-strain can be compressive or tensile. Therefore thermal pre-strain is unlikely to be the reason for the large offset in $J_{c,peak}$.

Despite the considerations, we proceed assuming there were no experimental artifacts, and consider the explanation to be associated with the domain structure and the fraction of each domain within the small FIB tracks. A higher volume fraction of A domains compared to B domains in REBCO will cause a shift in the $J_{c,peak}$ to the tensile region as explained in Chapter 3. Therefore it is possible that there is a higher fraction of A domains compared to B domains in the FIB tracks, potentially caused by the FIB milling detwinning the REBCO.

Comparison of the Strain Curves

To compare the $J_c(\varepsilon)$ curves of the FIB samples, to test for repeatability, the data was treated in three different ways. In each case only the half-cycle is used from -1 % strain to 0.4 % strain and compared at 0.5 T. The first comparison involved plotting the raw strain curves, whereby $J_c(\varepsilon)$ was normalised by dividing by $J_c(0)$ and the curves were not shifted but instead kept with their peaks occurring at their original positions given in Table 6.2.

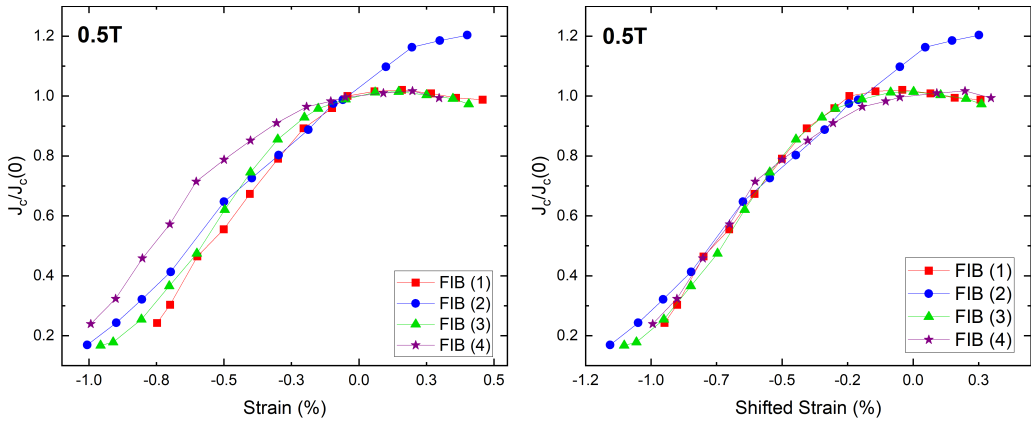

Figure 6.12: Comparison of the FIB strain curves at 0.5 T from $-1\,\%$ to $0.4\,\%$ strain. Left: raw curves normalised to $J_c(0)$. Right: curves normalised and arbitrarily shifted to align their compressive strain region.

This is shown in Fig. 6.12, and it can be seen that FIB (1), (3) and (4) are similar around the peak region, whereas FIB (1), (2) and (3) have similar sized drops of J_c in compression.

In the second treatment, the curves were again normalised, but were shifted to align their compressive regions as shown in Fig. 6.12. In this case the ε_m values of Table 6.2 were not subtracted as in previous treatments, but instead the compressive regions were aligned to give the best superposition of the curves. It can be seen that the slope of the graphs in the compressive region are similar for all samples, and there is overall a good agreement of FIB (1), (3) and (4), although FIB (2) appeared to have a much larger $J_{c,peak}$.

This initial analysis suggests that there is not much repeatability between the samples, as each curve has a different steepness and strain at which $J_{c,peak}$ occurs. Fig. 6.12 however suggests that if we account for the differences in the strain at which the peak occurs, the compressive regions of three of the four FIB samples (i.e. FIB (1), (3) and (4)) are similar.

A comparison of a FIB sample to the chemically etched sample is shown in

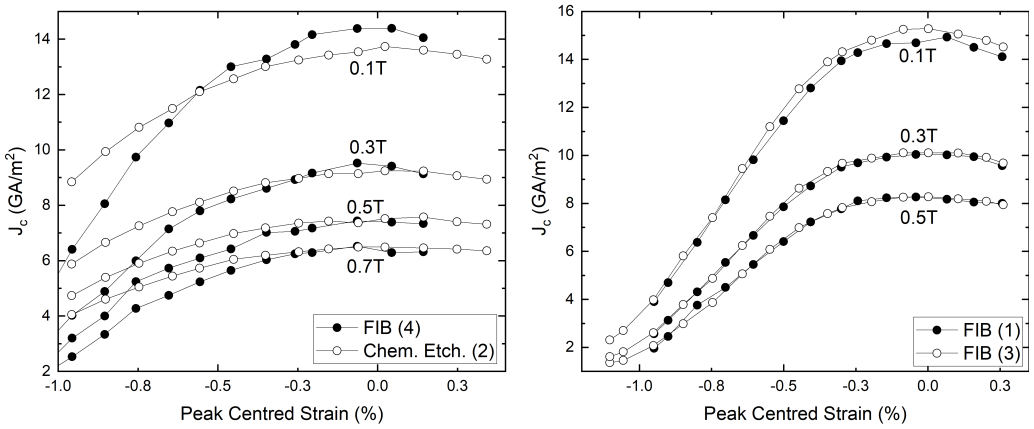

Figure 6.13: J_c versus ε for FIB (4) and chem. etch. (2), with $J_{c,peak}$ centred at 0 % strain (left). J_c versus ε for FIB (1) and FIB (3) with $J_{c,peak}$ centred at 0 % strain (right).

the left figure of Fig. 6.13, where chem. etch. (2) is compared to FIB (4), both with the $J_{c,peak}$ centered at 0 %. Instead of denoting this new strain as an intrinsic strain (ε_{int}), which we referred to previously as the REBCO strain with the thermal pre-strain removed, we refer to it here as a peak centred strain, because the sole cause for the shift in $J_{c,peak}$ for the FIB data it not just a thermal pre-strain but also a consequence of the different domain structure of the FIB tracks. It is clear that the FIB J_c strain sensitivity is quite different to the chemically etched or full-width one due to its steeper drop in J_c with strain. Hence FIB milled samples cannot be used to characterise the strain dependence of full-width REBCO tapes, the field dependence however is mainly in agreement. The right-hand graph of Fig. 6.13 shows the strain curves of FIB (1) and (3) which superpose well, suggesting that there is some consistency between the $J_c(\varepsilon)$ of the FIB tracks.

From the characteristics of the FIB $J_c(\varepsilon)$ data, we attribute the difference in the $J_c(\varepsilon)$ behaviour for the FIB tracks compared to the chemically etched tracks, to the different fractions of each domain in the REBCO tracks. In the following section we investigate this hypothesis further by extracting the

domain fractions of each FIB track by fitting the $J_c(\varepsilon)$ curves to the bimodal chain model, with the A-domain fraction f as a fitting parameter. After this we investigate the domain landscape of the REBCO layer of the tracks by using EBSD to image the REBCO crystal orientation, from which we directly measure the area fraction of each domain. The results from these investigations are presented in sections 6.4.3 and 6.4.4 respectively.

6.4.3 Fitting the Curves to the Chain Model

Here we present the results for the fits of the $J_c(\varepsilon)$ data to the bimodal chain model. We present two approaches, the first approach (fit 1) follows the theory described in [103] and presented in section 3.4.3, treating the A and B domains to have the same linear but opposite responses of J_c to strain, characterised by the parameter g. In the second approach (fit 2), we follow the theory described in [114], which comprises of a more involved treatment of the strain response of J_c for each domain, using the results from measurements of $J_c(\varepsilon)$ found for each domain and presented in Fig. 3.12.

In the fit 1, for each $J_c(\varepsilon)$ curve we fit the chain model given by equation 6.1, which is a rearranged form of equation 3.11.

$$J_c(\varepsilon) = J_c(0)\left[f(1+g\varepsilon)^{-n} + (1-f)(1-g\varepsilon)^{-n}\right]^{-1/n} \tag{6.1}$$

Where g is the strain sensitivity of J_c and has a field and temperature dependence given for an HTS material by [103]

$$g_{HTS} = \left|\frac{dT_c^*}{d\varepsilon}\right|_{\varepsilon=0\%} \frac{1}{T_c^*(0)}\left[2\frac{1+t^2(0)}{1-t^2(0)} + \left(\frac{st(0)}{1-t(0)} + w\right)\left(\frac{qb(0)}{1-b(0)} + n' - p - 2\right)\right] \tag{6.2}$$

Where $t(0) = T/T_c^*(0)$ and $b(0) = B/B_{c2}^*(T,0)$ at $\varepsilon = 0\%$, with T_c^* and

B^*_{c2} being the effective critical temperature and effective upper critical field respectively and n the index of transition and $|dT^*_c/d\varepsilon|$ the magnitude of the strain dependence of the critical temperature of a single domain. In our fit, $T^*_c(0)$ and $B^*_{c2}(0,0)$ were set as fixed parameters and assigned values typical for REBCO, as well as w, s, n', p and q, which are constants that come from the scaling law of the flux pinning force dependence on magnetic field and temperature [103]. We set $T^*_c(0) = 91\,\mathrm{K}$, $B^*_{c2}(0,0) = 103\,\mathrm{T}$, $w = 3$, $s = 1.25$, $n' = 2.5$, $p = 0.5$ and $q = 2$, which are values measured for REBCO in previous literature [103].

The fitting parameters in the model were $J_c(0)$, f and $\frac{dT^*_c}{d\varepsilon}$.

In fit (2), we use different functions for $J_{ci}(\varepsilon)$ given below, that take into account the parabolic strain dependence of J_{cA}, and the higher strain sensitivity of J_{cA} compared to J_{cB} by roughly a factor of two. We use these functions in the standard chain in equation 3.11, so

$$J_c(\varepsilon) = J_c(0)\left[f\left[1 + g_A(\varepsilon_{A-max})^2 - g_A(\varepsilon - \varepsilon_{A-max})^2\right]^{-n} + (1-f)\left[1 - g_B\varepsilon\right]^{-n}\right]^{-1/n} \tag{6.3}$$

where

$$J_{c,A} = J_{c,A-max} - J_{c,A}(0)g_A(\varepsilon - \varepsilon_{A-max})^2 \tag{6.4}$$

$$J_{c,B} = J_{c,B}(0)(1 - g_B\varepsilon) \tag{6.5}$$

and $J_{c,A-max} = J_c(0)(1 + g_A\varepsilon^2_{A-max})$. Here g_A and g_B are the strain sensitivities of J_c in the A and B domains respectively and ε_{A-max} is the strain at which the peak in the strain curve of the A domain occurs. We made the assumption that $J_{c,A}(0) = J_{c,B}(0) = J_c(0)$ at zero applied strain following Suzuki [114], and using $J_c(0)$ f, g_A, as fitting parameters, setting $g_B = 0.2$ and $\varepsilon_{A-max} = 0.35\%$ as global fixed parameters using values similar to the

literature [114].

Table 6.3 gives the values of the parameters extracted from fit 1 [117] and Table 6.4 gives the parameters values of fit 2 [114]. For fit 1 it can be seen that the values of g vary a lot for each sample where we would expect g to be constant. The values of g_A from fit 2 also seem to vary but are in general in closer agreement with the literature values of around 0.4 [114]. The values of $J_c(0)$ extracted from the two fits are also consistent as we would expect.

In terms of the f values, it can be seen that for fits 1 and 2, the f values for chem. etch. (1) and (2) and the 4 mm tape are around 0.5, suggesting that in these tracks, around 50 % of the REBCO area is A domain and 50 % is B domain, as expected and found previously for MOCVD REBCO tapes. This suggests that the chemically etched tracks have a microstructure that is representative of the full-width tapes.

Table 6.3: Fitting parameters extracted from bimodal fit 1 to all $J_c(\varepsilon)$ curves for all samples at 0.5 T.

Sample	$J_c(0)$ (GA/m^2)	f	$\frac{dT_c^*}{d\varepsilon}$ (K/%)	g (/%)
4 mm Tape	8.74	0.51	5.501	0.794
Chem. etch. (1)	8.057	0.511	5.788	0.835
Chem. etch. (2)	7.855	0.498	5.499	0.793
FIB (1)	8.056	0.688	7.875	1.136
FIB (2)	8.511	0.889	5.965	0.861
FIB (3)	8.277	0.696	6.555	0.945
FIB (4)	8.49	0.573	6.108	0.881

The f values for the FIB samples however are all greater than 0.5 for fits 1 and 2, suggesting that a larger fraction of the area in the tracks is occupied by A domains compared to B domains for all tracks. We expect there to be some variation in the f value as each FIB milling process is likely to have a slightly different effect on the REBCO microstructure. Despite the differences, both

Table 6.4: Fitting parameters extracted from bimodal fit 2 to all $J_c(\varepsilon)$ curves for all samples at 0.5 T with the fixed parameters $g_B = 0.2$ and $\varepsilon_{peak} = 0.35\%$. $J_c(0)$ assumed the same for the A and B domains and found to be consistent with fit 1.

Sample	$J_c(0)$ (GA/m^2)	f	g_A (/%)
4 mm Tape	8.70	0.50	0.30
Chem. etch. (1)	8.01	0.49	0.35
Chem. etch. (2)	7.82	0.47	0.29
FIB (1)	8.12	0.78	0.71
FIB (2)	8.53	1	0.55
FIB (3)	8.1	0.80	0.58
FIB (4)	8.41	0.57	0.48

fits provide further evidence that the domain structure within the FIB tracks has been changed by the FIB milling, causing it to be partially detwinned.

Due to the increased complexity and more thorough treatment of the behaviour of A and B domains under strain provided by fit 2, we present the strain curves with the chain model fits from fit 2 for all FIB samples in Fig. 6.14, and both chemically etched tracks and the 4 mm tape in Fig. 6.15. All strain curves fit to the chain model very well.

In the next section we present the images of the landscape of A and B domains within the REBCO layer found using EBSD, and see if the fractions of each domain match with the results from the chain model fits.

6.4.4 EBSD

In this section, the results from the EBSD analysis are presented. EBSD is a technique that can determine the grain structure and crystal orientation of a thin layer of a material.

In this technique, electrons are fired at the surface of a specimen that is tilted

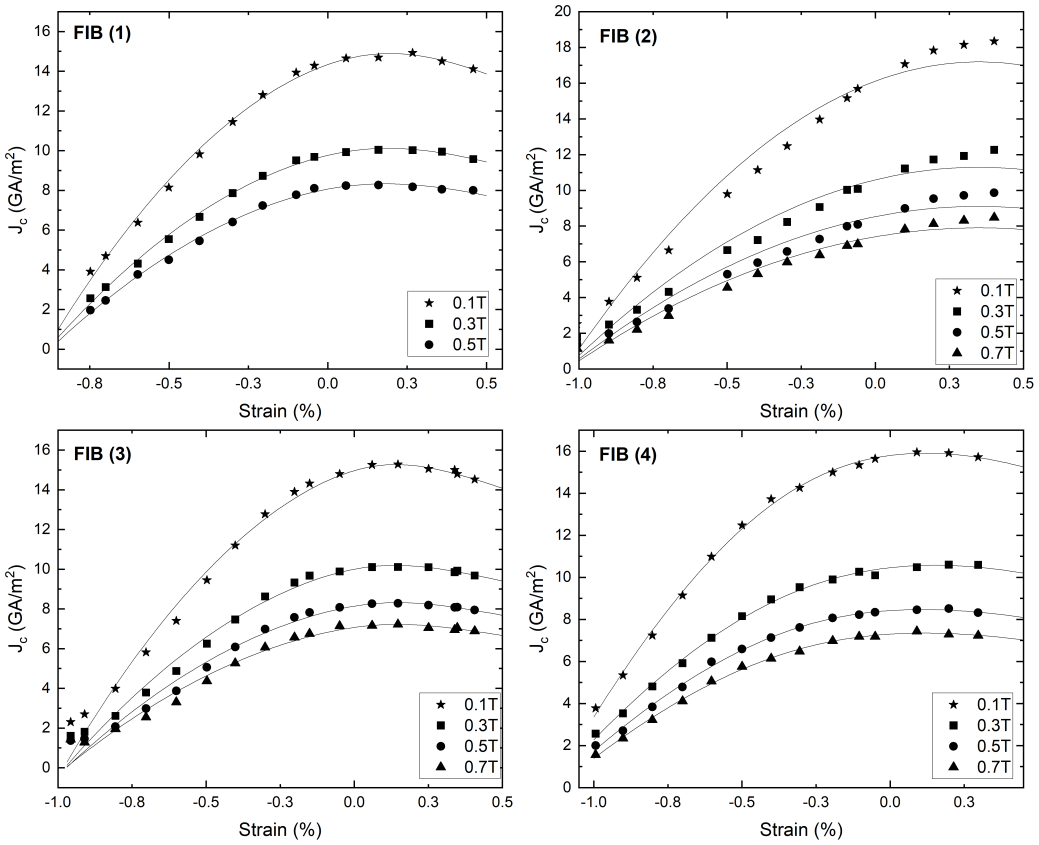

Figure 6.14: Raw J_c versus ε curves and fits to the bimodal chain model (fit 2) for all FIB tracks.

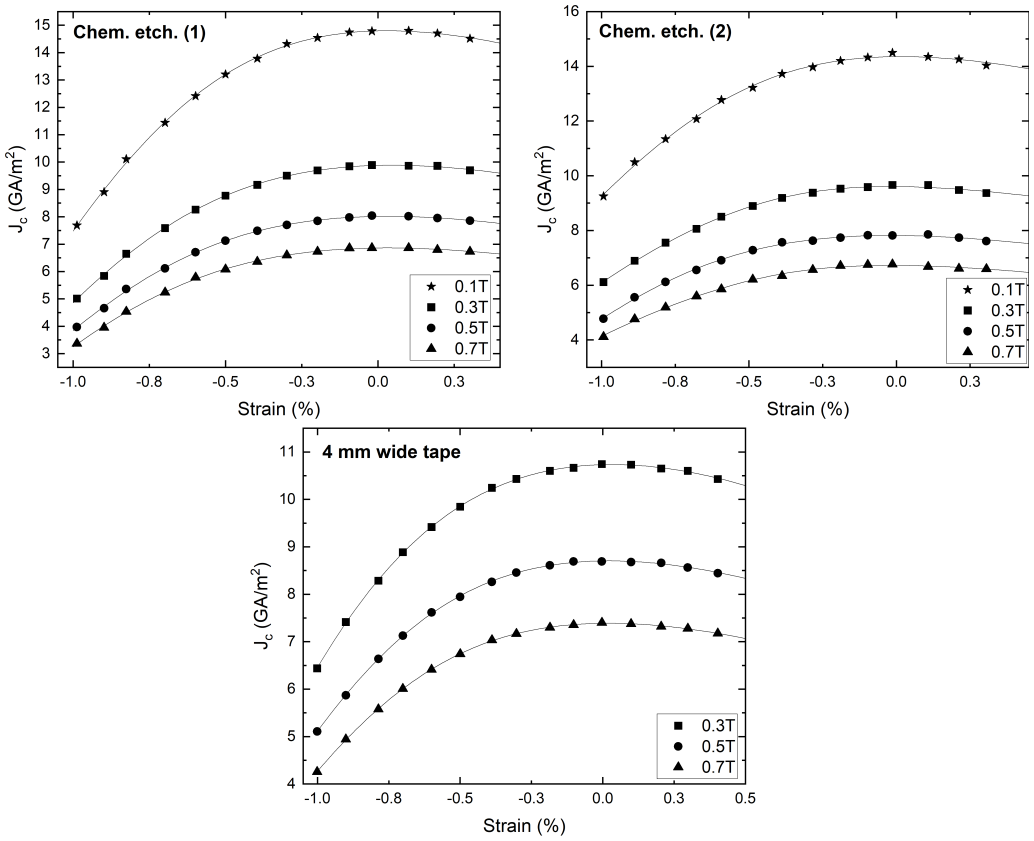

Figure 6.15: Raw J_c versus ε curves and fits to the bimodal chain model for the chemically etched tracks (top) and the 4 mm wide tape (bottom).

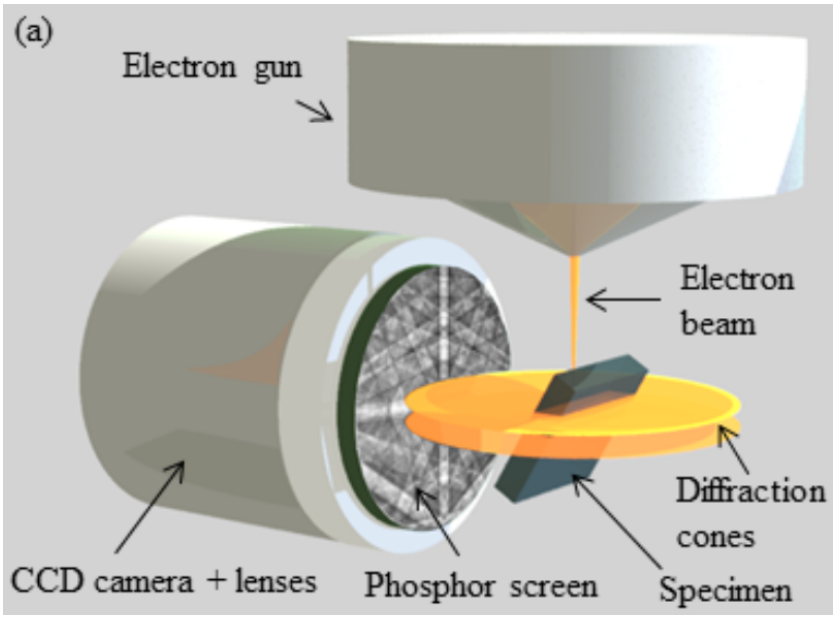

Figure 6.16: The experimental setup of EBSD showing the incident electron beam interacting with the tilted sample and producing a diffraction pattern on a phosphor screen [169].

by $\approx 70°$. The electrons interact with the crystal formed by the surface layers of atoms, tens of nanometers deep into the surface, and are backscattered forming a diffraction pattern. The diffraction pattern is then captured by a CCD camera for processing. The setup for EBSD is represented in Fig. 6.16.

The first step was to remove the copper and silver coatings from the REBCO tapes to expose the REBCO layer underneath. This was done using the solution of ammonia and hydrogen peroxide described in Chapter 5. To clean the samples afterwards, they were rinsed with acetone, with care taken to keep the REBCO surface away from water with which it would react.

The samples themselves were now a thin 1.6 µm layer of ceramic REBCO, and therefore already had a flat, glass-like surface for EBSD. The sample preparation, specifically the surface polishing, was very important as the electrons

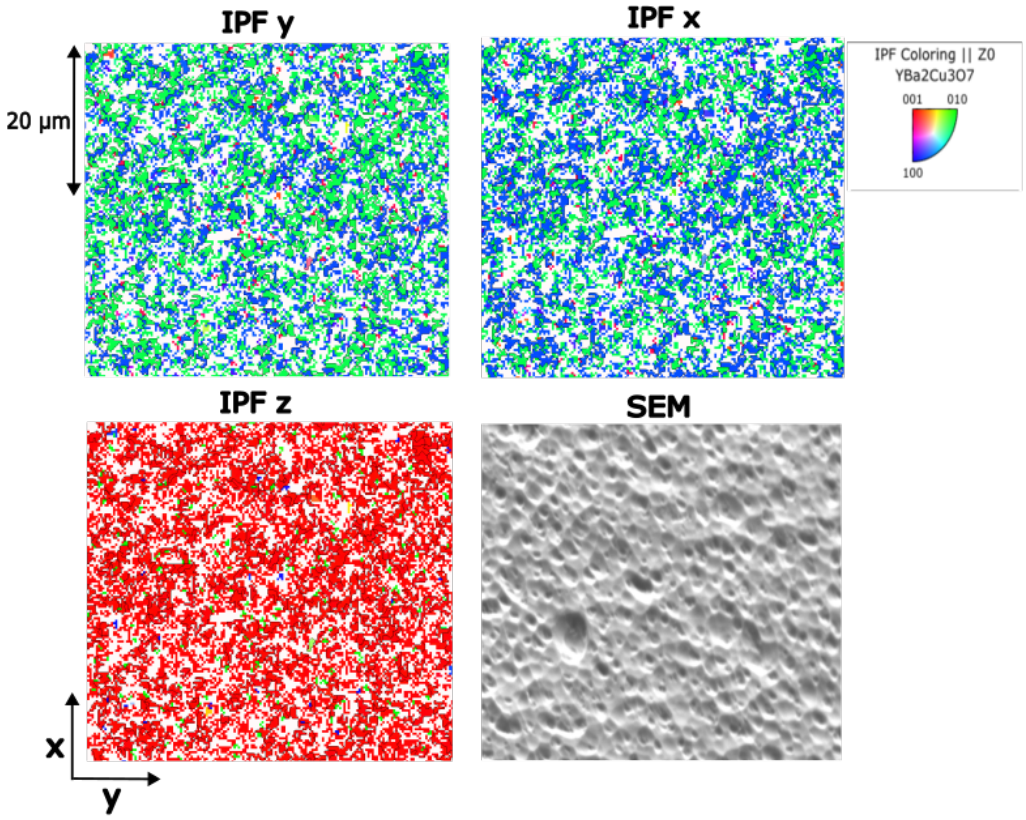

Figure 6.17: IPF maps and SEM images of 4 mm tape (1). Sample polished using mechanical and argon ion polishing (1 hour).

only interact with a thin layer in the surface of the material, so the surface must be very flat to get high quality Kikuchi patterns [170]. Preliminary attempts of EBSD on the unpolished samples failed as the surface was not flat enough to within the few nano-meters required. This was due to precipitates and a-axis grains protruding out from the surface. The samples were therefore polished using mechanical polishing followed by argon-ion polishing as described in the literature [171].

Argon ion polishing was done using two 30 kV, 5.5 nA argon ion beams at a low incident (2°) angle. Different times and combinations of the mechanical

and argon ion polishing were investigated to find the best settings. Firstly, mechanical polishing along with a long argon ion beam exposure of 1 hour was tested. This amount of polishing, applied to the 4 mm tape (1), removed the precipitates and a-axis grains shown in the SEM image of the 4 mm tape (1) shown in Fig. 6.17. This produced a very flat surface and resulted in a high fraction of indexing from the EBSD (around 60 % YBCO and 40 % zero solutions). The EBSD data show the orientation of the REBCO unit cell for each pixel of the SEM image taken. The pixel size was chosen to be 0.2 µm, which was smaller than the average size of a domain. Inverse polarity figure (IPF) maps were obtained for the x, y and z directions of the sample, where x is along the tape length, y is along the tape width, and z is normal to the tape surface. An IPF map gives information on which lattice parameter is aligned with the direction measured, where red corresponds to the (001) or c-axis, blue the (100) or a-axis, and green the (010) or b-axis. For all 4 mm tapes measured, IPF z is mainly red, suggesting that the c-axes of the unit cells are aligned to the tape normal, and IPF x and y are roughly 50 % green and 50 % blue with the exact ratios given in Table 6.5. This suggests that the A and B domains have roughly equal areas within the 4 mm width tapes, in agreement with the fits to the bimodal chain model.

This polishing was successful for the 4 mm tape (1), however for some samples, caused a false-indexing and failure to distinguish the c-axis from the a-axis. This false indexing was due to the Kikuchi patterns for the a and c axis aligned YBCO being very similar [172]. A way to determine whether the EBSD mapping had not produced false indexing was to check that the c-axis was aligned with the z direction (normal to the tape) for all pixels. In other words, for the Inverse Polarity Figure (IPF) in the z direction to be mainly red, shown in Fig. 6.17.

Since this level of polishing had produced some EBSD maps which were incorrect, it was decided to use a minimal level of polishing of just 5 minutes

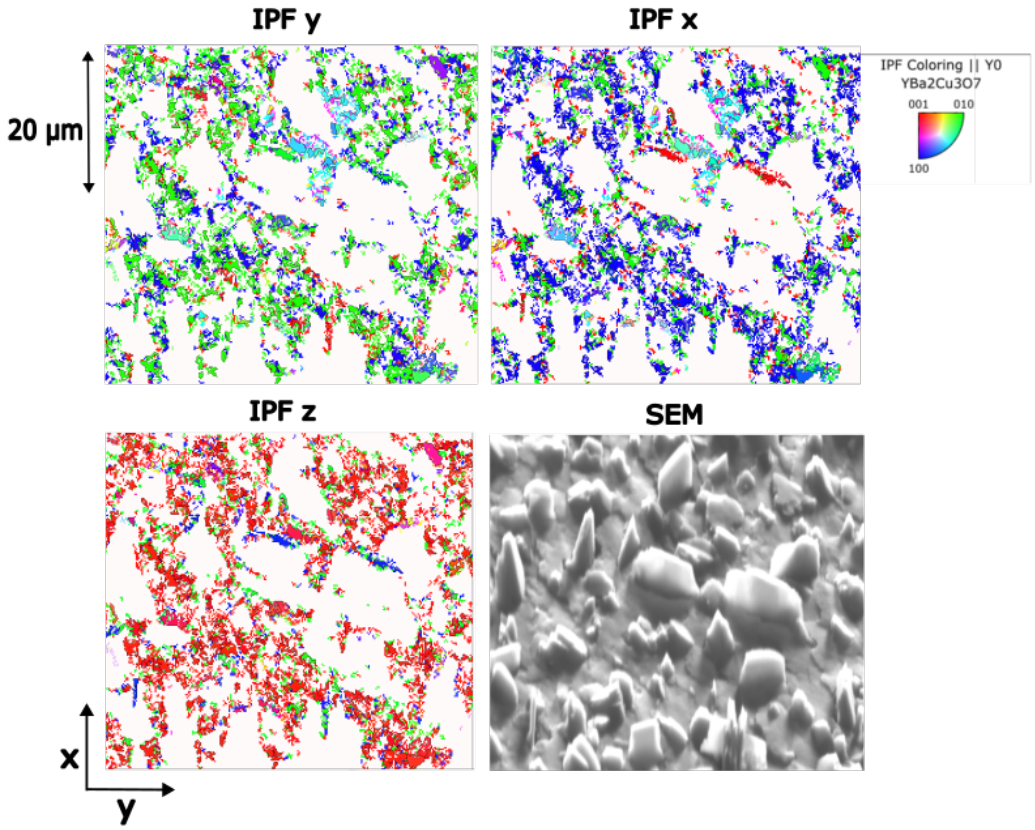

Figure 6.18: IPF maps and SEM images of 4 mm tape (2). Sample polished using argon ion polishing (5 minutes).

under the Argon ion beam for samples 4 mm (2) and (3), as suggested in previous work [170], [171]. No mechanical polishing was used here to reduce the chance of the crystal structure being damaged at the sample surface. This polishing led to a low fraction of indexing (30 % YBCO and 70 % zero solutions), and did not remove the precipitates and a-axis grains, as shown in the SEM in Fig. 6.18. Despite this, the polishing technique produced consistently successful maps where we see that IPF y and IPF x are predominantly mixed green-blue and IPF z is predominantly red.

To apply EBSD to the FIB tracks was more difficult; a thorough cleaning

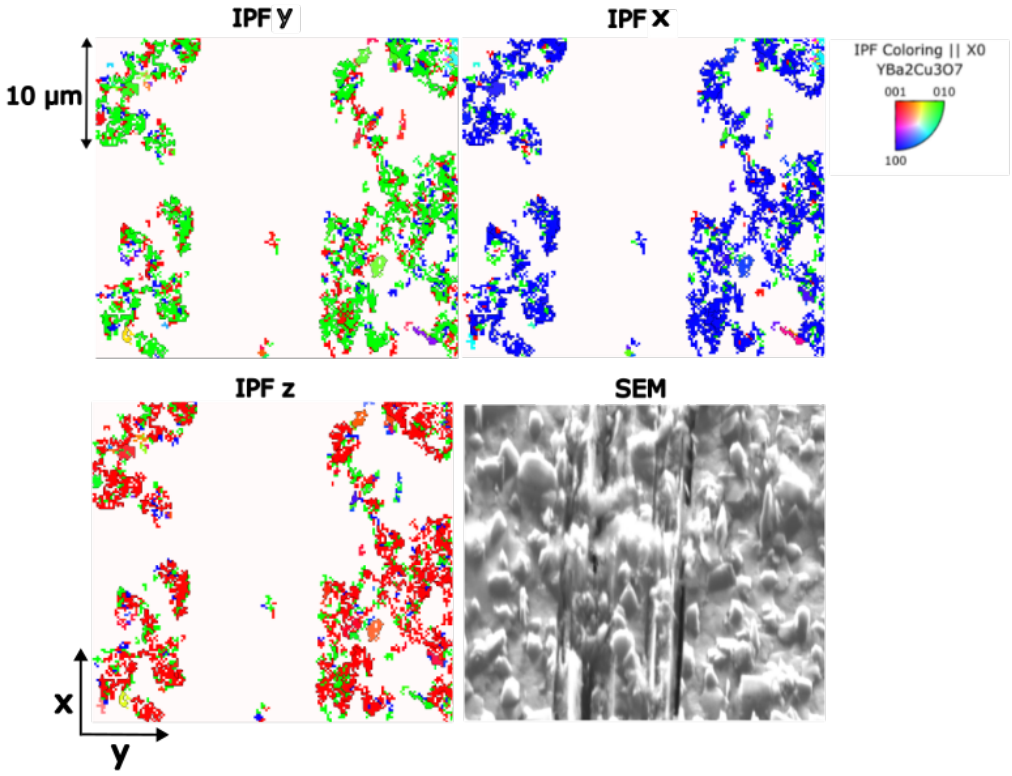

Figure 6.19: IPF maps and SEM images of FIB (1). Sample polished using argon ion polishing (10 minutes).

with acetone was needed to remove the residue from within the tracks which was hard to do. The tracks were then polished with the argon ions for 10 minutes to try to improve the fraction of indexing. Unfortunately, the small REBCO tracks were easily damaged during the cleaning process, shown in the SEM in Fig. 6.19, and so the area within the track could not be indexed properly. The area outside of the tracks was however well indexed, and was used as indicative of the area within the tracks.

For the FIB samples, of which two were measured, the ratio of blue to green area in the x direction was around 80 %/20 %, suggesting a higher fraction of A-domains in and around the track. This also broadly agrees with the fits

of the FIB I_c data to the bimodal chain model, which found the A-domain area fraction to be between 60 % and 90 %.

Table 6.5: The samples on which EBSD images were taken, along with the measured volume fraction of each domain.

	4 mm tape (1)	4 mm tape (2)	4 mm tape (3)	FIB (1)	FIB (2)
Polishing	Mech + Ar(1 hr)	Ar(5 mins)	Ar(5 mins)	Ar(10 mins)	Ar(10 mins)
A-dom. (%)	55.5	59.9	56.3	85.6	79.6
B-dom. (%)	44.5	40.1	43.7	14.4	20.4

Overall, the results from this investigation provide evidence that the FIB milling we have used physically changed the domain fractions of the REBCO in the tracks, which in turn changed the track J_c response to ε. The milling process using high energy (30 keV) gallium ions could be changing the crystal structure in a way that depends on the direction that the milling occurs, causing the REBCO to be A-domain richer along the track length. Similar changing of the crystal structure from FIB milling has been seen in other materials, such as steels, where FIB milling has caused an austenite to martensite phase transformation [173], so it is possible for a similar crystal change to be occurring in the REBCO. It has further been shown that applying heat and strain to a twinned REBCO layer can cause it to become detwinned and single domain [142]. The incident gallium ions from the milling could be generating some heating and lattice strain from implantation of the gallium ions that then causes a detwinning of the REBCO, in addition to displacing the oxygen atoms within the REBCO unit cell.

6.5 Conclusion

In this chapter, the results of the J_c dependence on ε for narrow tracks of REBCO CC down to 5 µm wide made using chemical etching and FIB

milling were presented. It was found that, although the chemically etched tracks produced $J_c(\varepsilon)$ curves that matched the 4 mm wide tapes, the curves from the FIB tracks did not match, and instead showed a large shift of $J_{c,peak}$ into the tensile strain region, and a steeper drop in J_c under compression. Therefore, FIB tracks cannot be used to characterise the dependence of J_c on ε for full-width REBCO tapes.

The reason for the different $J_c(\varepsilon)$ dependencies for the FIB tracks was attributed to a different domain landscape within the FIB tracks. This was investigated by imaging the REBCO layer using EBSD, the results from which provided evidence for the 4 mm tapes having approximately 50 % of each domain fraction, and the FIB samples having a much higher fraction of A-domains, around 80 % along the track. These results were consistent with the findings from the fits to the chain model.

A further test to investigate whether the different strain behaviour of the FIB tracks is due to a high fraction of A domains is to apply strain in the orthogonal direction of the tape (in the y direction) and see if we get the B-domain rich result expected. The results from this investigation are presented in the following chapter.

In conclusion, the FIB milling has been found to affect the REBCO microstructure by causing a partial detwinning of the REBCO layer, and hence causing the strain dependence of J_c on FIB tracks to be different to chemically etched tracks and full-width REBCO tapes.

Chapter 7

Final Experiments - A Deeper Understanding of the Critical Current Density

7.1 Introduction

This chapter presents the results of two final experiments. We note that the range of potential experiments on the HTS tapes available, simply to characterise J_c alone is vast. Given the anisotropic properties, different microstructures, and different field, temperature and strain dependencies, it is clear that pilot experiments are required to identify where we should put our effort. This chapter presents work on two such experiments that can pave the way for more detailed future work:

Firstly, J_c measurements are presented at different temperatures between 10 K and 83 K, at different magnetic fields between 0 T and 0.7 T and at different angles between 0 and 180°. The motivation of this work was to characterise the J_c of REBCO CC at very low temperatures down to 10 K,

as the REBCO magnet system of future Tokamaks aims to operate at around 20 K [24]. One easy route to achieve variable temperature is to use a Cold Head, which avoids the use of cryogens and cools via helium gas circulation. To measure J_c using a Cold Head however requires samples with small currents to prevent excess ohmic heating, and so our FIB tracks, which only require currents of only up to 0.2 A, were used to characterise REBCO using the Cold Head. We start by presenting the experimental setup and upgrades made to the Cold Head system to enable variable temperature, field and angle measurements. Afterwards we present the results of the field and angular dependence of J_c for the chemically etched and FIB tracks made in liquid nitrogen and compare to a full-width tape. After proving that the FIB tracks are able to replicate the field and angular dependencies of full-width tapes, we present the results and a preliminary analysis of the full set of $J_c(B, T, \theta)$ data made on a FIB track in the Cold Head.

In the second set of experiments in this chapter, we investigate how the critical current versus strain behaviour changes when the directions of the applied current and strain change with respect to each other.

7.2 Expt 1: Critical Current Density versus Field, Temperature and Angle

7.2.1 Experimental Setup

In this section we present the experimental setup that enabled variable temperature measurements, as well as variable field and angle. By using a Cold Head cryocooler we were not limited to measurements at a single temperature, that of liquid nitrogen, and instead were able to characterise the J_c of REBCO down to 10 K.

The same Cold Head as described in Chapter 4 was used, but to enable

variable temperature as well as field and angle measurements, a few upgrades were made to the Cold Head which previously was only able to measure J_c with no applied field, these upgrades will be described below.

7.2.2 The Cold Head Upgrades

To enable variable field and angle measurements in the Cold Head, the sample platform, radiation shield and vacuum shroud were reconstructed in order to fit between the pole pieces of the horizontal iron core magnet described in Chapter 4.

The new design of the sample platform was similar to that presented in Chapter 6, but with additional groves for the wires to thermally sink them and reduce thermal transfer from room temperature through the wiring to the sample. Temperature control was an important aspect of the setup, and therefore an additional second Kapton heater was installed on the bottom of the sample platform close to the sample and connected in parallel with the pre-existing silicon diode heater located in stage 2 of the Cold Head (see Chapter 4). The interplay between the silicon diode heater and this Kapton heater to balance the cooling from the cryocooler enabled precise control of the sample temperature to within 50 mK. Furthermore, the temperature of the sample was monitored more precisely by installing a platinum resistance thermometer (PRT) next to the sample, along with the Cernox that was installed in a well on the sample platform directly behind the sample (see Fig. 7.1). Due to the higher sensitivity now of the system to the sample temperature, the PID parameters of the temperature controller had to be changed. It was found that P,I and D values of 30, 10, and 0 were optimum.

A new radiation shield and vacuum shroud were designed according to the dimensions of the iron core magnet. The new design included a narrow tail thin enough to fit between the poles of the horizontal magnet, such that the sample connected to the Cold Head was located in the centre between the

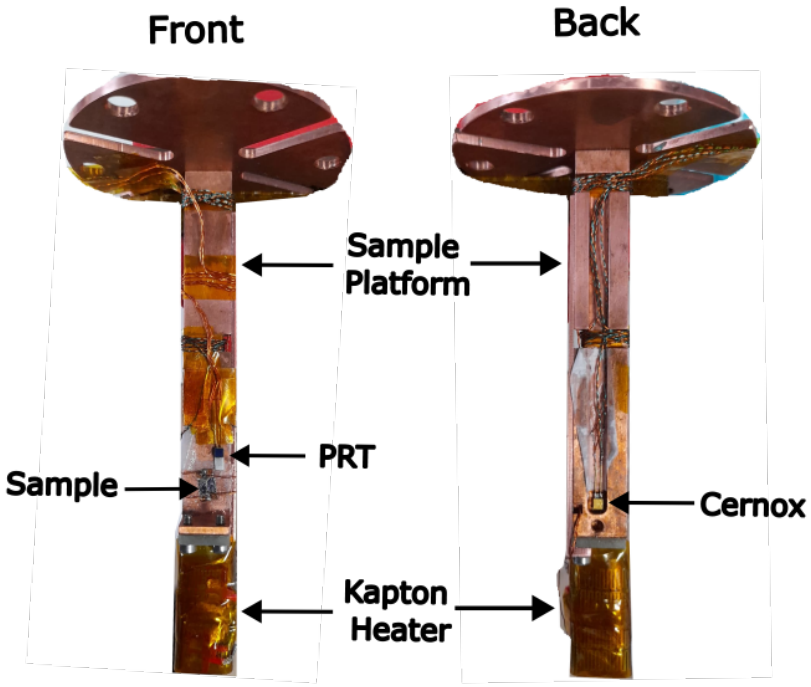

Figure 7.1: The front (left) and reverse side (right) of the sample platform for the upgraded Cold Head.

poles of the magnet. A CAD diagram of the upgraded Cold Head is shown in Fig. 7.2 (cf Appendix I). The angle between the REBCO tape normal and the magnetic field was varied by manually rotating the Cold Head and aligning a marker with the magnet bench-top protractor.

7.2.3 Transport Current Measurements

The free-standing sample was placed substrate side down on the end of the sample platform. The sample was electrically isolated from the copper platform using cigarette paper, and thermal grease was used to improve the thermal contact between the sample and sample platform. As the temperature of the sample depended on conduction through the copper platform, a good thermal contact was necessary to remove excess ohmic heating during

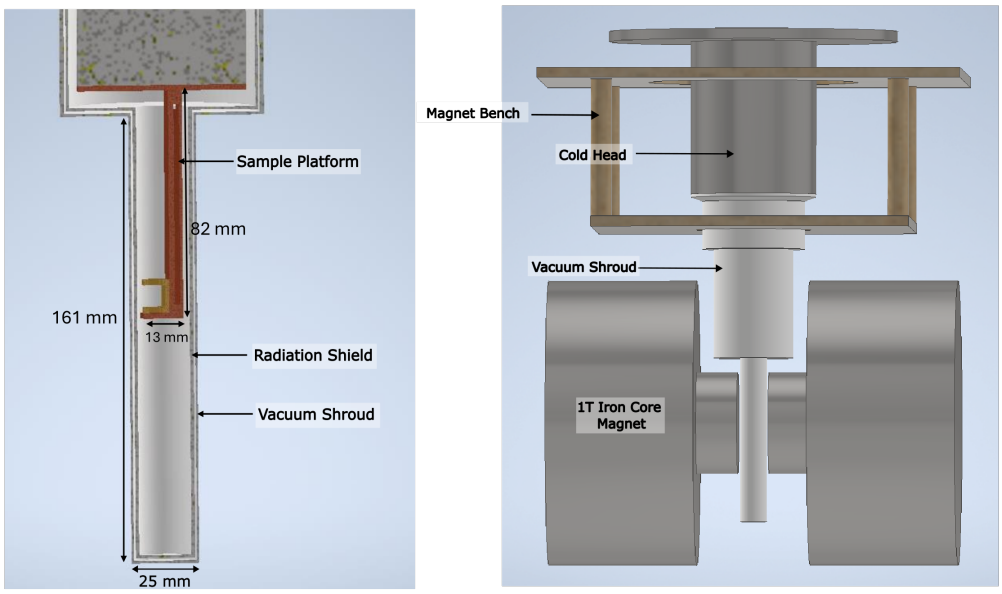

Figure 7.2: The assembly of the upgraded Cold Head sample platform, radiation shield and vacuum shroud (left). Upgraded Cold Head setup with horizontal 1 T magnet (right).

a VI trace, and to ensure the sample temperature was the same as that of the thermometers.

It was found that the size of the sample currents used, and the ramp rate of the current, caused ohmic heating and a local increase in temperature of the sample. Higher currents and longer current ramp rates generated the most heating. The current ramp rate had to be slow enough however for adequate data acquisition. It was found that for a reasonably fast ramp rate of 4 A/min, ohmic heating began to cause a noticeable increase in the sample temperature at about 0.6 A as shown in Fig. 7.3. Therefore, only the 5 µm FIB tracks were used in the Cold Head which only required maximum currents of 0.5 A.

The direction of the current through the sample was such that the Lorentz

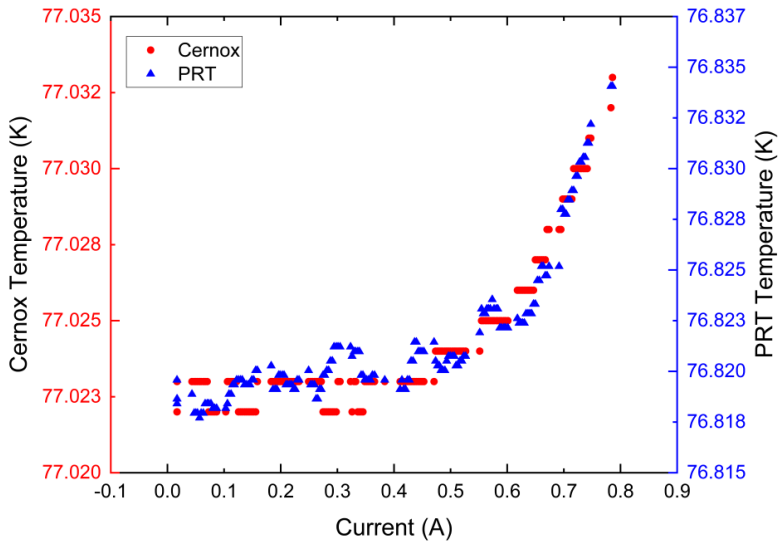

Figure 7.3: Increase in temperature versus current during a VI trace measured by the Cernox and PRT. Current ramp rate of 4 A/min

force generated acted to push the sample against the sample platform when the angle was set to 90°.

7.2.4 Variable Temperature Cold Head and 77 K Results

We now present the results of the $J_c(B, T, \theta)$ dependence measured in the Cold Head. As mentioned, the samples used in the Cold Head were 5 µm wide FIB samples. Because of their low I_c values, sample ohmic heating was not a concern. However, an important consistency check was to ensure the angular and field dependencies of the FIB samples were the same as the chemically etched tracks and full-width tapes in order to ensure the FIB tracks were able to correctly characterise a full-width tape. In the next section we present the angular and field dependencies of J_c for a chemically etched and FIB track

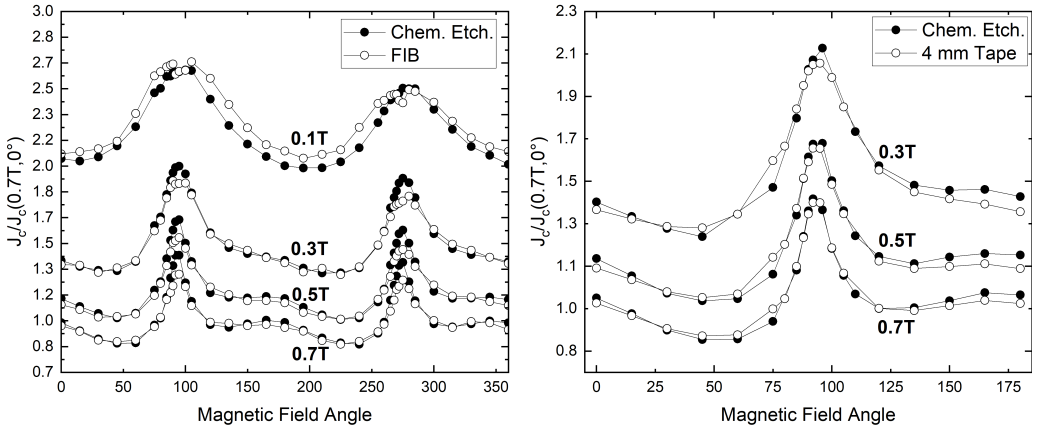

Figure 7.4: The J_c versus magnetic field angle to the tape normal of chem. etch. (3) and FIB (5) (left), and chem. etch. (3) and 4 mm wide tape (right). J_c values normalised to their values at 0.7 T and 0°.

along with a 4 mm wide tape made in liquid nitrogen and compare it with the Cold Head data.

$J_c(B, 77\,K, \theta)$ of Tracks

First, the experimental setup described in section 6.3 was used to measure $J_c(B, \theta)$ in liquid nitrogen for comparison of the track data. This setup allowed for a quick and easy comparison.

A new chemically etched (chem. etch. (3)) and FIB sample (FIB (5)) were made specifically to investigate the field and angular dependencies, and the $J_c(\theta)$ data for these samples at 0.7 T, 0.5 T, 0.3 T and 0.1 T are shown in Fig. 7.4. It can be seen that there is good agreement between the chemically etched and FIB track data as the curves at the four fields superpose well. The maxima at 90° and 270° are clearly seen for both samples which are due to the flux pinning between the CuO planes of the REBCO unit cell, and another very small maxima seen at fields of 0.7 T and 0.5 T and around 165° which is due to the pinning of the fluxons from the APCs in the REBCO

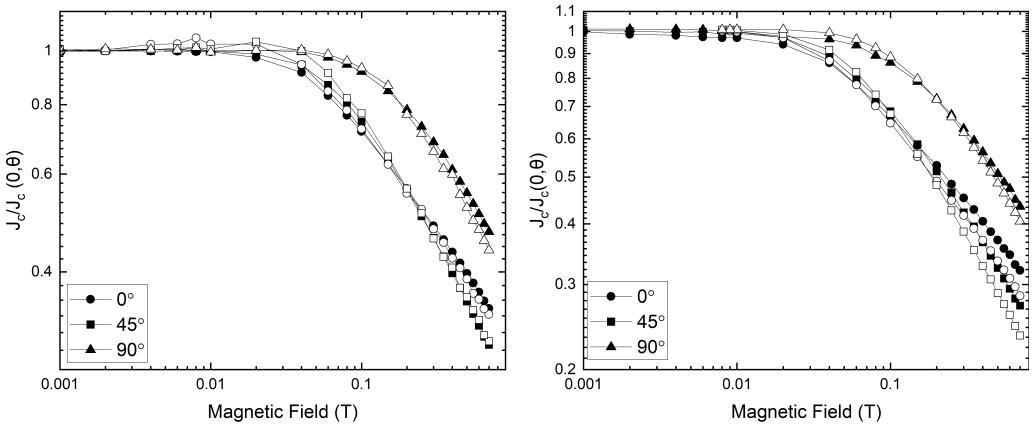

Figure 7.5: The J_c versus magnetic field for (solid symbols) chem. etch. (3) and (open symbols) FIB (5) (left), and for (solid symbols) chem. etch. (3) and a (open symbols) 4 mm wide tape (right). J_c values normalised to $J_c(0,\theta)$ at zero applied field.

layer. Fig. 7.4 also shows the comparison of the angular dependence for the chemically etched sample and the 4 mm wide tape measured at $E_c = 1000\,\mu\mathrm{Vm}^{-1}$ which also shows there to be good agreement.

Similarly, the $J_c(B)$ data for the chemically etched and FIB track, as well as for the chemically etched track and 4 mm wide tape at 0°, 45° and 90°, are shown in Fig. 7.5. There again appears to be a good agreement, except for the 4 mm wide tape which has a slightly higher sensitivity of J_c to field. Despite this, $J_c(B,\theta)$ appears to be consistent for both the chemically etched and FIB samples.

The corresponding n values versus angle and field for the chemically etched and FIB samples are shown in Fig. 7.6 and 7.7. The n values follow the same trend as J_c as shown also in Chapter 6.

Having shown the consistency between the chemically etched and FIB tracks in terms of the angular and field dependencies, we now present the angular and field work done using the Cold Head.

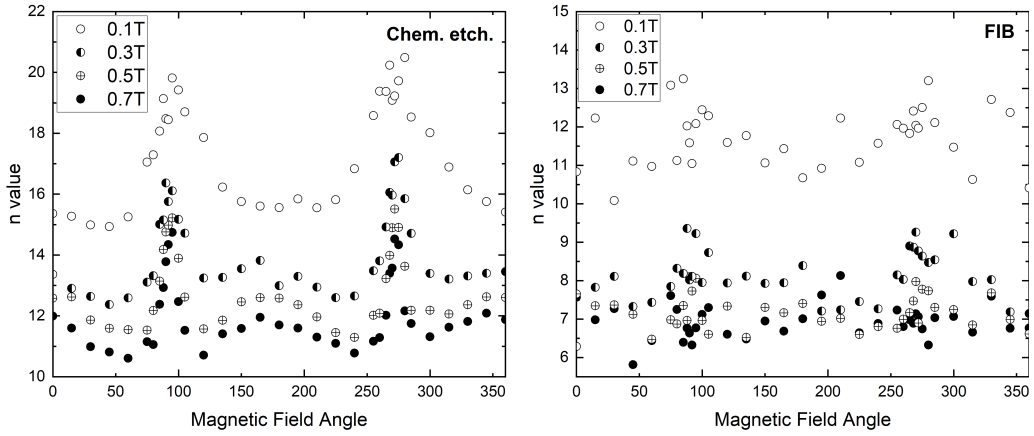

Figure 7.6: The n values versus magnetic field angle to the tape normal for a chemically etched track (left) and a FIB track (right).

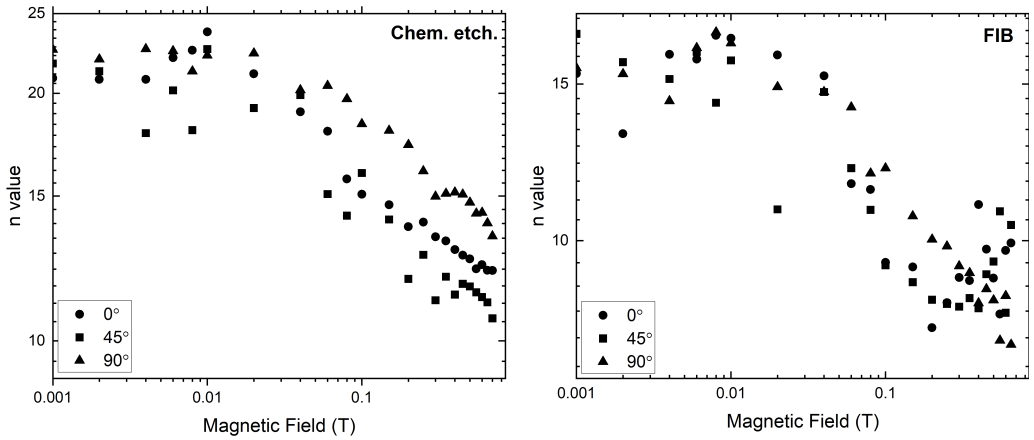

Figure 7.7: The n values versus magnetic field for a chemically etched track (left) and a FIB track (right).

Comparison Between the LN_2 Data the Cold Head Data

The new additions to the Cold Head enabling variable field and variable angle measurements were tested by comparing to $J_c(B, \theta)$ measurements made in liquid nitrogen.

Fig. 7.8 is a graph of J_c versus angle at 0.5 T and 0.3 T for a chemically

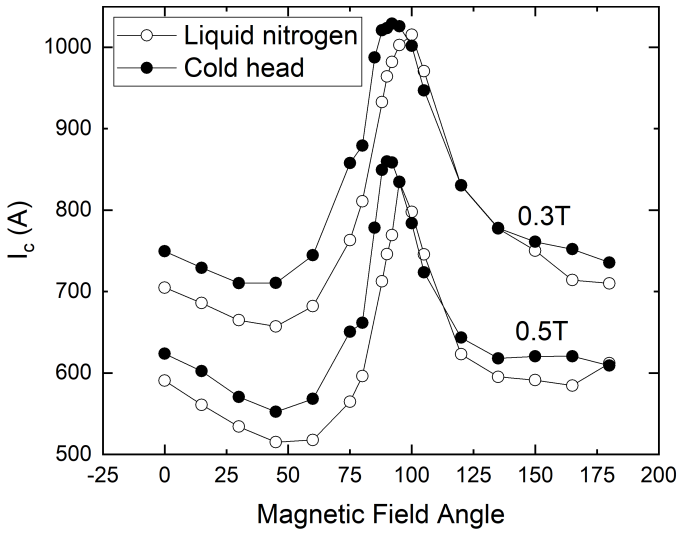

Figure 7.8: Comparison between the I_c angular dependence on a chemically etched sample measured in the Cold Head and in liquid nitrogen. Sample temperature was 77.0 K in the Cold Head and 77.3 K in liquid nitrogen.

etched sample measured using the Cold Head and the liquid nitrogen setup of Chapter 6. It can be seen that the two angular dependencies align reasonably well, and hence the new upgraded Cold Head system enabling $J_c(B, T, \theta)$ measurements was successful.

$J_c(B, T, \theta)$ of Tracks using the Cold Head

To measure $J_c(B, T, \theta)$ in the Cold head, a 5 µm wide FIB track was made referred to as FIB (CH). It was placed substrate side down with the track length aligned along the sample platform, such that the current direction was perpendicular to the magnetic fields for all angles of the field to the tape normal.

VI traces were made firstly at 0.5 T and 0.3 T at temperatures of 83 K, 77.347 K, 71 K, 65 K, 58 K, 50 K, 40 K, 30 K, 20 K and 10 K in that order As the currents at the lower temperatures were much higher (> 1 A at 10 K),

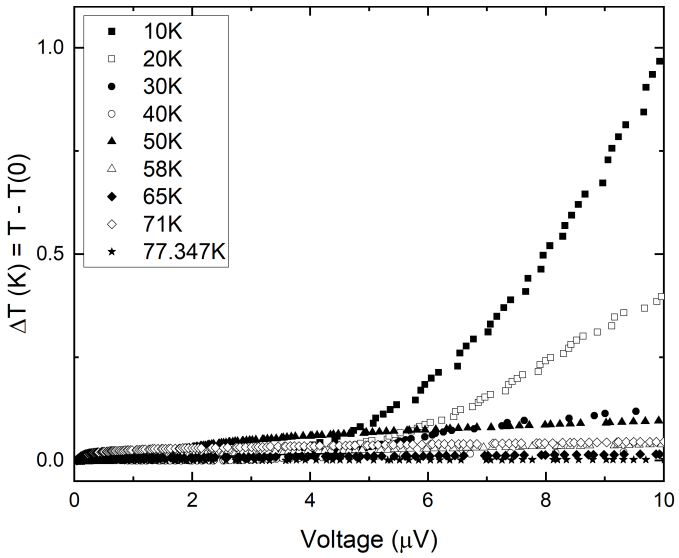

Figure 7.9: The increase in temperature measured by the Cernox versus the sample voltage during the VI traces for J_c measurements at each temperature.

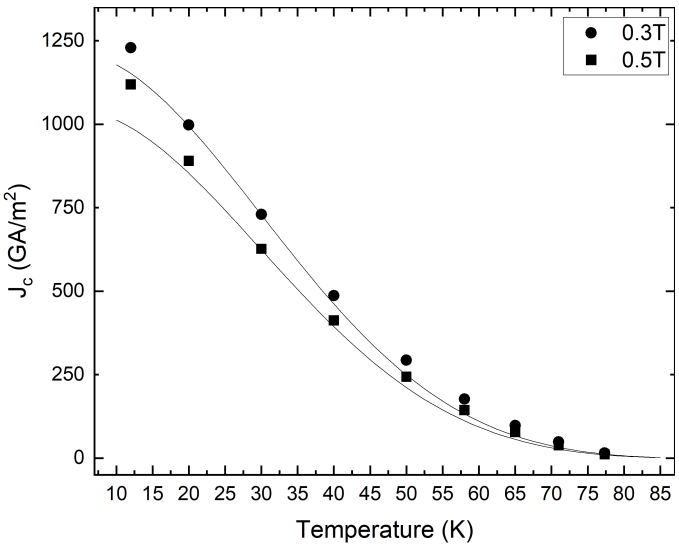

Figure 7.10: J_c versus temperature for a FIB sample measured in the Cold Head with fit to the JJ model (solid line).

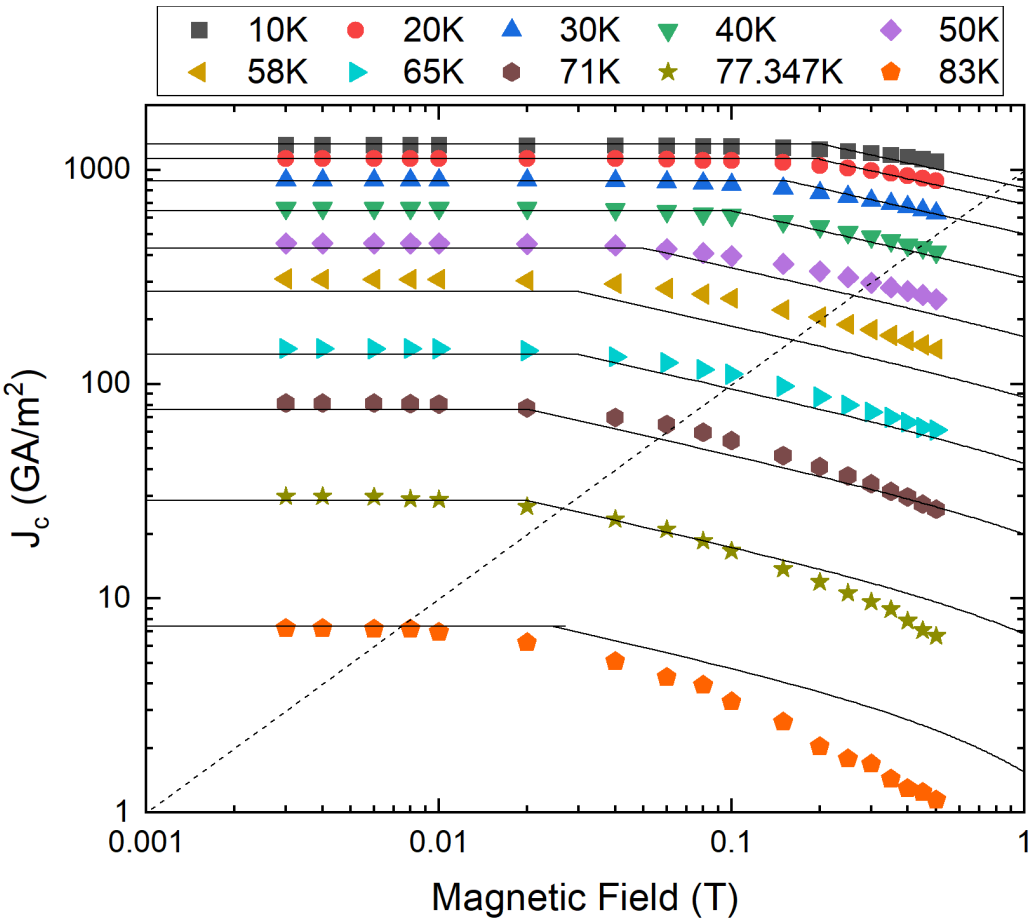

Figure 7.11: J_c versus magnetic field measured at different temperatures measured in the Cold Head with fit to the JJ model (solid lines) and a dashed line for the cross-over field.

there was more ohmic heating at 10 K and 20 K compared to the higher temperatures. Fig. 7.9 shows the increase in temperature versus sample voltage during each VI trace as measured by the Cernox, and although this temperature increase by 1 °C was a concern, it was unavoidable since the current of the 5 µm tracks was above 1 A at this temperature, but to make the tracks any narrower than 5 µm would result in a track of REBCO that would likely degrade very easily.

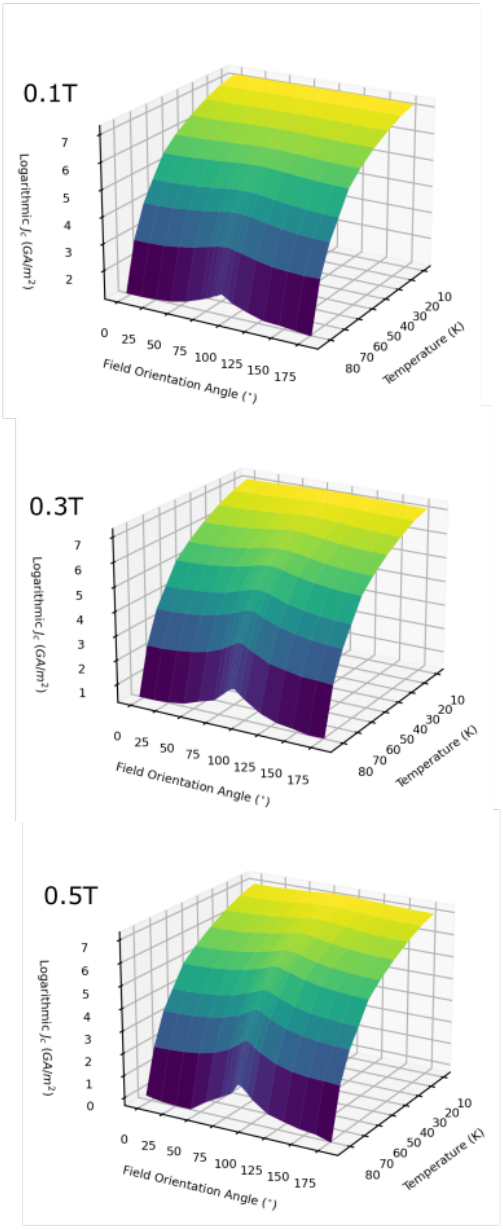

Figure 7.12: The $J_c(T, \theta)$ surface measured on a FIB track in the Cold Head at 0.1 T, 0.3 T and 0.5 T.

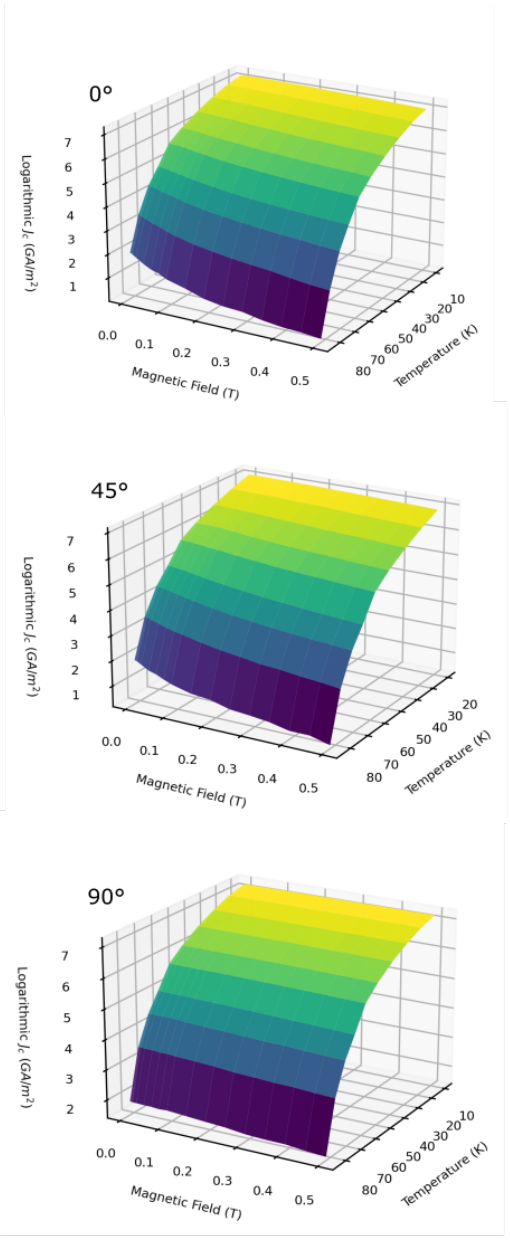

Figure 7.13: The $J_c(B, T)$ surface measured on a FIB track in the Cold Head at 0°, 45° and 90°.

After measuring the temperature dependence of J_c, which is shown in Fig. 7.10 at the two fields of 0.5 T and 0.3 T. The full set of angular and field dependencies were subsequently measured at temperatures between 10 K and 83 K. An angular sweep involved measuring J_c at angles between 0° and 180° in 15° increments, and 2° increments around the peak in J_c. A field sweep involved taking measurements of I_c in logarithmic increments of the field, i.e. at fields between 0.7 T to 0.1 T in 0.05 T increments, then at fields between 0.1 T and 0.01 T in 0.02 T increments, and finally 0.01 T to 0 T in 0.002 T increments.

Fig. 7.11 shows J_c versus field at all temperatures with fits to the JJ model using the fitting parameter values presented section 7.2.5. The dashed line in Fig. 7.11 represents the cross-over fields (B_{cr}) which separates the plateau region where J_c is independent of field from the region where J_c depends linearly on field in log space. The expression for B_{cr} presented in [120] is given by

$$B_{cr} = \frac{\mu_0 J_c(B_{app} < B_{cr})t}{2} \tag{7.1}$$

where t is the thickness of the REBCO layer, where we have used the value of 1.6 µm given to us by the manufacturer of this specific REBCO tape used [89]. Equation 7.1 with this value of t used does not produce B_{cr} values that match those from Fig. 7.11 at the lower temperatures, and at higher temperatures B_{cr} appears to be independent of temperature also shown in Fig. 7.11, and this therefore calls for a deeper understanding of the dependence of B_{cr} on J_c.

The full $J_c(\theta, T)$ surfaces at fields of 0.1 T, 0.3 T, 0.5 T are shown in Fig. 7.12. Similarly, the $J_c(B, T)$ surfaces at angles of 0°, 45° and 90° are shown in Fig. 7.13, and these graphs prove the viability of using narrow tracks to easily obtain a full set of $J_c(B, T, \theta)$ data.

7.2.5 Fits to the SNS Josephson Model

Using the $J_c(B,\varepsilon)$ data presented in Chapter 6, and the $J_c(B,T,\theta)$ data presented in this Chapter, we now use the SNS JJ model [119] presented in 3.4.4 to find a global fit to the data sets.

Table 7.1: Parameters extracted from fits of the strain data to the JJ model.

Fit parameters	4 mm tape	Chem. etch. (1)	Chem. etch. (2)	FIB (1)	FIB (2)	FIB (3)	FIB (4)	FIB (CH)
c_1	0.304	0.312	0.309	0.294	0.325	0.307	0.317	0.30
$c_{\varepsilon 1}$ ($10^{-3}\%^{-1}$)	-2.74	-1.86	-0.13	-18.04	-20.17	-9.78	-8.70	-
$c_{\varepsilon 2}$ ($10^{-3}\%^{-2}$)	30.57	34.40	26.39	47.40	22.14	37.93	41.80	-
ζ_1 (nm)	63.12	51.86	50.45	25.02	4.16	3.12	42.10	45
ζ_2 (nm)	-52.65	-41.07	-39.16	-8.76	14.45	16.48	-30.06	27

We begin by fitting the $J_c(B,\varepsilon)$ data of each of the samples listed in Table 6.1 to the model. In these fits, we set the following parameters as fixed, with $T_c^*(0) = 91\,\mathrm{K}$, $B_{c2}^*(0,0) = 103\,\mathrm{T}$, $w_s(0) = 244\,\mathrm{nm}$, $\lambda_L(0,0) = 135\,\mathrm{nm}$, $d(0) = 0.4\,\mathrm{nm}$, $\nu = 0.61$, $w = 2.2$, $\tilde{\alpha}_n(0,0) = -0.255$, $\tilde{\beta}_n(0,0) = 1.3$, $\tilde{m}_n = 0.659$, $T_{c,n}^*(0) = -2670\,\mathrm{K}$ using values that had been measured and determined for REBCO APC tape following the same procedure as [119]. The remaining parameters were left as free fitting parameters: c_1, $c_{\varepsilon 1}$, $c_{\varepsilon 2}$, ζ_1, ζ_2, where c_1 describes the field dependence of J_c, $c_{\varepsilon 1}$ and $c_{\varepsilon 2}$ are constants that describe the strain dependence of the junction thickness (d) and ζ_1 and ζ_2 are constants that describe the strain dependence of the junction width (w_s).

Due to the hysteresis of the strain curves for the FIB samples, only the half-cycle from maximum compression to maximum tension was used in the analysis.

Table 7.1 gives the values of the parameters found from the fit. The fitting parameters extracted for the chemically etched tracks and the 4 mm tape were very similar as expected due to the good superposition of their strain

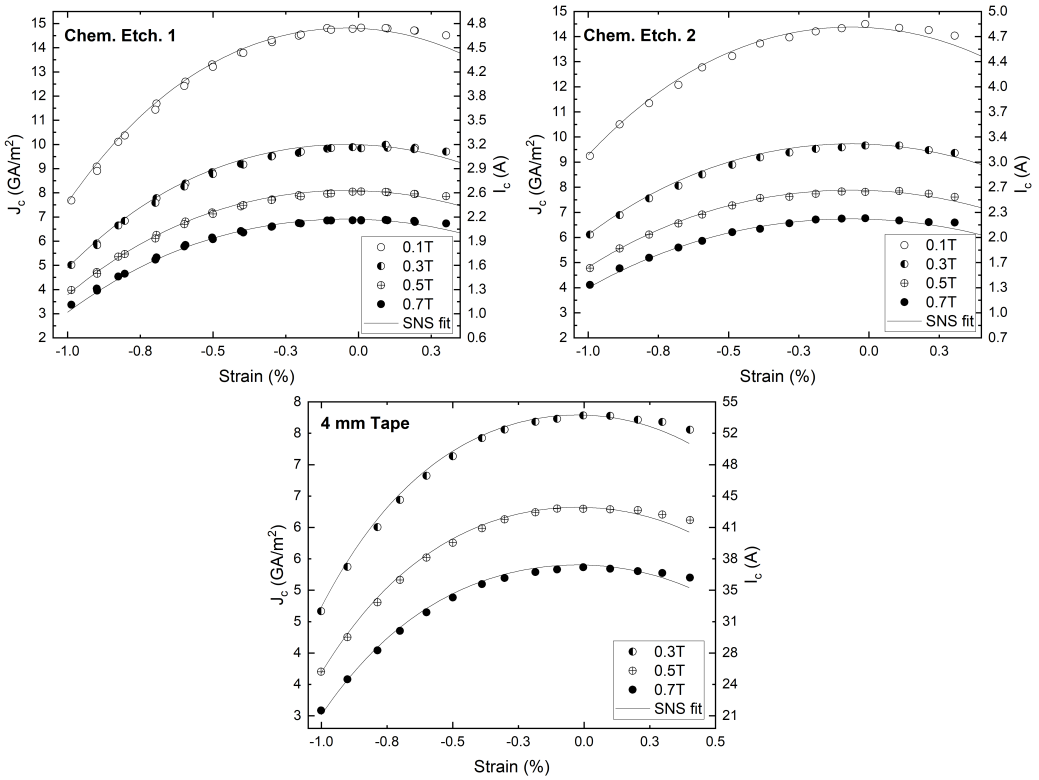

Figure 7.14: J_c versus ε for the chemically etched tracks with fits to the JJ model.

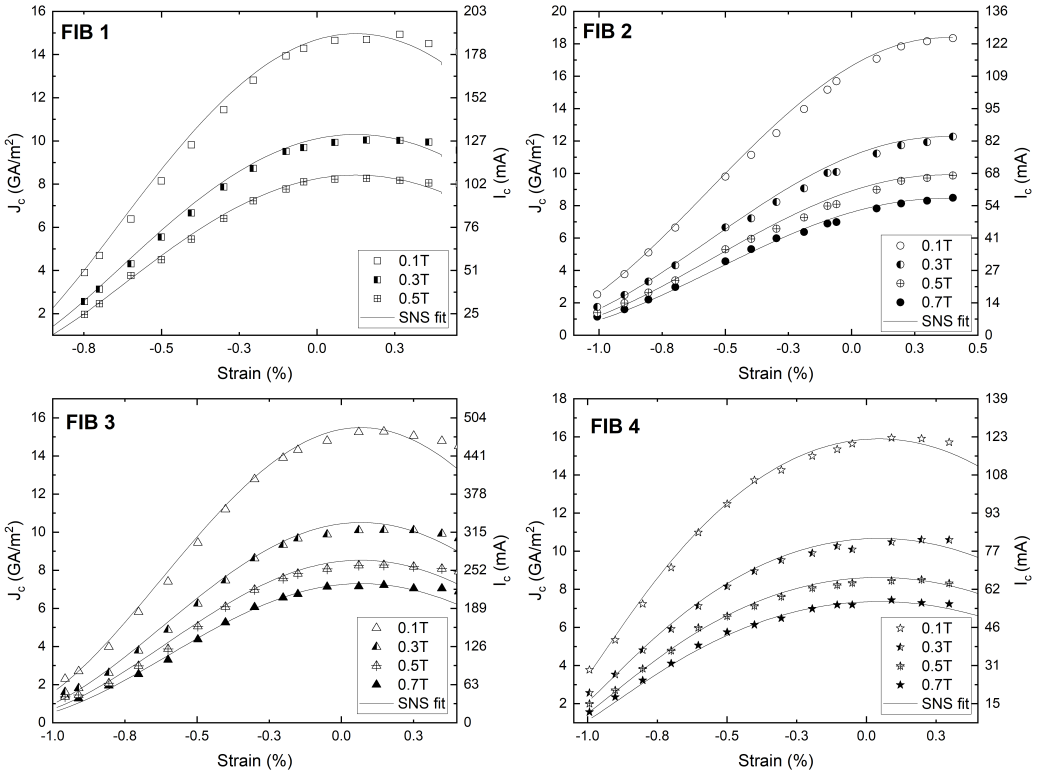

Figure 7.15: J_c versus ε for the FIB tracks with fits to the JJ model.

curves. In addition, all samples had a similar value for c_1 of around 0.3, indicating a similar magnetic field dependence, and also similar values of $c_{\varepsilon 2}$, however the FIB samples generally had higher values of $c_{\varepsilon 1}$ by an order of magnitude. The values of ζ_1 and ζ_2 were more varied across both the FIB and chemically etched samples over an order of magnitude, with ζ_2 being either positive or negative.

The $J_c(B, \varepsilon)$ data with these JJ fits of the chemically etched tracks and the 4 mm wide tape are shown in Fig. 7.14, and the FIB tracks shown in Fig. 7.15. The model fits all datasets very well.

To fit the model to the $J_c(B, T)$ Cold Head data measured on sample FIB (CH), we removed $c_{\varepsilon 1}$ and $c_{\varepsilon 2}$ from the fit as there was no strain applied and hence no strain dependence. We found c_1=0.3, ζ_1=45 nm and ζ_2=27 nm to give the best fit to the data which are consistent with the values found for the other samples, and therefore this model with these fitting parameters was successfully able to model the $J_c(B, T, \varepsilon)$ data sets for this REBCO CC.

7.3 Expt. 2: $J_c(\varepsilon)$ Curves for Different Strain and Current Orientations

The motivation of this small experimental investigation was to exploit the range of the many new experiments that track samples enable. More explicitly, here we present measurements that address whether if ε is applied in the direction along the width of the tape and the current still flows along its length, does the f value found from the chain model remain the same as that found when ε is applied parallel to the tape length.

Measurements of the strain curves were made on two sets of samples for each of four different combinations of ε and current direction. Table 7.2 shows a list of all the samples tested and their corresponding widths, and a picture

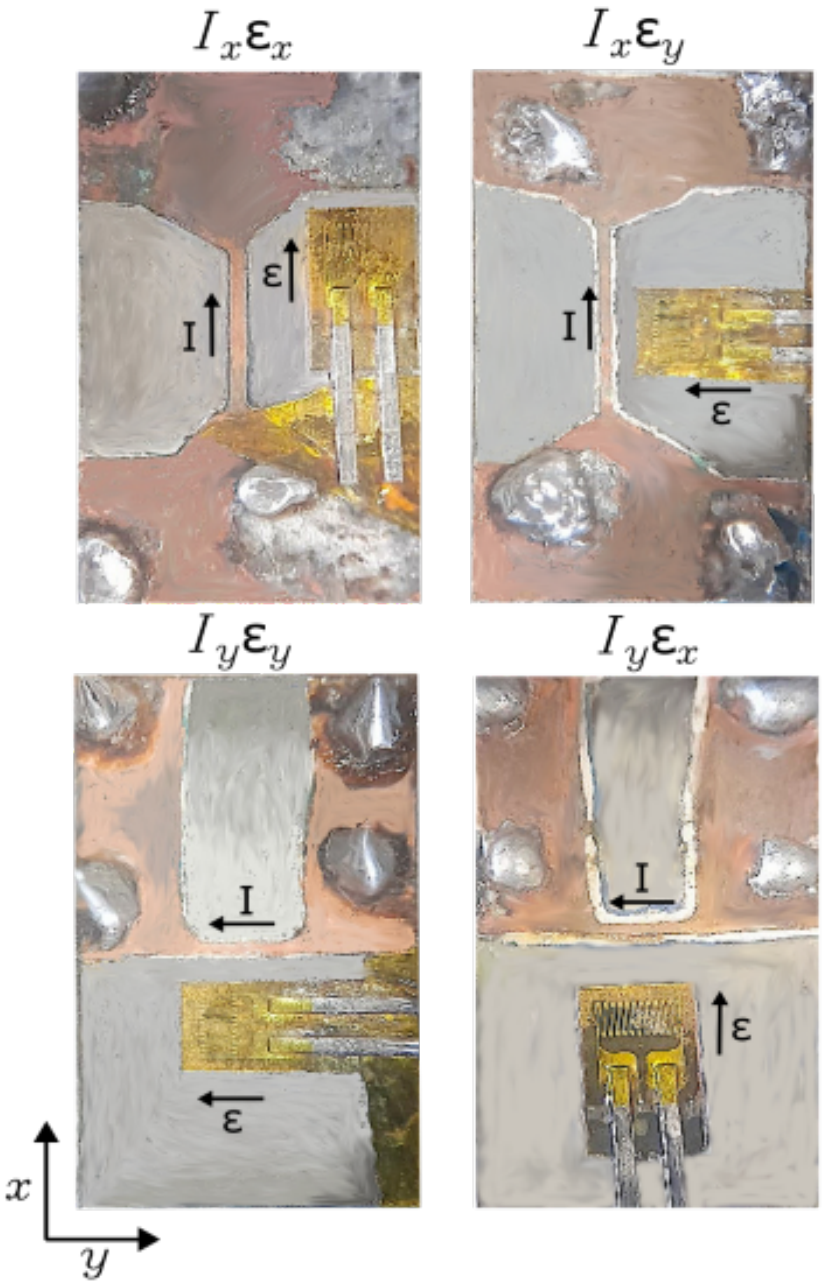

Figure 7.16: The setup for the different orientations of current and strain within the REBCO tape.

of the sample set with their different combinations of current and ε direction are shown in Fig. 7.16. The notation $I_i\varepsilon_j$ was used to represent the direction of the current and ε respectively, where i and j can be x or y, with x along the length of the tape and y along the width of the tape. The tracks with I_y were etched differently such that the tracks pointed in the y direction, and strain gauges were placed in the correct orientation parallel to the applied ε.

Table 7.2: The samples on which strain curves were measured for each $I_i\varepsilon_j$ combination.

Sample	Width /μm	I_c at self field /A
Chem. etch. $I_x\varepsilon_x$ 1	212	2.71
Chem. etch. $I_x\varepsilon_y$ 1	220	3.17
Chem. etch. $I_y\varepsilon_x$ 1	360	4
Chem. etch. $I_y\varepsilon_y$ 1	160	2.96
Chem. etch. $I_x\varepsilon_x$ 2	225	2.57
Chem. etch. $I_x\varepsilon_y$ 2	248	3.39
Chem. etch. $I_y\varepsilon_x$ 2	330	4.25
Chem. etch. $I_y\varepsilon_y$ 2	290	3.51
FIB 1 ($I_x\varepsilon_x$, $I_x\varepsilon_y$)	5	0.13
FIB 2 ($I_y\varepsilon_y$, $I_y\varepsilon_x$)	5	0.19

The experiment was also done on two FIB samples, where the $I_x\varepsilon_x$ and $I_x\varepsilon_y$ curves, as well as the $I_y\varepsilon_y$ and $I_y\varepsilon_x$ curves, were each measured on the same sample by rotating it by 90° and resoldering it to the strain board. This was done because the f values were very specific for each FIB sample, and so it was important to investigate the ε_x and ε_y characteristics on one sample. The success rate of this was small however due to the fragile nature of the FIB tracks, so only one set of measurements were taken with no repeats. For these FIB samples the Poisson strain was used to approximate the strain in the orthogonal direction, as a biaxial strain gauge was too big to fit on the substrate.

It was expected that, for the chemically etched samples, the $I_x\varepsilon_x$ curve would

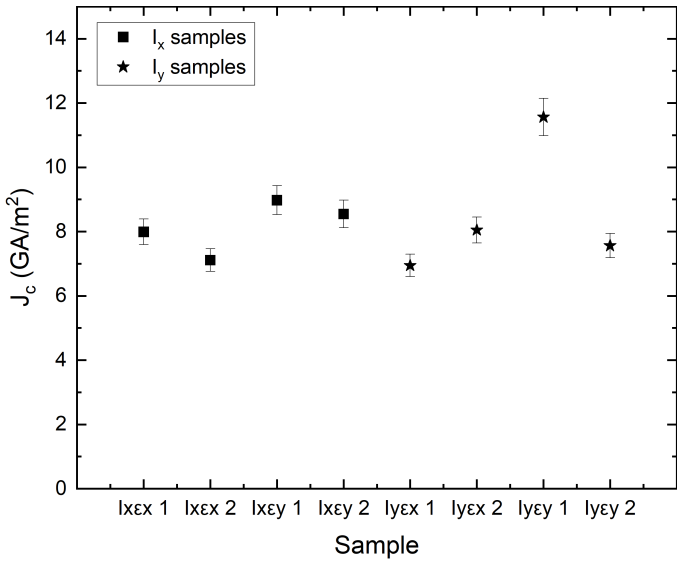

Figure 7.17: J_c measurements at 0.5 T, 77 K and 0 % strain on all samples (using the $I_i\varepsilon_j$ notation for sample labelling) with current in the x and y directions.

be identical to the $I_y\varepsilon_y$ curve. This is because of the volume fraction of 50 % of each domain calculated for the tape, such that the tape is homogeneous in both directions. The behaviour of the samples where the current and strain were orthogonal was harder to predict, as little work like this has been done previously and cannot be predicted by the chain model.

For the FIB samples, it was expected that the $I_x\varepsilon_y$ sample would have an opposite gradient to the $I_x\varepsilon_x$ curves due to the application of ε now primarily across B-domains along the y direction, since all $I_x\varepsilon_x$ FIB curves shown in the previous chapter were demonstrated to be richer in A domains along the x direction.

As almost all previous work has done transport current measurements by sending current along the length of the tape, it was important to find out whether sending current along the tape width instead changes J_c. The results of this are shown in Fig. 7.17, which presents the J_c values for each track

tested on free samples at 0.5 T, and shows that there is no difference in J_c between I_x and I_y tracks, in agreement with the findings of [118] that also found an independence of J_c to the direction of current in the tapes at zero strain.

Having checked the consistency in J_c for REBCO CC with current sent in the x and y directions, we now present the results of $I_x\varepsilon_x$, $I_x\varepsilon_y$, $I_y\varepsilon_x$, $I_y\varepsilon_y$ for the two sets of samples. However as ε was being considered in two orthogonal directions, it was important to take into account the transverse strain due to the Poisson ratio of the strain board, which would generate an inherent y-strain even though the applied ε was in the x direction. To measure this we could have used a biaxial strain gauge on each sample, however the size of the 7 mm by 4 mm biaxial strain gauges available were too big to fit on the small area of exposed substrate, so we were forced to instead use small 3 mm long linear strain gauges. A measurement of the Poisson ratio was made for this specific strain board and is presented below.

7.3.1 Poisson Ratio of Strain Board

To measure the Poisson ratio of the strain board, a biaxial strain gauge was adhered to a proxy REBCO substrate soldered to the strain board. The x and y strains were measured for a strain cycle with ε applied in the x direction. Fig. 7.18 presents the measured transverse ε_{trans} against the applied strain $\varepsilon_{applied}$ for the strain cycle in liquid nitrogen at 77 K. There is a small amount of hysteresis on applying and releasing the applied strain most likely due to some plastic deformation of the strain board. The Poisson ratio, given by $\nu = -\frac{\varepsilon_{trans}}{\varepsilon_{axial}}$, was measured to be 0.087 on applying compressive ε and 0.081 on releasing ε found from a linear fit to the data.

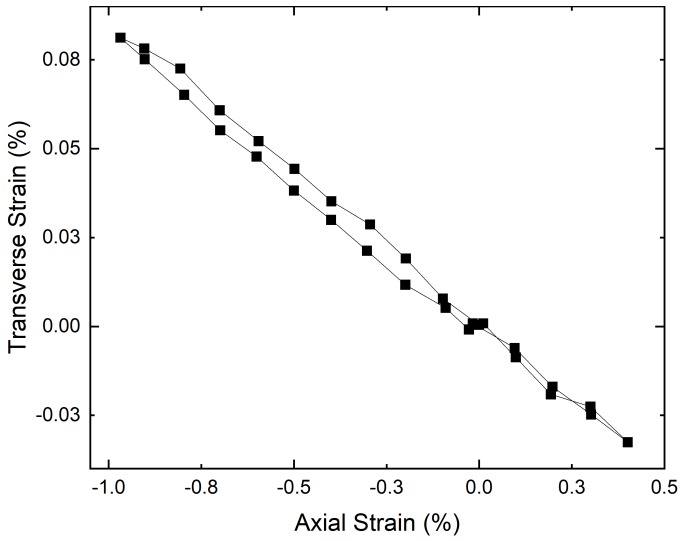

Figure 7.18: Axial strain versus transverse strain for the strain board at 77 K. Poisson ratio (ν) is given by the negative of the gradient and measured as 0.087.

7.3.2 J_c for Chemically Etched Tracks

The raw strain curves for each sample (set 1), and the repeat set (set 2) are shown in Figs. 7.19 and 7.20 respectively. Each curve is inverse parabolic, with each curve having a slightly different offset in $J_{c,peak}$. The ε_m for all the samples is given in Table 7.3. These ε_m values are larger in magnitude and in the compressive region for curves where the current and ε are orthogonal. The cause for these large offsets is again attributed to a thermal pre-strain.

To compare all the samples, the curves were shifted such that $J_{c,peak}$ aligned with 0 % strain. Fig. 7.21 presents a superposition of each strain curve from set 1 and 2 to check for repeatability. There is good agreement between the two sets of curves except for $I_y\varepsilon_y$, where the strain curves do not superpose so well, which could be due to some delamination of one of the samples or an incorrect adhering of the SG.

After checking for reproducibility, the curves for the four different current

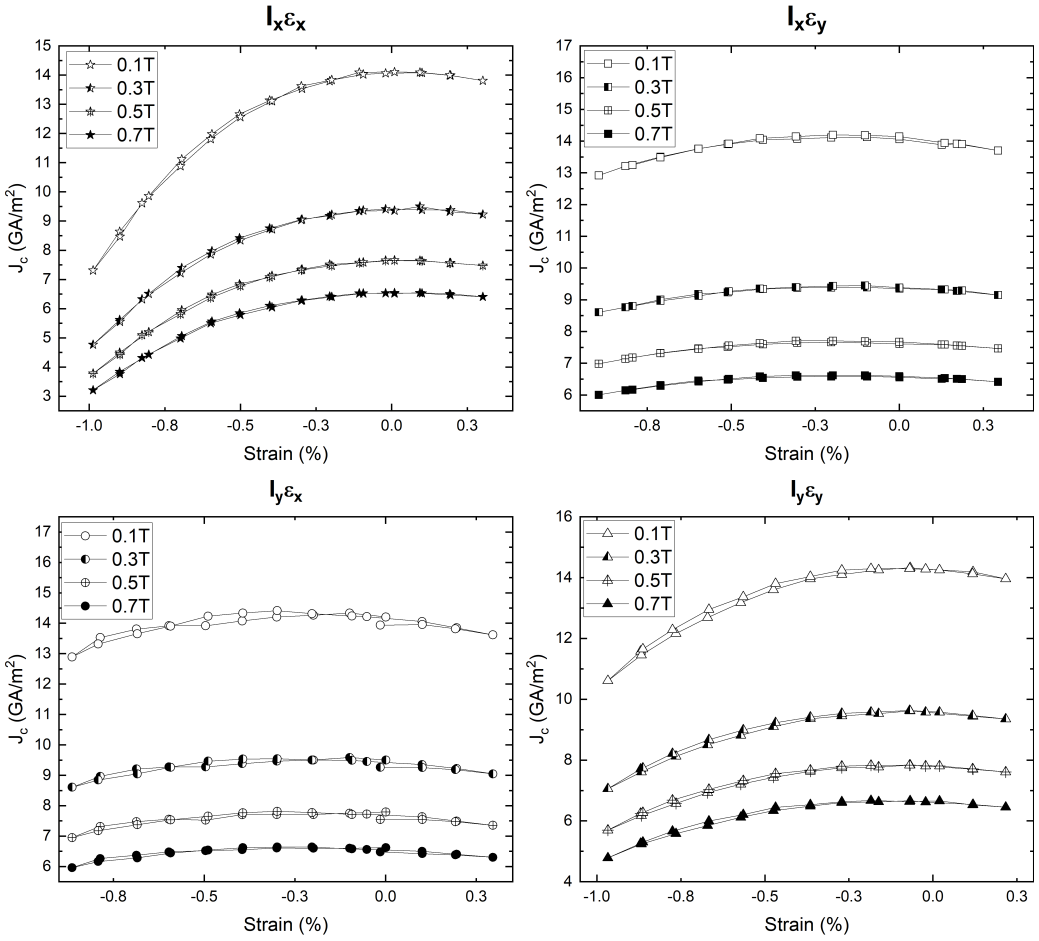

Figure 7.19: The raw J_c versus ε curves for each $I_i\varepsilon_j$ combination for the first set of samples (set 1).

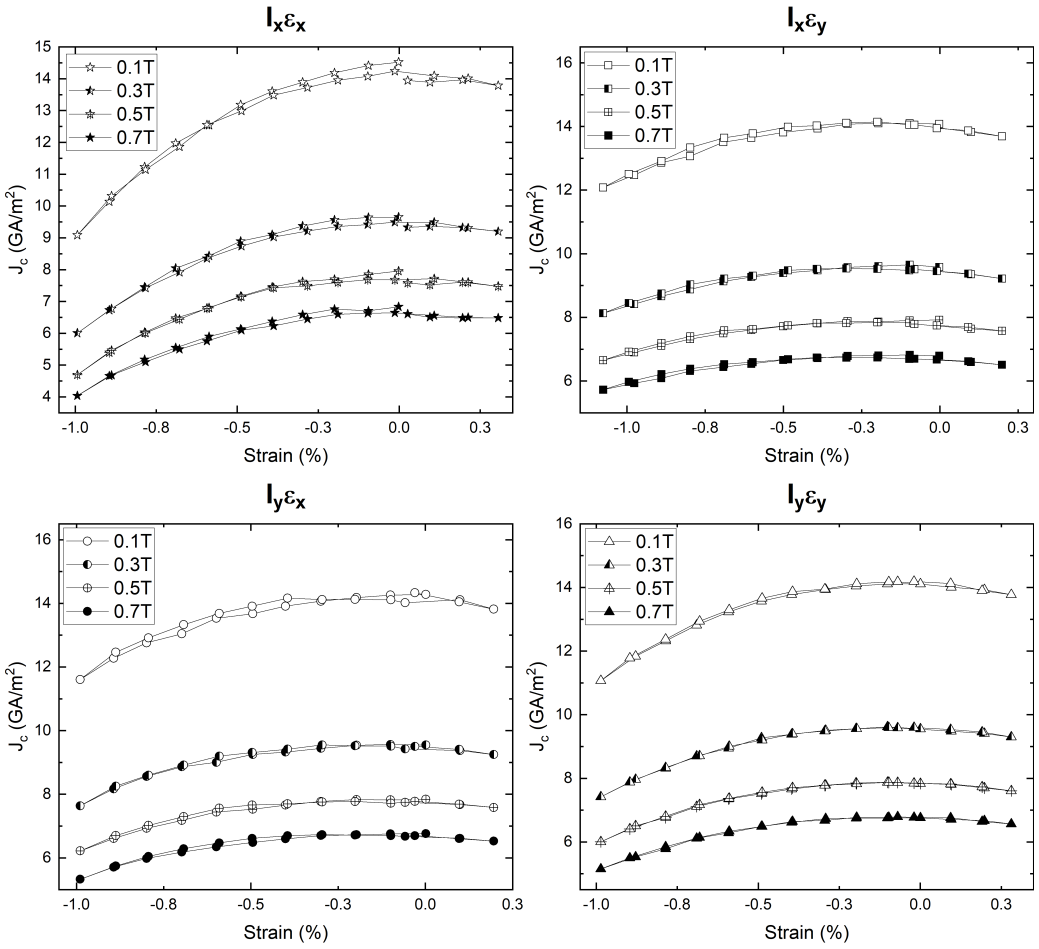

Figure 7.20: The raw J_c versus ε curves for each $I_i\varepsilon_j$ combination for the repeat set of samples (set 2).

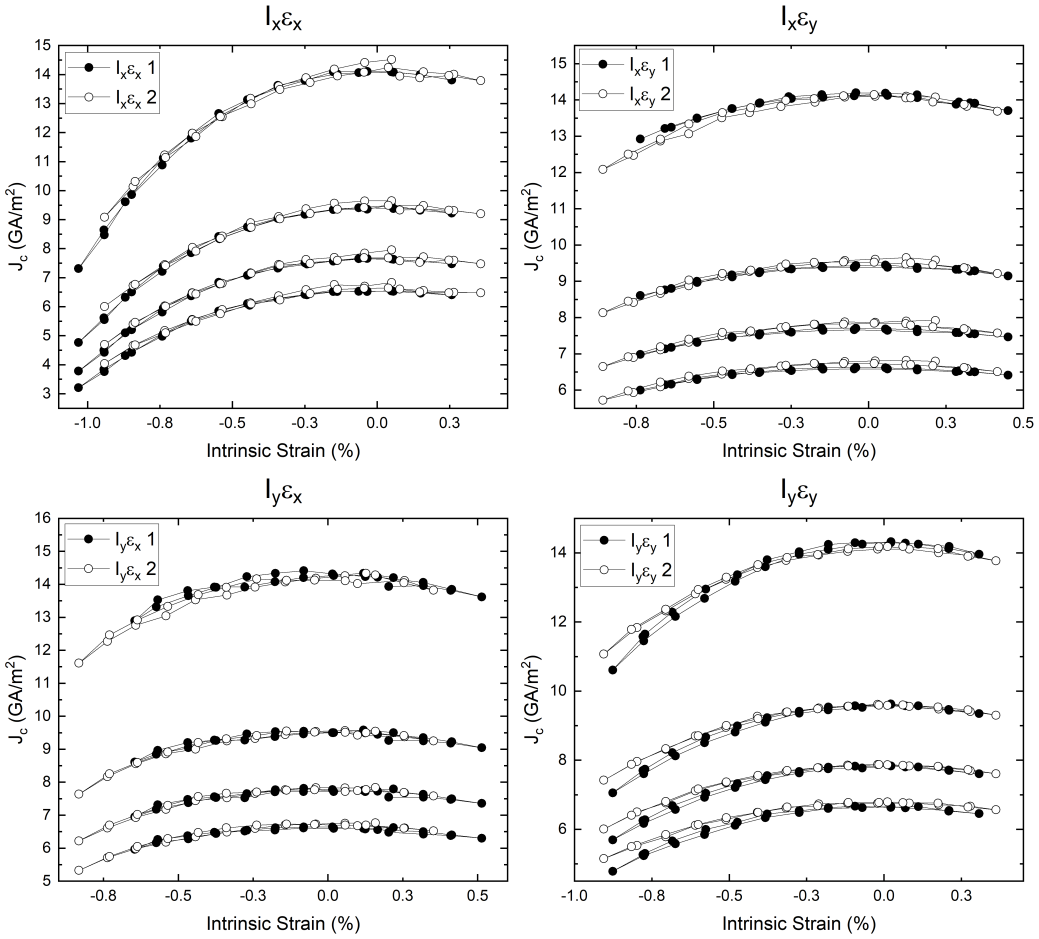

Figure 7.21: Superposition of strain curves from set 1 and set 2 of samples for each $I_i\varepsilon_j$ combination.

Table 7.3: Strains at which $J_{c,peak}$ occurred in the J_c versus ε curves for each sample.

Sample	ε_m (%)
$I_x\varepsilon_x$ 1	0.04
$I_x\varepsilon_y$ 1	-0.16
$I_y\varepsilon_x$ 1	-0.22
$I_y\varepsilon_y$ 1	-0.09
$I_x\varepsilon_x$ 2	-0.04
$I_x\varepsilon_y$ 2	-0.22
$I_y\varepsilon_x$ 2	-0.16
$I_y\varepsilon_y$ 2	-0.08

and ε orientations were compared. Fig. 7.22 shows a superposition of the curves for set 1 and set 2 at at all fields. The solid lines in the figures are fits of the data to the JJ model to aid the comparison.

Fig. 7.22 shows that J_c is the most sensitive to ε for the $I_x\varepsilon_x$ curve, and the least sensitive for $I_x\varepsilon_y$ for both sets of samples. The $I_y\varepsilon_y$ and $I_y\varepsilon_x$ curves lie between $I_x\varepsilon_x$. This results implies that there is some anisotropy in the x and y directions of the tape as the $I_x\varepsilon_x$ and $I_y\varepsilon_y$ curves do not superpose, this could be due to a slightly different domain fraction from the expected 50 %. To investigate this, both sets of $I_x\varepsilon_x$ and $I_y\varepsilon_y$ curves were fitted to both versions 1 and 2 of the chain model to find the f values. Table 7.4 and 7.5 gives the results of the fits, where in fit 2 we have set g_1, g_2 and ε_{peak} as fixed parameters to allow for a better comparison of the f values. The fitting shows that the f values of the $I_y\varepsilon_y$ curves are 0.46 and 0.47 for fit 1, and 0.46 and 0.42 for fit 2 (below 0.5), and the $I_x\varepsilon_x$ curves are 0.51 and 0.5 for fit 1, and 0.55 and 0.51 for fit 2 (above 0.5), suggesting there is some anisotropy in the tapes, consistent with the EBSD results.

Furthermore, J_c is less sensitive to ε when the current and ε are orthogonal compared to when the current and strain are aligned, suggesting that the J_c

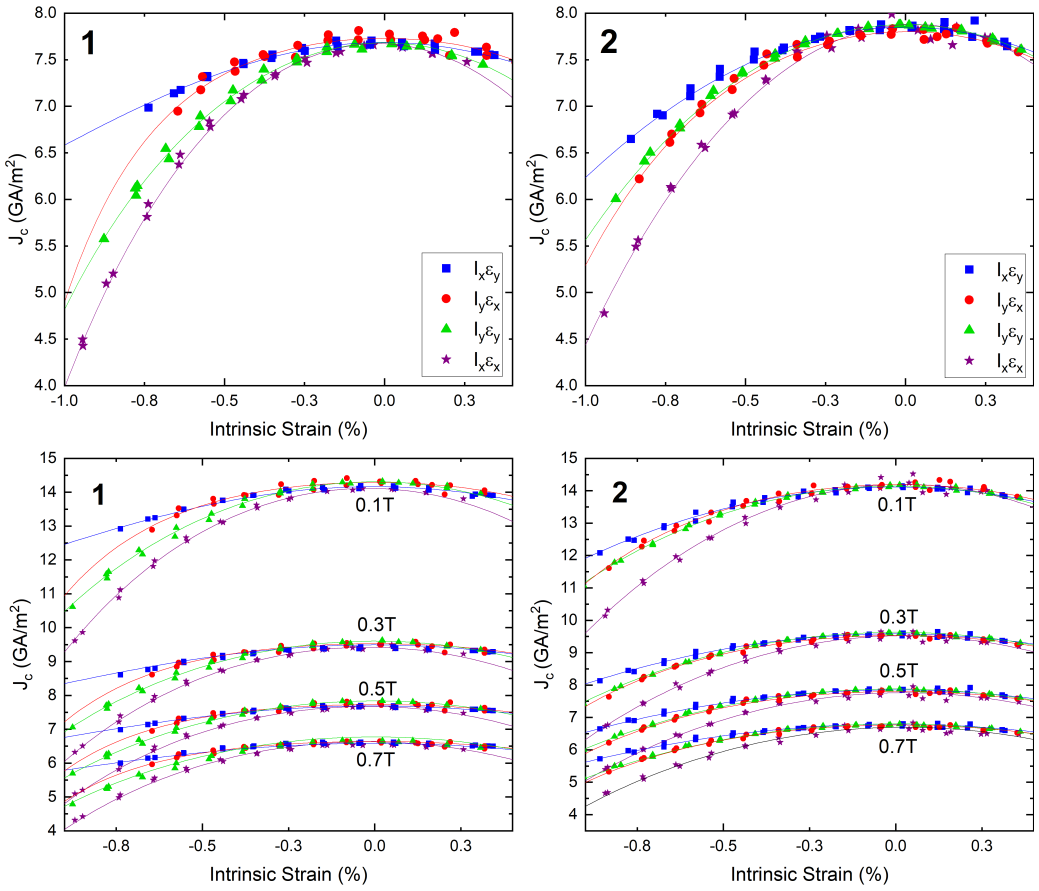

Figure 7.22: All four $I_i\varepsilon_j$ strain curves for set 1 (left) and set 2 (right) at 0.5 T (top) and at all fields (bottom).

sensitivity to strain depends on the direction of the current relative to ε. The field dependence however is the same for all current orientations, as shown by Fig. 7.22, where the $J_c(0)$ values for each curve are the same at each field.

Table 7.4: Fit parameters values extracted from the bimodal chain model fit 1 for $I_x\varepsilon_x$ and $I_y\varepsilon_y$ strain curves at 0.5 T.

	$I_x\varepsilon_x$ 1	$I_x\varepsilon_x$ 2	$I_y\varepsilon_y$ 1	$I_y\varepsilon_y$ 2
$J_c(0)$ (GA/m^2)	8.06 ± 0.01	7.86 ± 0.02	7.81 ± 0.01	7.85 ± 0.01
f	0.511 ± 0.005	0.498 ± 0.005	0.456 ± 0.011	0.468 ± 0.004
$\frac{dT_c^*}{d\varepsilon}$ (K/%)	5.79 ± 0.14	5.50 ± 0.27	4.74 ± 0.47	4.77 ± 0.27
g (/%)	0.84 ± 0.02	0.79 ± 0.04	0.68 ± 0.07	0.69 ± 0.04

Table 7.5: Fit parameters values extracted from the bimodal chain model fit 2 for $I_x\varepsilon_x$ and $I_y\varepsilon_y$ strain curves at 0.5 T. Fixed parameters are $g_A = 0.4$, $g_B = 0.2$, $\varepsilon_{peak} = 0.25\%$.

	$I_x\varepsilon_x$ 1	$I_x\varepsilon_x$ 2	$I_y\varepsilon_y$ 1	$I_y\varepsilon_y$ 2
$J_c(0)$ (GA/m^2)	7.63 ± 0.04	7.68 ± 0.017	7.81 ± 0.02	7.83 ± 0.01
f	0.55 ± 0.016	0.52 ± 0.016	0.46 ± 0.017	0.42 ± 0.008

7.3.3 J_c for FIB Tracks

The same investigation was carried out on two FIB tracks. $I_x\varepsilon_x$ and $I_x\varepsilon_y$ were measured on one sample by rotating through 90° and re-soldering the sample to the strain board, and similarly $I_y\varepsilon_y$ and $I_y\varepsilon_x$ were carried out on another sample. Fig. 7.23 shows the four strain data sets acquired. As expected, the $I_x\varepsilon_x$ results showed a high sensitivity of J_c to ε under compressive strain with a $J_{c,peak}$ shift to the tensile region as seen before, suggesting a large f value of the track.

After rotating the sample through 90°, re-soldering, and then collecting the $I_x\varepsilon_y$ data, there appeared to be no dependence of J_c on ε, although for

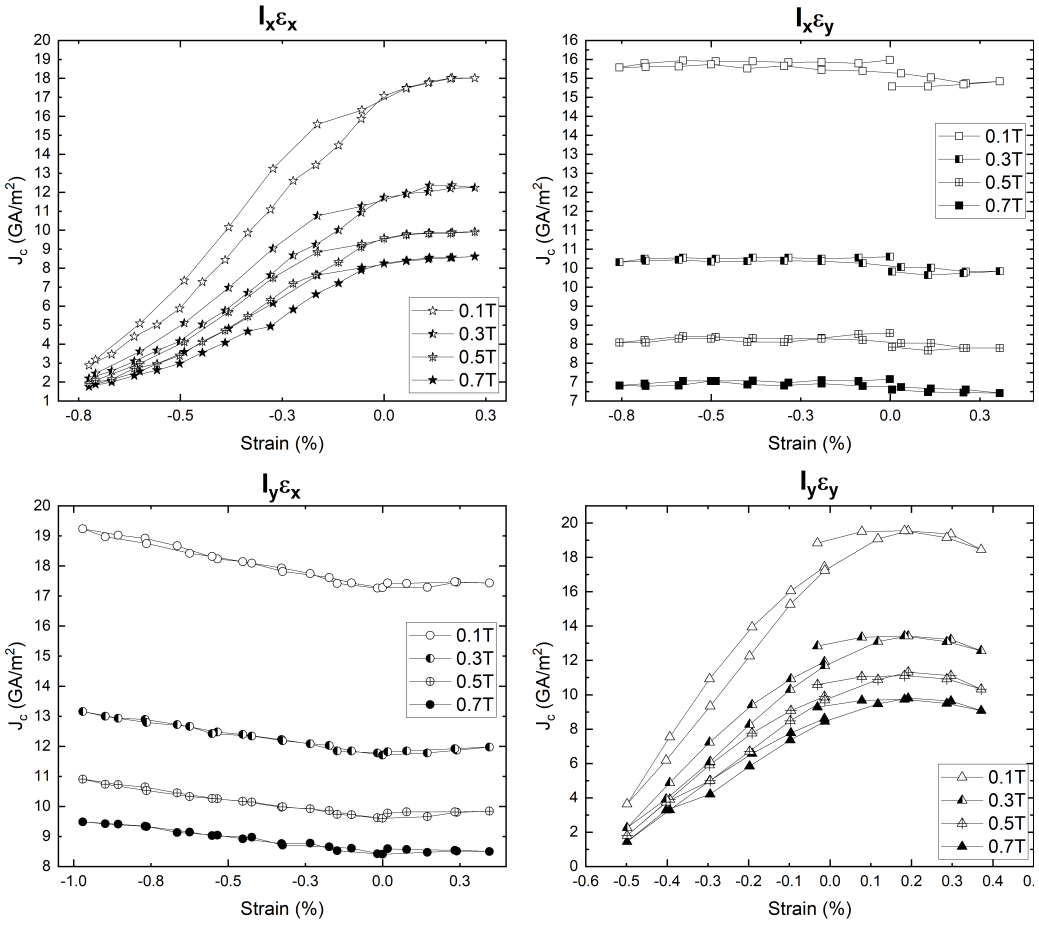

Figure 7.23: The raw J_c versus ε curves for each $I_i\varepsilon_j$ combination for the FIB samples.

the chemically etched samples, an inverse parabolic dependence was found despite it being weak. This could be due to several reasons, the most obvious one being the strain not propagating across the very narrow 5 µm wide track due to its small area and hence weak bonding to the substrate. Assuming this is not the case and that there are no experimental artifacts, the other reason could be because the ε is now propagating across a B domain rich area, but here we would expect the gradient of J_c versus ε to be linear and negative as shown in Fig. 3.12 and not independent of ε.

On the next sample $I_y\varepsilon_y$ was measured, and a similar J_c dependence on ε was found as the $I_x\varepsilon_x$ curve, with a high sensitivity of J_c to compressive strain, and a shift in $J_{c,peak}$ to the tensile region. This is suggestive of a large fraction of A domains now aligned along the y direction of the tape, or along the track length. This results provides further evidence towards the process of FIB milling itself changing the domain structure of the REBCO, but in a specific way such that the A domains are being forced to align along the length of the track (which could be in the x or y direction). In other words, the precise detwinning outcome, or the direction in which the A and B domains are forced to align, relies on the direction of the FIB milling.

On rotating the sample and measuring $I_y\varepsilon_x$, it was found that J_c increased linearly while applying compressive strain, consistent with the results found from the application of ε across a detwinned, B domain area of REBCO [114]. This result therefore provides strong evidence that the FIB milling is causing a detwinning of the REBCO, causing the A domains to align along the FIB track length and B domains to align along the track width.

7.4 Conclusion

In this chapter, we presented results from two experiments. First, we presented the results of the $J_c(B, T, \theta)$ dependence measured on a FIB track

using the Cold Head. We presented an overview of the setup and the upgrades to the Cold Head to enable in field and variable angle measurements with a precise control of temperature. We then presented the results of the angular and field dependence of a chemically etched and FIB samples as measured in liquid nitrogen and confirmed that the dependencies were the same and representative of a full-width REBCO CC. Finally we presented the full set of $J_c(B, T, \theta)$ data measured in the Cold Head at temperatures between 10 K and 83 K, fields from 0 T up to 0.7 T, and angles of the field to the tape normal between 0° and 180°. We have therefore showed that the miniaturisation of the REBCO CC by the use of small tracks has enabled a characterisation of the critical surface of full-width REBCO CC down to 10 K using a simple cryocooler experimental setup. This experimental miniaturisation can further enable characterisation of REBCO at much higher fields, where the magnet bore size is too small to accommodate measurements on full-width tapes.

Then we presented the results of a small investigation into the J_c dependence on ε for different orientations of the current and ε within the REBCO tape. The results suggest that the J_c was the most sensitive to compressive strain when the current and strain were aligned, and much less sensitive when they were orthogonal. The data also suggested there was a small amount anisotropy in the strain dependence when the current and ε were applied along the length of the tape, where J_c was found to be more sensitive to ε, compared to across its width, where it was less sensitive.

Chapter 8

Conclusion and Future Work

The motivation of the work presented in this doctoral thesis has been to investigate the $J_c(B, T, \theta, \varepsilon)$ surface of narrow tracks of HTS REBCO CC down to 5 µm in width. The superconductor REBCO is a promising candidate to be used in the magnet system of future Tokamaks due to its higher critical parameter values compared to the low temperature superconductors. This enhanced critical surface allows REBCO to carry more current in higher magnetic fields, enabling the production of much strong superconducting magnets in more extreme operating conditions for a much more compact plasma confinement in Tokamaks. Therefore, it is of great interest to study REBCO and investigate its performance in Tokamak-like operating conditions for future clean energy purposes.

To characterise the performance of REBCO CCs in the magnet system of future Tokamaks, which will likely operate at around 20 K and 20 T, full-width REBCO CC tapes can not easily be used for testing due to the high currents required at low temperatures, and the small space available in the narrow bore size of the applied field magnets requiring a more miniaturised experimental setup than is possible with full-width tapes. The importance of

using tracks is therefore as follows: if it were found that the track J_c critical surface superposed the critical surface of a full-width REBCO CC tape, then the characterisation of REBCO tapes would be possible using narrow tracks of the REBCO CC. Due to the much smaller currents carried by tracks producing less ohmic heating, as well as the much smaller experimental setup, this would open up a much larger range of temperatures, fields and strains at which REBCO CC could be characterised, especially at lower temperatures and at higher fields, allowing a characterisation of the performance of REBCO CC in Tokamak-like operating conditions.

To answer the question of whether the narrow tracks of REBCO replicate the performance of full-width REBCO CC tapes, and can hence be used to characterise REBCO CCs for future Tokamaks, this thesis was structured as follows. Firstly, some background information on the importance of nuclear fusion development and the role of REBCO in future Tokamaks was presented in Chapter 2. Then in Chapter 3 we outlined the theory of superconductivity and some explanation for the $J_c(B, T, \theta, \varepsilon)$ critical surface of REBCO CC in terms of its microstructure. In Chapter 4 we presented some preliminary work done to measure $B_{c2}(T, \theta, \varepsilon)$ on full-width REBCO tapes and Chapter 5 outlined the techniques used to prepare the REBCO tracks for the remainder of the work, namely using chemical etching to produce tracks 200 µm wide, and FIB milling to produce tracks 5 µm wide. The results of the $J_c(\varepsilon)$ dependence for tracks is presented in Chapter 6, and the results from two important experiments are presented in Chapter 7, one of which was to determine the $J_c(B, T, \theta)$ dependence of a FIB track using a developed Cold Head cryocooler system, and the second was to determine the strain dependence of J_c for different orientations of the current and strain in the tape enabled by tracks.

The main conclusions from this experimental PhD were as follows. Firstly the chemically etched tracks were found to have the same $J_c(B, \theta, \varepsilon)$ depen-

dence as the full-width REBCO CC tapes, allowing a full characterisation of REBCO tapes using these tracks down to 200 µm wide.

The second conclusion was that, although the FIB tracks produced a J_c dependence on field and angle of the field to the tape normal that was in agreement with the chemically etched tracks, the strain dependence was however not in agreement. It was found that the $J_c(\varepsilon)$ of the FIB tracks had a much more sensitive response of J_c to ε, and the peak in the strain curves was not centred around 0 % strain but instead shifted to much high tensile strains of 0.3 % or more. This shift in the position of $J_{c,peak}$ to tensile strains was characteristic of a REBCO microstructure that was A-domain rich, and fits to the chain model and imaging using EBSD confirmed this, finding the volume fraction of A-domains within the FIB tracks to be around 80 %. In summary, the FIB tracks were not able to characterise the ε dependence of REBCO, and the reason for this was found to be that the FIB milling process was changing the domain structure within the REBCO tracks causing the REBCO to de-twin and be constituted by a higher fraction of A domains. Furthermore, the precise orientation of the detwinning was found to depend on the direction of the FIB milling, whereby the A domains were forced to align along the length of the FIB milled tracks and the B domains along the track width.

One other final conclusion from the strain work was drawn from an experiment done to determine the $J_c(\varepsilon)$ curves for different orientations of current and ε within the REBCO tape enabled by the use of tracks. The results from this experiment proved that when the current and strain were applied in orthogonal directions the J_c response to ε was much weaker compared to when the current and strain were parallel. In addition, it was found that J_c was slightly less sensitive to ε when the current and ε were applied along the tape width compared to when applied along the tape length.

Despite the difference in ε response, the use of FIB tracks still enabled a

full set of $J_c(B, T, \theta)$ data down to 10 K and up to 0.7 T measured using an upgraded Cold Head cryocooler system, proving the success of a full characterisation of REBCO $J_c(B, T, \theta)$ over a large range of fields and temperatures using a simple Cold Head cryocooler setup.

The next step in this work will be to design and implement an in-situ strain device to enable the full $J_c(B, T, \theta, \varepsilon)$ data set on tracks in the cryocooler. The difficulties involved in implementing an in-situ strain upgrade to our setup primarily are maintaining a good thermal contact of the strain board to the conductive sample platform whilst applying strain. Several ideas and preliminary designs involving the use of push-rods, motors and piezoelectric actuators to apply strain have been considered, but these designs have been found to have too many practical difficulties, however a new design incorporating these ideas and integrating a push-rod with a spring system has been recently developed for the Cold Head [174]. Our work has also brought to attention the requirement of a new technique to fabricate very narrow 5 µm tracks of REBCO to replace FIB milling for use in this future setup, where laser etching and photolithography are the most likely alternatives, to enable measurements on tracks in high pulsed field facilities such as those at Los Alamos, which is an area of future work.

Appendix A

Appendix

Data from all figures in this thesis and LabVIEW files used for all measurements are available at https://durhamuniversity-my.sharepoint.com/:f:/r/personal/dph0dh_durham_ac_uk/Documents/(114)%20Emma%20Gillard%20thesis%20archive?csf=1&web=1&e=I7MRCv

Files of the FIB track drawings and settings of used for the FIB milling.

CleWin drawing file of the 5 µm FIB tracks:

https://durhamuniversity-my.sharepoint.com/:u:/r/personal/dph0dh_durham_ac_uk/Documents/(114)%20Emma%20Gillard%20thesis%20archive/FIB%20Code/FIB%20curved%20corners%205um%20track%202um%20wells.gds?csf=1&web=1&e=kG1fNO

GDSTODB ASCII stream file for 5 µm wide FIB tracks with 20 µm deep and 2 µm wide milled wells:

https://durhamuniversity-my.sharepoint.com/:u:/r/personal/dph0dh_durham_ac_uk/Documents/(114)%20Emma%20Gillard%20thesis%20archive/

FIB%20Code/20um%20%5B366%C2%B5m%209.3nA%5D%205um%20tracks.str?csf=1&web=1&e=uEfp79

FIB milling settings for the 5 µm tracks:

https://durhamuniversity-my.sharepoint.com/:t:/r/personal/dph0dh_durham_ac_uk/Documents/(114)%20Emma%20Gillard%20thesis%20archive/FIB%20Code/20um%20%5B366%C2%B5m%209.3nA%5D%205um%20tracks.txt?csf=1&web=1&e=2wG3uE

Files for G10 measurement probe drawings.

Inventor files for the G10 measurement probe:

https://durhamuniversity-my.sharepoint.com/:u:/r/personal/dph0dh_durham_ac_uk/Documents/(114)%20Emma%20Gillard%20thesis%20archive/Probe%20drawings/Liquid%20nitrogen%20measurement%20probe.dwg?csf=1&web=1&e=iFFkTY

https://durhamuniversity-my.sharepoint.com/:u:/r/personal/dph0dh_durham_ac_uk/Documents/(114)%20Emma%20Gillard%20thesis%20archive/Probe%20drawings/Liquid%20nitrogen%20measurement%20probe.ipt?csf=1&web=1&e=MFAGap

Drawings and description of the Cold Head upgrade system (Chapter 7).

The Cold Head as found and used in Chapter 4 was only able to perform variable temperature measurements $J_c(T)$. In order to fit the sample in the Cold Head between the poles of the 1 T electromagnet to enable the $J_c(B, T, \theta)$ measurements in Chapter 7, some upgrades were required.

The experimental development consisted of two parts: the first part involved redesigning the sample platform, radiation shield and vacuum shroud to fit between the poles of the magnet, and the second part involved improving the

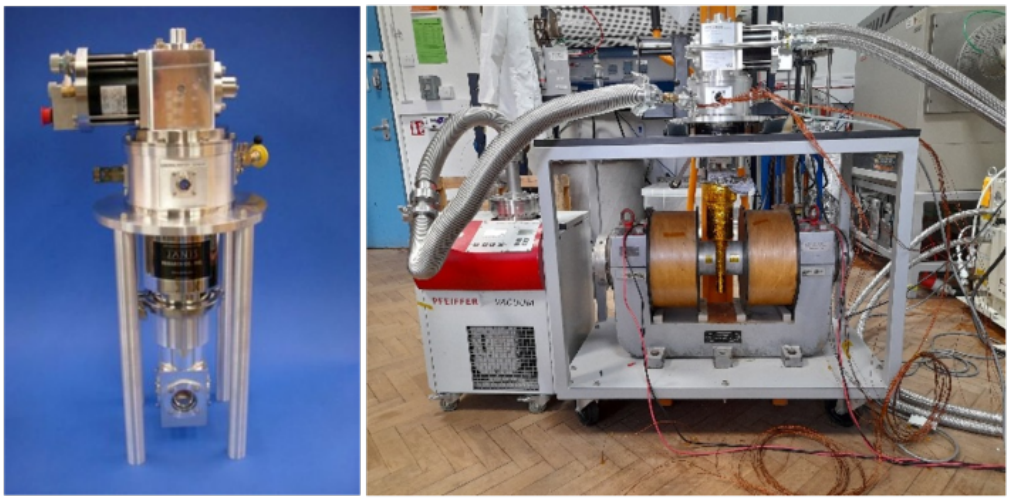

Figure A.1: Original Cold Head as found for $J_c(T)$ measurements (left). New Cold Head and 1 T electromagnet after the upgrades for $J_c(B, T, \theta)$ measurements (right).

temperature control and stability at the sample location.

Images of the Cold Head system before and after the upgrades are shown in Fig. A.1.

Due to the limited space available of around 30 mm, all parts to fit between the magnet poles were designed very precisely to fit in the compact space, and the materials were chosen carefully to serve their required purposes. The sample platform was made out of copper to ensure a good thermal conductive path between stage two of the Cold Head and the sample, and was made to a specific length such that the sample was situated at the centre between the pole pieces when installed on the end of the sample platform. The radiation shield was made out of aluminium which reflected the radiation from the outside environment well, and the vacuum shroud was made out of a 1 mm thick layer of stainless steel which was the thinnest it could be made to still be able to hold a good vacuum and not be in contact with the radiation

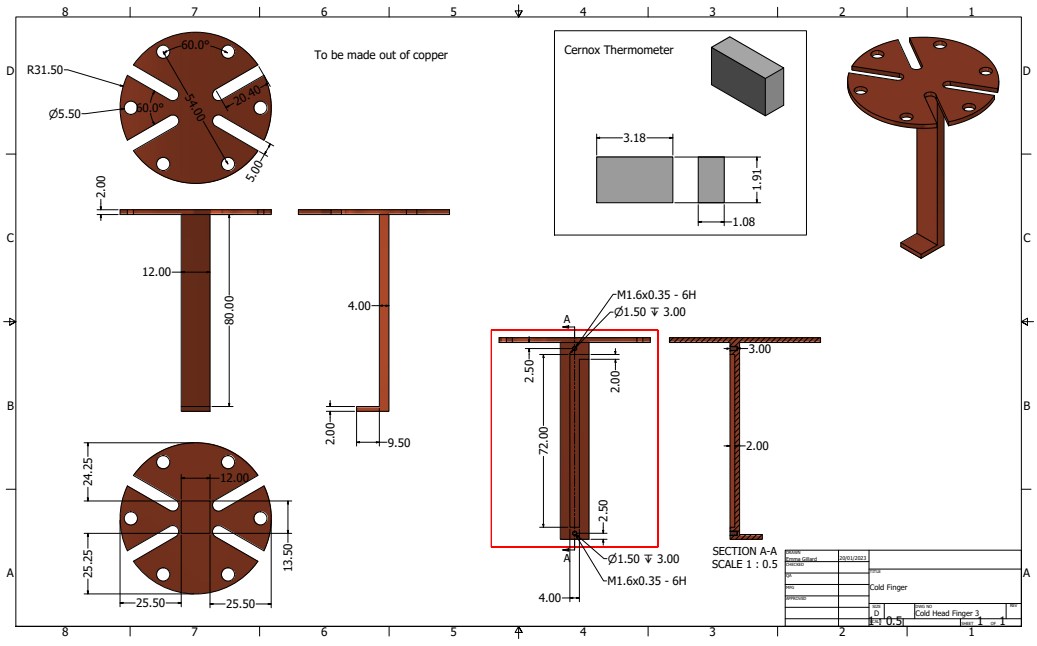

Figure A.2: Inventor drawing of the upgraded sample platform.

shield. Drawings of the new sample platform, radiation shield and vacuum shroud are given in Figs. A.2, A.3 and A.4 respectively.

To vary the angle, a simple protractor was printed and attached to the top of the Cold Head and aligned with a second tabletop protractor, in this way the magnetic field angle could be changed manually by physically rotating the Cold Head.

Now that the system was able to fit inside a magnetic field, we moved onto the next step which was to improve the thermometry.

The Cold Head as found was installed with a silicon diode thermometer and a heater on the second stage and the temperature was controlled through the interplay of the thermometer reading and heater output. However, as the sample on the new sample platform was now far from the silicon diode

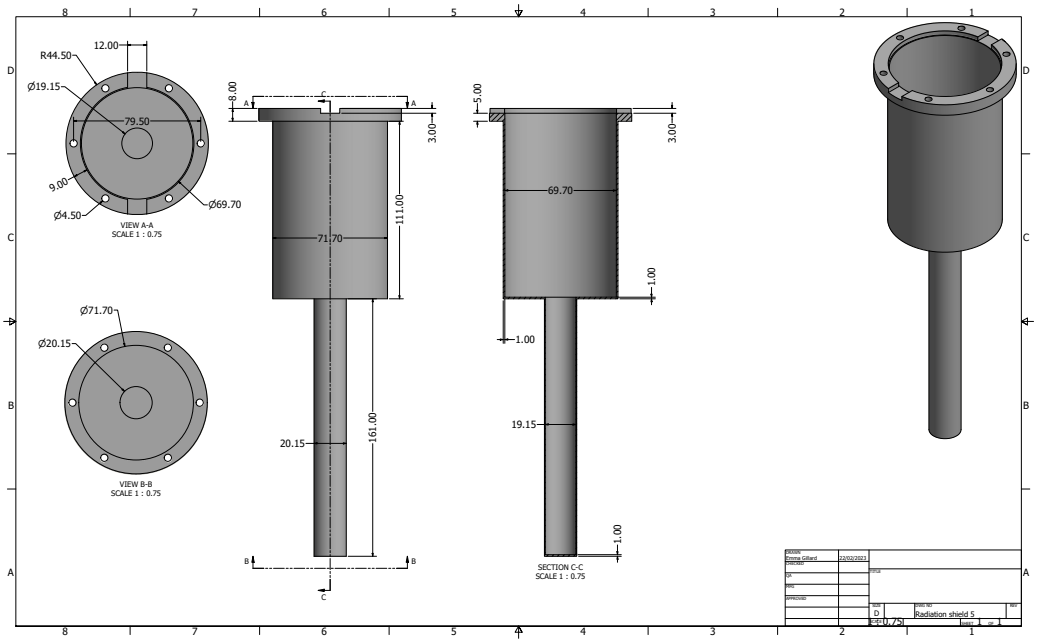

Figure A.3: Inventor drawing of the upgraded radiation shield.

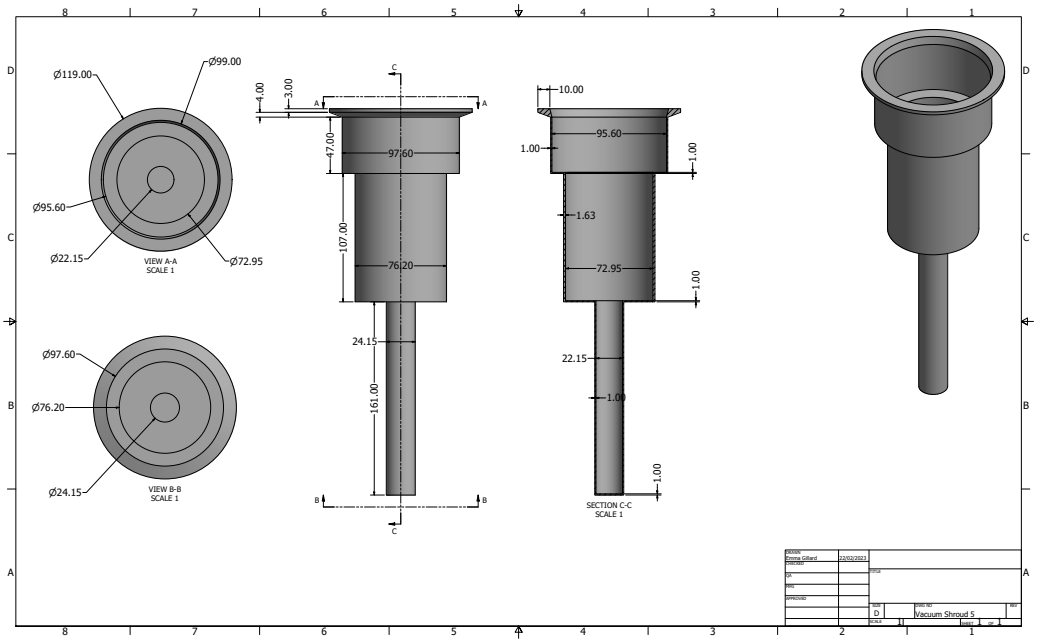

Figure A.4: Inventor drawing of the upgraded vacuum shroud.

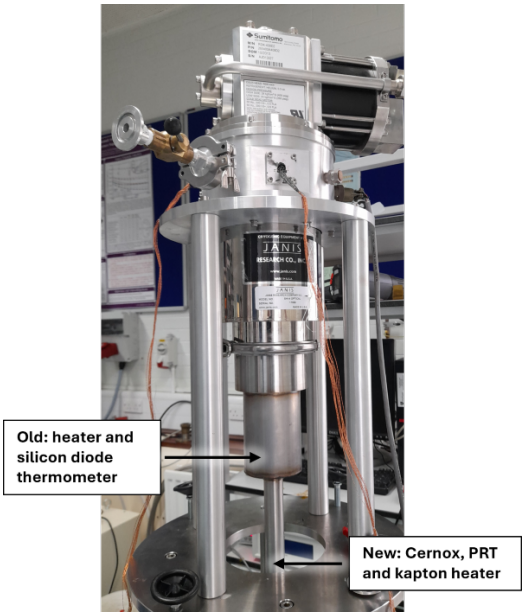

Figure A.5: Positioning of the original and new heaters and thermometers in the upgraded Cold Head.

thermometer, this thermometer was no longer accurately able to measure the precise temperature at the sample location. Therefore, a second Cernox thermometer was installed in a well in the sample platform directly behind the sample to precisely measure the sample temperature.

We then attempted to control the temperature at the sample using the interplay between the new Cernox and the original heater, but due to the large distance between them (see Fig. A.5), this led to very large non-converging temperature oscillations. The PID parameters were adjusted to try to compensate for this, however no values could remove the oscillations and therefore two localised Kapton heaters (rated 10 W, 28 V each) were connected in series and installed next to the Cernox and below the sample.

The Kapton heater combination was wired in parallel with the original so that each heater received a current that produced a roughly equal power

output, and the PID values adjusted slightly to allow a stable control of the temperature of the sample, which were found to be 30, 10, 0. The current sent through the heaters from the temperature controller was set to be 2 A; enough current to provide sufficient heating but not enough to burn through the Kapton heaters. With this new setup, we were able to control the temperature of the sample to within 0.05 K. An illustration of the new thermometry setup is given in Fig. A.5.

Bibliography

[1] S. Meschini, F. Laviano, F. Ledda, *et al.*, "Review of commercial nuclear fusion projects," *Frontiers in Energy Research*, vol. 11, p. 1 157 394, 2023.

[2] G. Katoch, G. Sharma, M. Alaghbari, *et al.*, "Fusion energy: A sustainable pathway to meeting future global energy demands," *Discover Sustainability*, vol. 6, no. 1, p. 221, 2025.

[3] D. Maradin, "Advantages and disadvantages of renewable energy sources utilization," *International Journal of Energy Economics and Policy*, vol. 11, no. 3, pp. 176–183, 2021.

[4] S. Shafiee and E. Topal, "When will fossil fuel reserves be diminished?" *Energy policy*, vol. 37, no. 1, pp. 181–189, 2009.

[5] M. Englert, L. Krall, and R. C. Ewing, "Is nuclear fission a sustainable source of energy?" *MRS bulletin*, vol. 37, no. 4, pp. 417–424, 2012.

[6] National Oceanic and Atmoshperic Administration, *Climate change impacts*, Available at `https://www.noaa.gov/education/resource-collections/climate/climate-change-impacts` (07/04/2025).

[7] Z. Guo, *Nuclear fusion: Overview of challenges and recent progress*, 2023.

[8] J. Wesson and D. J. Campbell, *Tokamaks*. Oxford university press, 2011, vol. 149.

[9] K. Whittle, *Nuclear materials science*. IOP Publishing, 2020.

[10] J. P. Freidberg, *Plasma physics and fusion energy*. Cambridge university press, 2008.

[11] P. Magaud, G. Marbach, and I. Cook, "Nuclear fusion reactors," *Encyclopedia of Energy*, vol. 4, pp. 365–381, 2004.

[12] The ITER Organisation, *What is a tokamak?* Available at `https://www.iter.org/machine/what-tokamak` (10/04/2025).

[13] G. D. Dubus, "From plain visualisation to vibration sensing: Using a camera to control the flexibilities in the ITER remote handling equipment," *Disertasi. Tampere University of Technology. Finlandia*, 2014.

[14] J. Ongena, "Nuclear fusion and its large potential for the future world energy supply," *Nukleonika*, vol. 61, no. 4, pp. 425–432, 2016.

[15] M. L. Walker, P. De Vries, F. Felici, and E. Schuster, "Introduction to tokamak plasma control," in *2020 American Control Conference (ACC)*, IEEE, 2020, pp. 2901–2918.

[16] T. Ihli, T. Basu, L. Giancarli, *et al.*, "Review of blanket designs for advanced fusion reactors," *Fusion Engineering and Design*, vol. 83, no. 7-9, pp. 912–919, 2008.

[17] C. Wong, S. Malang, M. Sawan, *et al.*, "Assessment of first wall and blanket options with the use of liquid breeder," *Fusion science and technology*, vol. 47, no. 3, pp. 502–509, 2005.

[18] J. You, G. Mazzone, E. Visca, *et al.*, "Divertor of the european demo: Engineering and technologies for power exhaust," *Fusion Engineering and Design*, vol. 175, p. 113 010, 2022.

[19] P. Norajitra, S. I. Abdel-Khalik, L. M. Giancarli, *et al.*, "Divertor conceptual designs for a fusion power plant," *Fusion Engineering and Design*, vol. 83, no. 7-9, pp. 893–902, 2008.

[20] International Atomic Energy Agency, *Fusion device information system - fusdis*, Available at `https://nucleus.iaea.org/sites/fusionportal/Pages/FusDIS.aspx` (08/04/2025).

[21] S. Atzeni, "Fusion energy: From basic research to commercialization," *Rendiconti Lincei. Scienze Fisiche e Naturali*, pp. 1–10, 2025.

[22] L. Cavallucci, M. Breschi, J. Li, and C. Hoa, "Operation margin of the ITER central solenoid during the plasma scenario," *Applied Sciences*, vol. 15, no. 7, p. 3526, 2025.

[23] H. Meyer and S. P. Team, "Plasma burn—mind the gap," *Philosophical Transactions A*, vol. 382, no. 2280, p. 20 230 406, 2024.

[24] A. Creely, M. J. Greenwald, S. B. Ballinger, *et al.*, "Overview of the SPARC tokamak," *Journal of Plasma Physics*, vol. 86, no. 5, p. 865 860 502, 2020.

[25] B. Sorbom, J. Ball, T. Palmer, *et al.*, "ARC: A compact, high-field, fusion nuclear science facility and demonstration power plant with demountable magnets," *Fusion Engineering and Design*, vol. 100, pp. 378–405, 2015.

[26] Popular Mechanics, *China's fusion reactor reached an unbreakable limit—and broke right through it*, Available at `https://www.popularmechanics.com/science/energy/a69949952/east-reactor-greenwald-limit/` (20/01/2026).

[27] J. Lion, J.-C. Anglès, L. Bonauer, *et al.*, "Stellaris: A high-field quasi-isodynamic stellarator for a prototypical fusion power plant," *Fusion Engineering and Design*, vol. 214, p. 114 868, 2025.

[28] S. Segantin, R. Testoni, Z. Hartwig, D. Whyte, and M. Zucchetti, "Exploration of a fast pathway to nuclear fusion: Thermal analysis and cooling design considerations for the ARC reactor," *Fusion Science and Technology*, vol. 76, no. 1, pp. 45–52, 2020.

[29] Renaissance Fusion, *Renaissance Fusion*, Available at `https://renfusion.eu/` (20/01/2026).

[30] P. Barabaschi, A. Fossen, A. Loarte, A. Becoulet, L. Coblentz, and I. Contributors, "ITER progresses into new baseline," *Fusion Engineering and Design*, vol. 215, p. 114 990, 2025.

[31] A. Baker, "The spherical tokamak for energy production (STEP) in context: UK public sector approach to fusion energy," *Philosophical Transactions A*, vol. 382, no. 2280, p. 20 230 401, 2024.

[32] P. Rodriguez-Fernandez, A. Creely, M. Greenwald, *et al.*, "Overview of the SPARC physics basis towards the exploration of burning-plasma regimes in high-field, compact tokamaks," *Nuclear Fusion*, vol. 62, no. 4, p. 042 003, 2022.

[33] David Dalton, *Nuclear fusion / virginia site to host 'world's first' grid-scale commercial plant*, Available at `https://www.nucnet.org/news/virginia-site-to-host-world-s-first-grid-scale-commercial-plant-12-3-2024` (10/04/2025).

[34] Proxima Fusion, *Our Roadmap*, Available at `https://www.proximafusion.com/about` (20/01/2026).

[35] O. Motojima, "The ITER project construction status," *Nuclear Fusion*, vol. 55, no. 10, p. 104 023, 2015.

[36] B. Wirth, K. Nordlund, D. Whyte, and D. Xu, "Fusion materials modeling: Challenges and opportunities," *MRS bulletin*, vol. 36, pp. 216–222, 2011.

[37] J. Sánchez, "Nuclear fusion as a massive, clean, and inexhaustible energy source for the second half of the century: Brief history, status, and perspective," *Energy Science & Engineering*, vol. 2, no. 4, pp. 165–176, 2014.

[38] R. Kembleton, "Nuclear fusion: What of the future?" In *Managing Global Warming*, Elsevier, 2019, pp. 199–220.

[39] A. M. Bradshaw, T. Hamacher, and U. Fischer, "Is nuclear fusion a sustainable energy form?" *Fusion Engineering and Design*, vol. 86, no. 9-11, pp. 2770–2773, 2011.

[40] D. Perrault, "Nuclear safety aspects on the road towards fusion energy," *Fusion Engineering and Design*, vol. 146, pp. 130–134, 2019.

[41] J. Li, J. Zhang, and X. Duan, "Magnetic fusion development for global warming suppression," *Nuclear fusion*, vol. 50, no. 1, p. 014 005, 2009.

[42] B. Lindley, T. Roulstone, G. Locatelli, and M. Rooney, "Can fusion energy be cost-competitive and commercially viable? an analysis of magnetically confined reactors," *Energy policy*, vol. 177, p. 113 511, 2023.

[43] R. Toschi, "Nuclear fusion, an energy source," *Fusion engineering and design*, vol. 36, no. 1, pp. 1–8, 1997.

[44] P. Komarek, "Potential and desire for HTS application in thermonuclear fusion," *Fusion engineering and design*, vol. 81, no. 20-22, pp. 2287–2296, 2006.

[45] P. Bruzzone, W. H. Fietz, J. V. Minervini, *et al.*, "High temperature superconductors for fusion magnets," *Nuclear Fusion*, vol. 58, no. 10, p. 103 001, 2018.

[46] D. Whyte, "Small, modular and economically attractive fusion enabled by high temperature superconductors," *Philosophical Transactions of the Royal Society A*, vol. 377, no. 2141, p. 20 180 354, 2019.

[47] Y. Zhai, D. van der Laan, P. Connolly, and C. Kessel, "Conceptual design of HTS magnets for fusion nuclear science facility," *Fusion Engineering and Design*, vol. 168, p. 112 611, 2021.

[48] D. J. Miller, V. A. Maroni, J. M. Hiller, *et al.*, "Characterization of long-length, MOCVD-derived REBCO coated conductors," *IEEE transactions on applied superconductivity*, vol. 19, no. 3, pp. 3176–3179, 2009.

[49] D. Van Delft and P. Kes, "The discovery of superconductivity," *Europhysics News*, vol. 42, no. 1, pp. 21–25, 2011.

[50] V. Kozhevnikov, "Meissner effect: History of development and novel aspects," *Journal of Superconductivity and Novel Magnetism*, vol. 34, no. 8, pp. 1979–2009, 2021.

[51] M. Raine, "High field superconductors for fusion energy applications," Ph.D. dissertation, Durham University, 2015.

[52] D. K. Namburi, Y. Shi, and D. A. Cardwell, "The processing and properties of bulk (RE)BCO high temperature superconductors: Current status and future perspectives," *Superconductor Science and Technology*, vol. 34, no. 5, p. 053 002, 2021.

[53] C. P. Poole, H. A. Farach, R. J. Creswick, and R. Prozorov, *Superconductivity*. Elsevier, 2014.

[54] J. G. Bednorz and K. A. Müller, "Possible high T_c superconductivity in the Ba-La-Cu-O system," *Zeitschrift für Physik B Condensed Matter*, vol. 64, no. 2, pp. 189–193, 1986.

[55] T. Sheahen, *Introduction to high-temperature superconductivity*. Springer Science & Business Media, 1994.

[56] M. A. Rahman, M. Z. Rahaman, and M. N. Samsuddoha, "A review on cuprate based superconducting materials including characteristics and applications," *American Journal of Physics and Applications*, vol. 3, no. 2, pp. 39–56, 2015.

[57] B. Gamble, G. Snitchier, and R. Schwall, "Prospects for HTS applications," *IEEE Transactions on Magnetics*, vol. 32, no. 4, pp. 2714–2719, 2002.

[58] T. A. Coombs, Q. Wang, A. Shah, *et al.*, "High-temperature superconductors and their large-scale applications," *Nature Reviews Electrical Engineering*, vol. 1, no. 12, pp. 788–801, 2024.

[59] X. Li, M. D. Ainslie, D. Song, W. Yang, and R. Macian-Juan, "REBCO coated conductors: Enabling the next generation of tokamak reactors," *Superconductor Science and Technology*, 2024.

[60] K. Wang, H. Dong, D. Huang, *et al.*, "Advances in second-generation high-temperature superconducting tapes and their applications in high-field magnets," *Soft Science*, vol. 2, no. 3, N–A, 2022.

[61] M. Noe, W. Goldacker, R. Heller, T. Schneider, and W. Fietz, "HTS applications," 2009.

[62] A. K. Jha and K. Matsumoto, "Superconductive REBCO thin films and their nanocomposites: The role of rare-earth oxides in promoting sustainable energy," *Frontiers in Physics*, vol. 7, p. 82, 2019.

[63] A. Bussmann-Holder and H. Keller, "High-temperature superconductors: Underlying physics and applications," *Zeitschrift für Naturforschung B*, vol. 75, no. 1-2, pp. 3–14, 2020.

[64] A. Koblischka-Veneva and M. R. Koblischka, "$Ba_2Cu_3O_{7-\delta}$ and the roeser-huber formula," *Materials*, vol. 14, no. 20, p. 6068, 2021.

[65] J. C. Lewis, K. Adams, W. Iliffe, *et al.*, "Local structure analysis of ${}_{00}$kev he^+ irradiated REBCO coated conductor using polarisation dependent Cu K edge EXAFS," *Superconductor Science and Technology*, vol. 38, no. 1, p. 015 022, 2024.

[66] J. L. MacManus-Driscoll and S. C. Wimbush, "Processing and application of high-temperature superconducting coated conductors," *Nature Reviews Materials*, vol. 6, no. 7, pp. 587–604, 2021.

[67] S. Foltyn, L. Civale, J. MacManus-Driscoll, *et al.*, "Materials science challenges for high-temperature superconducting wire," *Nature materials*, vol. 6, no. 9, pp. 631–642, 2007.

[68] Amalia Ballerino, *Technical superconductors: HTS*, Available at `https://indico.cern.ch/event/1227234/contributions/5601049/attachments/2758083/4802548/Lecture_Ballarino.pdf` (04/06/2025).

[69] A. Goyal and S.-H. Wee, "Buffer layers for REBCO films for use in superconducting devices," Oak Ridge National Laboratory (ORNL), Oak Ridge, TN (United States), Tech. Rep., 2014.

[70] M. Dedicatoria, H. Shin, H. Ha, S. Oh, and S. Moon, "Electro-mechanical property evaluation of REBCO coated conductor tape with stainless steel substrate," *Progress in Superconductivity and Cryogenics*, vol. 12, no. 4, pp. 20–23, 2010.

[71] Y. Iijima, N. Tanabe, Y. Ikeno, and O. Kohno, "Biaxially aligned $YBa_2Cu_3O_{7-x}$ thin film tapes," *Physica C: Superconductivity*, vol. 185, pp. 1959–1960, 1991.

[72] Y. Liu, H. Suo, Z. Zhang, *et al.*, "The possible dominant factors in the mechanical properties of the metallic substrates of various commercial REBCO tapes," *Physica C: Superconductivity and its Applications*, vol. 629, p. 1 354 643, 2025.

[73] X. Wang, A. B. Yahia, E. Bosque, *et al.*, "REBCO–a silver bullet for our next high-field magnet and collider budget?" *arXiv preprint arXiv:2203.08736*, 2022.

[74] V. Matias, B. J. Gibbons, A. T. Findikoglu, P. C. Dowden, J. Sullard, and J. Y. Coulter, "Continuous fabrication of IBAD-MgO based coated conductors," *IEEE transactions on applied superconductivity*, vol. 15, no. 2, pp. 2735–2738, 2005.

[75] G. Hubler, "Fundamentals of ion-beam-assisted deposition: Technique and film properties," *Materials Science and Engineering: A*, vol. 115, pp. 181–192, 1989.

[76] U. Balachandran, B. Ma, M. Li, *et al.*, "Development of coated conductors by inclined substrate deposition," *Physica C: Superconductivity*, vol. 392, pp. 806–814, 2003.

[77] M. Paidpilli and V. Selvamanickam, "Development of RE-Ba-Cu-O superconductors in the US for ultra-high field magnets," *Superconductor Science and Technology*, vol. 35, no. 4, p. 043 001, 2022.

[78] M. R. Khan, A. Leo, A. Masi, *et al.*, "Comparison of commercial REBCO tapes through flux pinning energy," *Crystals*, vol. 14, no. 12, p. 1017, 2024.

[79] Y. Xu and D. Shi, "A review of coated conductor development," *Tsinghua science and technology*, vol. 8, no. 3, pp. 342–369, 2003.

[80] SuperPower Inc, *Our technology*, Available at `https://www.superpower-inc.com/Technology.aspx` (04/07/2025).

[81] SuperPower Inc, *2G HTS wire specification*, Available at `https://www.superpower-inc.com/specification.aspx` (14/07/2025).

[82] Vladimir Matias, *State of coated conductor industry REBCO roundtable*, Available at `https://indico.fnal.gov/event/61772/attachments/172362/233118/matias20vladimir.pdf` (05/06/2025).

[83] G. Majkic, R. Pratap, A. Xu, E. Galstyan, and V. Selvamanickam, "Over 15 MA/cm^2 of critical current density in 4.8 μm thick, zr-doped (Gd,Y)$Ba_2Cu_3O_x$ superconductor at 30K, 3T," *Scientific reports*, vol. 8, no. 1, p. 6982, 2018.

[84] A. Xu, Y. Zhang, M. H. Gharahcheshmeh, *et al.*, "J_c(4.2K, 31.2T) beyond 1 kA/mm^2 of a 3.2 μm thick, 20 mol% Zr-added MOCVD REBCO coated conductor," *Scientific Reports*, vol. 7, no. 1, p. 6853, 2017.

[85] C. Yao and Y. Ma, "Superconducting materials: Challenges and opportunities for large-scale applications," *Iscience*, vol. 24, no. 6, 2021.

[86] Yifei Zhang, *Advances and perspectives in REBCO coated conductor production at SuperPower*, Available at `https://indico.cern.ch/event/1347361/contributions/6308479/attachments/3029135/5346980/2025$\%$20CCA$\%$20presentation_SuperPower_yz.pdf` (05/06/2025).

[87] Y. Zhao, Y. Wu, A. Goyal, H. Huhtinen, P. Paturi, and Y. Tsuchiya, "Commercial compact fusion triggered REBCO tape industry: Pulsed laser deposition technology opportunities and challenges," *Superconductivity*, p. 100 188, 2025.

[88] C. Senatore, M. Bonura, and T. Bagni, "REBCO tapes for applications in ultra-high fields: Critical current surface and scaling relations," *Superconductor Science and Technology*, vol. 37, no. 11, p. 115 013, 2024.

[89] SuperPower-inc, *Superpower® 2g hts wire type - scs4050-ap, 20um cu qs m4-534-14 0104 (1740-1800m)*, Type: SCS4050-AP, Spool ID:

20230112, Internal ID: M4-534-14 0104, Length: 60 m, Width: 4.01 mm, Thickness: 0.075 mm, Av. Ic: 131 A, Min Ic: 126 A, 2020.

[90] C. Wang, K. Do, M. Beasley, T. Geballe, and R. Hammond, "Deposition of in-plane textured MgO on amorphous Si_3N_4 substrates by ion-beam-assisted deposition and comparisons with ion-beam-assisted deposited yttria-stabilized-zirconia," *Applied Physics Letters*, vol. 71, no. 20, pp. 2955–2957, 1997.

[91] M. Paidpilli, R. Pratap, M. Kochat, *et al.*, "Growth of high-performance 4-5μm thick film REBCO tapes doped with hafnium using advanced MOCVD," *IEEE Transactions on Applied Superconductivity*, vol. 31, no. 5, pp. 1–5, 2021.

[92] D. Agassi, D. Christen, and S. Pennycook, "Flux pinning and critical currents at low-angle grain boundaries in high-temperature superconductors," *Applied physics letters*, vol. 81, no. 15, pp. 2803–2805, 2002.

[93] S. O. Mbam and X.-F. Gou, "Inspection of fabrication defects in REBCO coated conductors from various industrial manufacturers under similar fabrication conditions using the DEM approach," *Physica C: Superconductivity and its applications*, vol. 574, p. 1 353 664, 2020.

[94] D. Abraimov, J. Kvitkovic, and O. Yavuz, *Origins of low-temperature in-field J_c variability in modern MOCVD REBCO tapes*, Available at `https://nationalmaglab.org/library/presentations/NHMFL_Presentation-10885.pdf` (09/06/2025).

[95] M. de Leon, M. A. Diaz, and H.-S. Shin, "Interaction of cracks and precipitate particles on the REBCO superconducting layers of practical CC tapes through fractographic observations," *Progress in Superconductivity and Cryogenics*, vol. 22, no. 3, pp. 7–12, 2020.

[96] G. Li, X. Fang, L. Zhao, *et al.*, "Precisely determined temperature window size for the growth of high quality c-axis oriented YBCO films by photo-assisted MOCVD," *Physica C: Superconductivity*, vol. 468, no. 21, pp. 2213–2218, 2008.

[97] M. Yoshizumi, T. Izumi, and Y. Shiohara, "Development of coated conductors in japanese national project "development of fundamental technologies for HTS coils"," *Physics Procedia*, vol. 65, pp. 117–120, 2015.

[98] P. Li, D. Abraimov, A. Xu, and D. Larbalestier, "Observation of important current-limiting defects in a recent high pinning force MOCVD IBAD-MgO coated conductor," *Superconductor Science and Technology*, vol. 25, no. 2, p. 025 002, 2011.

[99] S. H. Wee, Y. L. Zuev, C. Cantoni, and A. Goyal, "Engineering nanocolumnar defect configurations for optimized vortex pinning in high temperature superconducting nanocomposite wires," *Scientific reports*, vol. 3, no. 1, p. 2310, 2013.

[100] D. Abraimov, J. Jaroszynski, and A. Francis, *Beyond 20T: Tape characterization*, Available at `https://indico.cern.ch/event/588810/contributions/2473703/attachments/1414294/2164567/7__2017_Barcelona_WAMHTS_4_Abraimov_cut4.pdf` (06/06/2025).

[101] M. T. Paulose, J. S. Sandra, M. A. Sayeed, and V. Selvamanickam, "Development of REBCO thin films using MOCVD on non-standard buffers and substrates," *IEEE Transactions on Applied Superconductivity*, 2024.

[102] V. Rouco, A. Palau, R. Guzman, *et al.*, "Role of twin boundaries on vortex pinning of CSD YBCO nanocomposites," *Superconductor Science and Technology*, vol. 27, no. 12, p. 125 009, 2014.

[103] P. Branch, K. Osamura, and D. Hampshire, "Weak emergence in the angular dependence of the critical current density of the high temperature superconductor coated conductor REBCO," *Supercond. Sci. Technol.*, vol. 33, no. 10, p. 104 006, 2020.

[104] K. Osamura, S. Machiya, K. Kajiwara, *et al.*, "Inverted-parabolic and weak strain dependencies on the critical current in practical $< 110 >$

and $< 100 >$ oriented REBCO tapes," *AIP Advances*, vol. 9, no. 7, 2019.

[105] K. Osamura, S. Machiya, Y. Tsuchiya, *et al.*, "Microtwin structure and its influence on the mechanical properties of REBCO coated conductors," *IEEE transactions on applied superconductivity*, vol. 22, no. 1, pp. 8 400 809–8 400 809, 2012.

[106] C. Senatore, C. Barth, M. Bonura, M. Kulich, and G. Mondonico, "Field and temperature scaling of the critical current density in commercial REBCO coated conductors," *Superconductor Science and Technology*, vol. 29, no. 1, p. 014 002, 2015.

[107] G. Succi, A. Ballarino, S. Hopkins, C. Barth, and Y. Yang, "Magnetic field and temperature scaling of the critical current of REBCO tapes," *IEEE Transactions on Applied Superconductivity*, vol. 34, no. 3, pp. 1–7, 2024.

[108] M. Miura, B. Maiorov, S. Baily, *et al.*, "Mixed pinning landscape in nanoparticle-introduced $YGdBa_2Cu_3O_y$ films grown by metal organic deposition," *Physical Review B—Condensed Matter and Materials Physics*, vol. 83, no. 18, p. 184 519, 2011.

[109] P. Paturi, "The vortex path model and angular dependence of J_c in thin YBCO films deposited from undoped and $BaZrO_3$-doped targets," *Superconductor Science and Technology*, vol. 23, no. 2, p. 025 030, 2010.

[110] W. Pi, A. Shu, Y. Shen, *et al.*, "Magnetic field angle dependence of critical current in REBCO tapes produced by different techniques," *IEEE Transactions on Applied Superconductivity*, vol. 34, no. 3, pp. 1–6, 2024.

[111] N. A. Mineev and I. A. Rudnev, "Angular distributions of the critical current of REBCO coated conductors in magnetic field up to 5T," *Progress in Superconductivity and Cryogenics*, vol. 17, no. 1, pp. 6–9, 2015.

[112] J. Lu, Y. Xin, Y. Zhang, and H. Bai, "ab-plane tilt angles in REBCO conductors," *IEEE Transactions on Applied Superconductivity*, vol. 33, no. 5, pp. 1–4, 2023.

[113] M. Weigand, N. A. Rutter, S.-L. Sahonta, and J. H. Durrell, "Critical current densities of MOCVD tapes for different current directions," *IEEE transactions on applied superconductivity*, vol. 21, no. 3, pp. 3347–3351, 2010.

[114] T. Suzuki, S. Awaji, H. Oguro, and K. Watanabe, "Applied strain effect on superconducting properties for detwinned (Y,Gd)BCO coated conductors," *IEEE Transactions on Applied Superconductivity*, vol. 25, no. 3, pp. 1–4, 2014.

[115] S. Awaji, T. Suzuki, H. Oguro, K. Watanabe, and K. Matsumoto, "Strain-controlled critical temperature in $REBa_2Cu_3O_y$-coated conductors," *Scientific Reports*, vol. 5, no. 1, p. 11 156, 2015.

[116] K. Osamura, S. Machiya, and D. P. Hampshire, "Mechanism for the uniaxial strain dependence of the critical current in practical REBCO tapes," *Superconductor Science and Technology*, vol. 29, no. 6, p. 065 019, 2016.

[117] P. Branch, Y. Tsui, K. Osamura, and D. P. Hampshire, "Weakly-emergent strain-dependent properties of high field superconductors," *Sci. Rep.*, vol. 9, p. 13 998, 2019.

[118] D. C. van der Laan, D. Abraimov, A. Polyanskii, *et al.*, "Anisotropic in-plane reversible strain effect in $Y_{0.5}Gd_{0.5}Ba_2Cu_3O_{7-\delta}$ coated conductors," *Superconductor Science and Technology*, vol. 24, no. 11, p. 115 010, 2011.

[119] J. Greenwood, To be published, 2025.

[120] C. W. Gurnham and D. P. Hampshire, "Self-field effects in a josephson junction model for J_c in rebco tapes," *IEEE Transactions on Applied Superconductivity*, vol. 32, no. 4, pp. 1–5, 2021.

[121] Quantum Design, *4k ccr sample in vacuum cryostats shi-4 series*, Available at https://qd-uki.co.uk/cryogenics/janis-4k-cryocoolers/ (03/03/2025).

[122] Quantum Design, *Physical measurement property system*, Available at https://qd-europe.com/fileadmin/Mediapool/products/magnetometers/pdf/PPMS.pdf (03/03/2025).

[123] Ross McDonald, *National high magnetic field laboratory's pulsed field facility at Los Alamos*, Available at https://nationalmaglab.org/user-facilities/pulsed-field (03/03/2025).

[124] Janis Research Company, *Closed cycle refrigerator system manual*, Available at http://appliedcryogenics.com/CRYO\%20DOC/Janis\%20Closed\%20Cycle\%20Refrigerator\%20System\%20Manual.pdf (03/03/2025).

[125] J. Ekin, *Experimental techniques for low-temperature measurements: cryostat design, material properties and superconductor critical-current testing*. Oxford university press, 2006.

[126] Lake Shore Cryotronics, *User's manual model 340 temperature controller*, Available at https://www.lakeshore.com/docs/default-source/product-downloads/340_manual.pdf?sfvrsn=a7420fdf_1&srsltid=AfmBOortjBk8JoVw359BgPDyHkpY6KHCxlGafjKr1odTpeBHwd8IkXTG (03/03/2025).

[127] A. Godeke, M. Dhallé, A. Morelli, L. Stobbelaar, H. van Weeren, and H. J. N. van Eck., "A device to investigate the axial strain dependence of the critical current density in superconductors," *Review of Scientific Instruments*, vol. 75, pp. 5112–5118, 2004.

[128] N. Cheggour and D. P. Hampshire, "A probe for investigating the effects of temperature, strain, and magnetic field on transport critical currents in superconducting wires and tapes," *Review of Scientific Instruments*, vol. 71, no. 12, pp. 4521–4530, 2000.

[129] HBK Shop, *1-ly11-0.3/120 linear strain gauges*, Available at https://b2bstore.hbm.com/myHBM/app/displayApp/(cpgnum=1&layout=7.01-16_153_6_9_70_34_65_73_134_6&uiarea=6&citem=EE4F064EFF141D4EE1000000AC1099345872594 8094F4303E1000000AC10A03A&carea=EE4F064EFF141D4EE1000000AC109934&xcm=hbm_b2boccasionalcrm&rdb=0&cpgsize=0)/.do?rf=y (22/05/2025).

[130] R. He, Y. Tan, Z. Huang, *et al.*, "Bending and uniaxial tensile strain effects on the critical current of REBCO coated conductor tapes," *Cryogenics*, vol. 116, p. 103 285, 2021.

[131] J. R. C. Dizon, A. R. N. Nisay, M. J. A. Dedicatoria, R. C. Munoz, H.-S. Shin, and S.-S. Oh, "Analysis of thermal residual stress/strain in REBCO coated conductor tapes," *IEEE Transactions on Applied Superconductivity*, vol. 24, no. 3, pp. 1–5, 2013.

[132] F. Pierro, M. Delgado, L. Chiesa, X. Wang, and S. O. Prestemon, "Measurements of the strain dependence of critical current of commercial REBCO tapes at 15T between 4.2 and 40K for high field magnets," *IEEE Transactions on Applied Superconductivity*, vol. 29, no. 5, pp. 1–5, 2019.

[133] M. J. Raine, S. A. Keys, and D. P. Hampshire, *Handbook of Superconductivity - Chapter: Characterisation of the Transport Critical Current Density for Conductor Applications*. Taylor and Francis - CRC Press, 2017, p. 32.

[134] Quantum Design, *Physical property measurement system horizontal rotator option user's manual*, Available at https://wmich.edu/sites/default/files/attachments/u1045/2019/15_1384-100\%20Rev.\%20C0\%20PPMS\%20HORIZONTAL\%20ROTATOR\%20USER\%27S\%20MANUAL.pdf (03/03/2025).

[135] F. R. Gamble, F. J. DiSalvo, R. A. Klemm, and T. H. Geballe, "Superconductivity in layered structure organometallic crystals," *Science*, vol. 168, pp. 568–570, 1970.

[136] F. R. Gamble, J. H. Osiecki, M. Cais, R. Pisharody, F. J. DiSalvo, and T. H. Geballe, "Intercalation complexes of lewis bases and layered sulfides: A large class of new superconductors," *Science*, vol. 174, pp. 493–497, 1971.

[137] S. T. Ruggiero, T. W. J. Barbee, and M. R. Beasley, "Superconductivity in quasi-two-dimensional layered composites," *Phys. Rev. Lett.*, vol. 45, pp. 1299–1302, 1980.

[138] W. R. White, A. Kapitulnik, and M. R. Beasley, "Model system for vortex motion in coupled two-dimensional type-II superconductors," *Phys. Rev. Lett.*, vol. 66, pp. 2826–2829, 1991.

[139] A. P. Smith, M. J. Raine, E. Surrey, S. Awaji, T. Okada, and D. P. Hampshire, "3D properties in (RE)BCO tapes measured in fields up to 35T," *IEEE Transactions on Applied Superconductivity*, vol. 29, p. 6 601 005, 2019.

[140] R. A. Klemm, A. Luther, and M. R. Beasley, "Theory of the upper critical field in layered superconductors," *Phys. Rev. B*, vol. 12, no. 3, pp. 877–91, 1975.

[141] P. Benzi, E. Bottizzo, and N. Rizzi, "Oxygen determination from cell dimensions in YBCO superconductors," *J. Crystal Growth*, vol. 269, pp. 625–629, 2004.

[142] T. Okada, H. Misaizu, and S. Awaji, "In-plane domain control of REBCO coated conductors by annealing under bending strain," *IEEE Transactions on Applied Superconductivity*, vol. 31, no. 5, pp. 1–6, 2021.

[143] J. Greenwood *et al.*, "Percolative current flow through anisotropic high-field superconductors under strain," Ph.D. dissertation, Durham University, 2023.

[144] E. Gillard, M. Raine, and D. Hampshire, "Resistivity measurements of the strain, temperature and angular dependence of the upper crit-

ical field of REBCO tapes up to 8T," *IEEE Transactions on Applied Superconductivity*, vol. 33, no. 5, pp. 1–5, 2023.

[145] M. Turenne, R. Johnson, S. Kahn, F. Hunte, L. Ye, and J. Schwartz, "Characterization of REBCO coated conductors for high field magnets," in *Proc. 1st Int. Part. Accel. Conf.*, 2010, pp. 400–402.

[146] J. J. V. Barber, "Investigation of cryogenic cooling for a high-field toroidal field magnet used in the SPARC fusion reactor design," Ph.D. dissertation, Massachusetts Institute of Technology, 2018.

[147] Global Times, *China's all-superconducting magnet hits world-record steady field, boosts aerospace electromagnetic propulsion*, Available at `https://www.globaltimes.cn/page/202509/1344679.shtml` (12/10/2025).

[148] Awaji and Tatsunori, private communication, 2022.

[149] Sigma-Aldrich Solutions, *Ammonia solution 25%*, Available at `https://www.sigmaaldrich.com` (17/07/2025).

[150] Rapid Electronics Limited, *Hydrogen peroxide 30%*, Available at `https://www.rapidonline.com/hydrogen-peroxide-100-volume-h2o2-500ml-52-7476` (17/07/2025).

[151] Sigma-Aldrich Solutions, *Phosphoric acid 10%*, Available at `https://www.sigmaaldrich.com/GB/en/product/mm/480951` (17/07/2025).

[152] K. Tsuchiya, A. Kikuchi, A. Terashima, *et al.*, "Critical current measurement of commercial REBCO conductors at 4.2 k," *Cryogenics*, vol. 85, pp. 1–7, 2017.

[153] FEI Company, *Helios nanolab 400 / 400 s / 400 ml / 600 user operation manual*, Available at `https://nrf.aux.eng.ufl.edu/_files/documents/820.pdf` (18/07/2025).

[154] WieWeb software 2025, *CleWin software*, Available at `https://wieweb.com/site/product-category/clewin-software/` (18/07/2025).

[155] FEI Company, *Gdstodb for dualbeams*, Available at `https://www.yumpu.com/en/document/read/2741480/gdstodb-for-dualbeams` (18/07/2025).

[156] D. Scobbie, Private communication, 2025.

[157] X.-t. Zhang, H.-j. Liu, Y. Shi, F. Liu, and L. Lei, "Critical current degradation behavior of SSTC YBCO tapes under uniaxial strain," in *2018 IEEE International Conference on Applied Superconductivity and Electromagnetic Devices (ASEMD)*, IEEE, 2018, pp. 1–2.

[158] H. Zhang, P. Gao, and X. Wang, "A combination of failures of interfacial delamination and layer cracking in REBCO multilayered conductors," *Engineering Fracture Mechanics*, vol. 274, p. 108 785, 2022.

[159] G. Xiao, C. Zhou, J. Qin, H. Jin, H. Liu, and C. Zhao, "Critical current degradation behaviour of various REBCO tapes under uniaxial strain," *Fusion Engineering and Design*, vol. 190, p. 113 523, 2023.

[160] J. Lu, Y. Xin, B. Jarvis, and H. Bai, "Oxygen out-diffusion in REBCO coated conductor due to heating," *Superconductor Science and Technology*, vol. 34, no. 7, p. 075 004, 2021.

[161] C. Gurnham, V. Große, and D. Hampshire, "Angular J_c measurements at 77 k in-field, on an ISD REBCO coated conductor using a straightforward mechanical scribing technique to reduce tape width," in *Journal of Physics: Conference Series*, IOP Publishing, vol. 1559, 2020, p. 012 036.

[162] Z. Yang, P. Song, M. Guan, F. Feng, and T. Qu, "Critical current degradation and delamination crack observation of epoxy-coated rebco superconducting tapes after thermal cycles in liquid nitrogen," *Ceramics International*, vol. 47, no. 21, pp. 29 824–29 831, 2021.

[163] R. Barns and R. Laudise, "Stability of superconducting $YBa_2Cu_3O_7$ in the presence of water," *Applied physics letters*, vol. 51, no. 17, pp. 1373–1375, 1987.

[164] A. Xu, V. Braccini, J. Jaroszynski, Y. Xin, and D. Larbalestier, "Role of weak uncorrelated pinning introduced by $BaZrO_3$ nanorods at low-temperature in (Y,Gd)$Ba_2Cu_3O_x$ thin films," *Physical Review B—Condensed Matter and Materials Physics*, vol. 86, no. 11, p. 115 416, 2012.

[165] D. C. van der Laan, T. Haugan, P. Barnes, *et al.*, "The effect of strain on grains and grain boundaries in $YBa_2Cu_3O_{7-\delta}$ coated conductors," *Superconductor Science and Technology*, vol. 23, no. 1, p. 014 004, 2009.

[166] K. Sakurai, A. Yamashita, Y. Mizuguchi, K. Yabuuchi, and N. Oono-Hori, "Irradiation effects on copper oxide superconductors including high-entropy REBCO (HE-REBCO)," *Nuclear Materials and Energy*, vol. 40, p. 101 709, 2024.

[167] W. Iliffe, K. Adams, N. Peng, *et al.*, "The effect of in situ irradiation on the superconducting performance of $REBa_2Cu_3O_{7-\delta}$-coated conductors," *MRS bulletin*, vol. 48, no. 7, pp. 710–719, 2023.

[168] D. Taylor, S. Keys, and D. Hampshire, "E-J characteristics and n-values of a niobium–tin superconducting wire as a function of magnetic field, temperature and strain," *Physica C: Superconductivity*, vol. 372, pp. 1291–1294, 2002.

[169] Semiconductor Spectroscopy Devices Group, *Electron backscatter diffraction (EBSD)*, Available at `https://gan-sem.phys.strath.ac.uk/techniques/electron-backscatter-diffraction-ebsd/` (29/09/2025).

[170] A. Koblischka-Veneva, M. R. Koblischka, J. Schmauch, Y. Wan, J. Qian, and X. Yao, "EBSD characterization of specific microstructures in RE-BCO superconductors," *IEEE Transactions on Applied Superconductivity*, vol. 29, no. 3, pp. 1–4, 2018.

[171] M. Koblischka and A. Koblischka-Veneva, "Applications of the electron backscatter diffraction technique to ceramic materials," *Phase Transitions*, vol. 86, no. 7, pp. 651–660, 2013.

[172] M. Weigand, S. Speller, G. Hughes, *et al.*, "Individual grain boundary properties and overall performance of metal-organic deposition coated conductors," *Physical Review B—Condensed Matter and Materials Physics*, vol. 81, no. 17, p. 174 537, 2010.

[173] E. J. Seo, L. Cho, J. K. Kim, *et al.*, "Focused ion beam-induced displacive phase transformation from austenite to martensite during fabrication of quenched and partitioned steel micro-pillar," *Journal of alloys and compounds*, vol. 812, p. 152 061, 2020.

[174] M. Raine, Private communication, 2025.